Institute of Geophysics
Polish Academy of Sciences

PUBLICATIONS
OF THE INSTITUTE OF GEOPHYSICS
POLISH ACADEMY OF SCIENCES

Geophysical Data Bases, Processing and Instrumentation

432 (B-43)

MONOGRAPHIC VOLUME

Anisotropy Estimation of Lower Paleozoic Shales from Northern Poland using Microseismic Data

Wojciech GAJEK

Warsaw 2021 (Issue 1)

INSTITUTE OF GEOPHYSICS
POLISH ACADEMY OF SCIENCES

PUBLICATIONS
OF THE INSTITUTE OF GEOPHYSICS
POLISH ACADEMY OF SCIENCES

Geophysical Data Bases, Processing and Instrumentation

432 (B-43)

MONOGRAPHIC VOLUME

Anisotropy Estimation of Lower Paleozoic Shales from Northern Poland using Microseismic Data

Wojciech GAJEK

Warsaw 2021

ISBN 978-83-66254-05-3 eISSN-2299-8020
DOI: 10.25171/InstGeoph_PAS_Publs-2021-001

Editorial Office
Instytut Geofizyki Polskiej Akademii Nauk
ul. Księcia Janusza 64, 01-452 Warszawa

There are more things in Heaven and Earth, than are dreamt of in your philosophy

William Shakespeare

CONTENTS

Editorial note

This publication is a revised version of my doctoral thesis submitted on September 2019 and defended on February 2020 at the Institute of Geophysics, Polish Academy of Sciences, under the supervision of Michał Malinowski, PhD.

Acknowledgements

This research was conducted within the ShaleMech Geomechanics project devoted to intensification of shale gas extraction from Polish shales, funded by the Polish National Centre for Research and Development (NCBR), grant no. BG2/SHALEMECH/14.

I would like to thank all the co-authors of my papers for their contribution. Exclusively, I wish to thank to Dr. James P. Verdon for introducing me into the shear-wave splitting topic, to Prof. Marek Jarosiński for the geomechanical interpretation of mapped microseismicity and to Dr. Jacek Trojanowski for sharing his skills in the fields of seismology and microseismicity.

The field data from borehole microseismic monitoring used in the thesis were provided by PGNiG S.A.

Collaboration with University of Bristol was supported within TIDES COST Action ES1401.

Seismic Unix and Crewes free seismic software packages and also James's P. Verdon implenentation of Neighborhood Algorithm has been used.

XRMI and cross-dipole sonic logs interpretation was performed by the Institute of Oil and Gas–National Research Institute.

Special thanks to my supervisor Dr. Michał Malinowski for all his support, advises and commitment, and also tolerance for engagement into side research topics.

List of symbols

K	Bulk modulus	
M_0	Seismic moment	
M_w	Seismic moment magnitude	
V_P	*P*-wave velocity	m/s
V_P0	Vertical *P*-wave velocity	m/s
V_{SH}	Velocity of horizontally polarized *S*-wave	m/s
V_{SII}	Velocity of *S*-wave parallel to symmetry axis	m/s
V_{SV}	Velocity of vertically polarized *S*-wave	m/s
$V_{S\perp}$	Velocity of *S*-wave perpendicular to symmetry axis	m/s
V_S	*S*-wave velocity	m/s
V_S0	Vertical *S*-wave velocity	m/s
X	Offset	m
Z	Depth	m
Θ	Phase angle	degrees
α	Fractures strike	degrees
C	Elasticity (compliance) tensor	
S	Stiffness tensor	
$\delta,\gamma,\varepsilon$	Thomsen's anisotropic parameters	
μ	Shear modulus	
ρ	Density	g/cm^3
σ	Picking uncertainty	s
τ	Stress	Pa
ξ	Crack density	
ζ	Inversion objective function	
dt	Delay time	s
e	Strain	Hz
f	Frequency	Hz
k	Scaling constant	
r	Source-receiver-distance	m
t	Time	s
u	Slowness	s/m
v	Displacement	m

List of abbreviations

1D	One-dimensional
3C	Three component
3D	Three-dimensional
AVAZ	Amplitude versus azimuth
GUI	Grafical user interface
HTI	Horizontal transverse isotropy
KB	Kelly bushing
L1	Lubocino 1 (well)
L2H	Lubocino 2 horizontal (well)
MCCF	Multichannel convolution filter
MD	Maximum difference
MV	Microseismic volume
PDF	Probability density function
PGNiG	Polskie Górnictwo Naftowe i Gazownictwo (Polish Oil&Gas company)
QC	Quality control
RMS	Root mean square
RTM	Reverse time migration
S/N	Signal to noise ratio
SH-wave	Horizontally polarized shear-wave
SRV	Stimulated reservoir volume
STA/LTA	Short-term average versus long-term average
SV-wave	Vertically polarized shear-wave
SWS	Shear-wave splitting
TI	Transverse isotropy
TOC	Total organic carbon
TTI	Titlet transverse isotropy
TVD	True vertical depth
VSP	Vertical seismic profiling
VTI	Vertical transverse isotropy
XRMI	Extended-range micro imager

Abstract

Downhole microseismic monitoring is a widely used tool for the assessment of hydraulic fracturing job effectiveness. During the process of fluid injection into the reservoir, new fractures develop due to the induced pressure, which gives rise to microseismic events. Therefore, the knowledge of an accurate velocity model is necessary in order to locate the induced microseismic events. Subsurface complexity is often raised by a horizontal layering, an intrinsic anisotropy of shales, and aligned fracture sets. That introduces anisotropic effects into the velocity field. In such a case, the anisotropy should be taken into account during the velocity model building. Otherwise, some errors will be introduced into the microseismic event locations, and hence, the interpretation of treatment effects will be biased. Therefore, this thesis is devoted to the anisotropy estimation using downhole microseismic data. It examines possible location errors caused when the anisotropy effect is not considered and proposes a technique of anisotropic velocity model inversion. It also presents field data examples of anisotropic model building and fractures characterization.

In this thesis, I introduce a new technique for anisotropic (VTI) velocity model inversion based on traveltimes of the *P*-, *SH*-, and *SV*-waves onsets and probabilistic event location algorithm. This is followed by synthetic studies showcasing errors expected in microseismic event locations when anisotropy is neglected. In addition, a feasibility study of performing quasi-real-time anisotropic velocity model inversion during an ongoing hydraulic fracturing job is included.

Then, I present two different applications of the developed methodologies to the field data from a downhole microseismic survey that was carried out to monitor hydraulic fracturing in the Lower Paleozoic gas-bearing shales in Lubocino well, Northern Poland. In the first application, the VTI anisotropic velocity model inversion using the traveltimes of perforation shots is applied. The accuracy of the model provides high-quality locations of microseismic events induced during the hydraulic treatment. Then, the locations become a basis for a detailed stage-by-stage evaluation of the stimulation performance and provide information about geological units that were successfully fractured.

In the second application, I utilize shear-wave splitting (SWS) measurements to reveal weak azimuthal (HTI) anisotropy caused by aligned fractures. The HTI is dominated by stronger VTI fabric produced by the alignment of anisotropic platy clay minerals and by thin horizontal layering. I perform the rock-physics model inversion based on SWS measurements to finally obtain an orthorhombic stiffness tensor, which links the dominant VTI fabric with HTI anisotropy produced by the presence of aligned vertical natural fracture sets in the shale-gas reservoir.

Finally, based on both synthetic and real data examples, it is concluded that taking the anisotropy into account during the velocity model building in downhole applications always enhances the accuracy of microseismic event locations, and hence, raises the quality of the final assessment of hydraulic fracturing operation. It is also demonstrated that the proposed VTI anisotropic velocity model inversion can be implemented on-site during an ongoing industry operation.

ESTYMACJA ANIZOTROPII ŁUPKÓW DOLNEGO PALEOZOIKU Z POMORZA Z WYKORZYSTANIEM DANYCH MIKROSEJSMICZNYCH

Streszczenie

Otworowy monitoring mikrosejsmiczny jest narzędziem szeroko stosowanym do oceny efektywności zabiegu szczelinowania hydraulicznego wykorzystywanego do intensyfikacji wydobycia gazu z łupków. Do lokalizacji wstrząsów mikrosejsmicznych, które są indukowane w momencie szczelinowania formacji łupkowych, konieczna jest znajomość pola prędkości fal sejsmicznych. Czynniki takie jak: różnorodność warstw skalnych, pierwotne uwarstwienie sedymentacyjne skał łupkowych czy obecność systemów spękań zwiększają złożoność górotworu. W odniesieniu do pola prędkości, powyższe czynniki skutkują obecnością anizotropii i tym samym zwiększają stopień skomplikowania pola prędkości. Konsekwentnie anizotropia powinna być uwzględniona podczas budowy pola prędkości fal sejsmicznych. Nieuwzględnienie anizotropii w obliczaniu lokalizacji wstrząsów mikrosejsmicznych może wprowadzać błędy w lokalizacji, przyczyniając się do niepoprawnej oceny efektywności zabiegu szczelinowania hydraulicznego. Niniejsza praca skupia się na zagadnieniu określania anizotropii przy wykorzystaniu danych z otworowego monitoringu mikrosejsmicznego. Rozprawa proponuje nową metodykę inwersji anizotropowego modelu prędkości. Analizowane są także błędy lokalizacji wstrząsów mikrosejsmicznych powodowane brakiem uwzględnienia efektów anizotropowych w opisie pola prędkości. Rozważania teoretyczne poparte są aplikacjami omawianych narzędzi do rzeczywistych danych z monitoringu mikrosejsmicznego w celu inwersji anizotropowego modelu prędkości oraz wyznaczania parametrów obecnych w górotworze systemów spękań.

W niniejszej pracy prezentuję nową metodykę inwersji anizotropowego (VTI) modelu prędkości fal sejsmicznych opartej na czasach pierwszych wstąpień fal *P, SH* i *SV* oraz algorytm lokalizacji wstrząsów sejsmicznych w domenie prawdopodobieństwa wraz z ich implementacją w postaci kodów obliczeniowych. Następnie przedstawiam modelowania opisujące ilościowo błędy lokalizacji, których należy się spodziewać w przypadku braku uwzględnienia anizotropii w modelu prędkości. W celu przetestowania efektywności proponowanej metodyki w warunkach polowych przeprowadzam test symulujący użycie opracowanych kodów obliczeniowych równocześnie z trwającym szczelinowaniem hydraulicznym pod kątem uzyskiwania interpretacji wyników monitoringu na bieżąco.

Kolejnymi elementami pracy są dwa zastosowania przedstawionych metod do danych z otworowego monitoringu mikrosejsmicznego prowadzonego podczas szczelinowania hydraulicznego dolnopaleozoicznych łupków gazonośnych Pomorza w otworze Lubocino. Pierwsza z aplikacji przedstawia inwersję anizotropowego (anizotropia polarna typu VTI) modelu prędkości z wykorzystaniem czasów pierwszych wstąpień strzałów perforacyjnych. Dzięki inwersji precyzyjnego modelu możliwe staje się przeprowadzenie wysokiej jakości lokalizacji wstrząsów mikrosejsmicznych, indukowanych w wyniku szczelinowania hydraulicznego. Daje to podstawy do przeprowadzenia drobiazgowej oceny efektywności zabiegu szczelinowania i uzyskania odpowiedzi na pytanie, które jednostki geologiczne zostały efektywnie zeszczelinowane. W kolejnym eksperymencie na danych rzeczywistych badam zjawisko rozszczepienia

fali poprzecznej w ośrodku anizotropowym w celu analizy anizotropii azymutalnej (HTI) generowanej przez system równoległych spękań pionowych. Anizotropia azymutalna zdominowana jest przez silniejszą anizotropię (VTI) generowaną przez teksturę skał łupkowych oraz cienkie warstwowanie poziome ośrodka skalnego. W oparciu o obserwacje zjawiska rozszczepienia fali *S* przeprowadzam inwersję modelu geomechanicznego. Wynikiem jest otrzymany ortorombiczny tensor sztywności, który łączy w swoim opisie dominującą anizotropię polarną (VTI) ze słabszą anizotropią azymutalną (HTI), powodowaną obecnością szczelin.

Na podstawie przeprowadzonych rozważań teoretycznych oraz pomyślnego zastosowania stworzonej metodyki do danych rzeczywistych stwierdzam, że uwzględnianie anizotropii podczas budowy modelu prędkości fal sejsmicznych dla zastosowań otworowego monitoringu mikrosejsmicznego każdorazowo zwiększa precyzję lokalizacji wstrząsów mikrosejsmicznych. W konsekwencji, przyczynia się to do poprawy jakości końcowej oceny efektywności zabiegu szczelinowania hydraulicznego. W oparciu o przeprowadzone symulacje dowodzę również, że stosowanie proponowanej metodyki inwersji anizotropowego (VTI) modelu prędkości jest możliwe na bieżąco w warunkach polowych i może być wykorzystywane podczas trwającego zabiegu szczelinowania hydraulicznego.

1. INTRODUCTION

1.1 Microseismic monitoring – what is it?

Both natural and anthropogenic phenomena like volcanic activity, mining or oil and gas exploration generate small earthquakes. Comparing to regular tectonic earthquakes, which can sometimes be felt or even have a devastating impact, those are most often unnoticeable for human tiny-magnitudes events with moment magnitudes below 0. Those small earthquakes are called micro-earthquakes or microseismic events. Despite their relatively tiny scale, valuable information about the subsurface can be inferred from their distribution, mechanisms, and occurrence in time. For example, in mining, they can be used as rockbursts indicators. In the case of artificial water reservoirs, the microseismic activity can be used to assess the reaction of rock masses to increased pressure. To monitor those phenomena sparse network of seismometers designed for global seismology is not enough, due to limited detectability. However, a dedicated, local network of sensitive seismic instruments can be used to record those events and provide valuable information about the phenomena occurring in the subsurface. For example, a string of seismometers a few hundred meters away from a target shale formation during a hydraulic fracturing may provide information about, e.g., locations of induced microseismic events and time evolution of fractures in a stimulated rock volume. This concept is illustrated in Fig. 1.

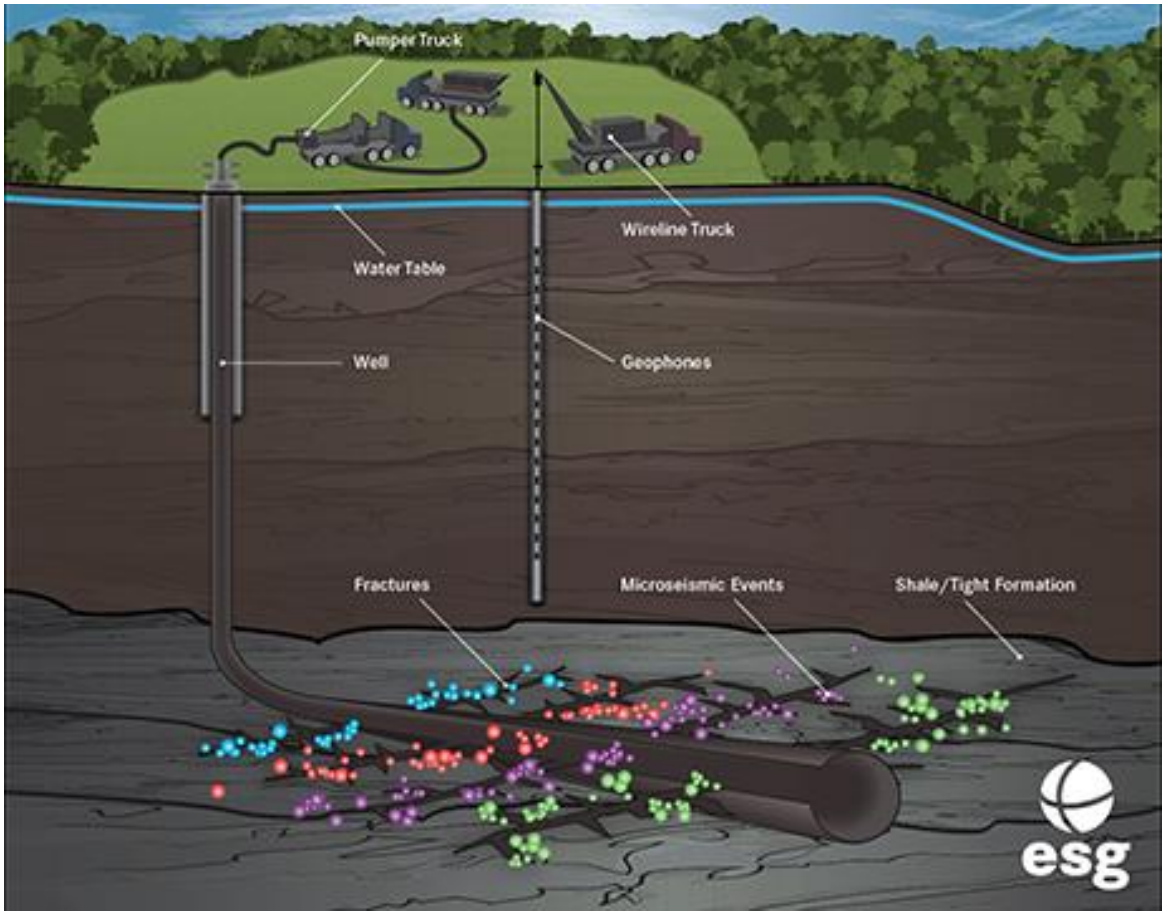

Fig. 1. A concept of a downhole microseismic monitoring of hydraulic fracturing treatment. Hydraulic stimulation induces microseismic events (dots in different colors) along generated fractures. The energy being released propagates through the subsurface and can be recorded by the geophones. Source: https://www.esgsolutions.com/sites/esgsolutions.com/files/img/microseismic-fracture-mapping-esgsmall.jpg (accessed on 5 February 2019).

The energy released during fracture opening or other phenomena acting as a seismic source (see "microseismic events" in Fig. 1) generates seismic waves, which propagate in the subsurface. The wave field is recorded by ground motion sensors located in the monitoring boreholes, mine tunnels or at the surface (see "geophones" in Fig. 1). These events, lasting milliseconds, have to be identified on multiple receivers in hours-long records containing different origin events and background noise. An event's location can be calculated based on observed time differences of various seismic waves arrivals at available receivers. The location accuracy depends on the precision of seismic waves arrivals picking in time and on the knowledge about parameters characterizing the subsurface (layering, seismic waves velocities, and anisotropy) between the source and the receivers. Then the information inferred from microseismic activity can be interpreted to conclude on phenomena taking place in the subsurface.

1.2 The aims of this thesis

In this thesis, I develop new techniques of subsurface characterization which enhance microseismic monitoring performance in the context of hydraulic fracturing. Particularly, new techniques of seismic velocities and anisotropy estimation in shales using downhole microseismic data are developed. Successful recognition of the character and the strength of the anisotropy complements a knowledge about parameters of the subsurface. On the one hand, knowing the seismic anisotropy can affect the accuracy of event locations by enhancing the velocity model precision (Yu and Shapiro 2014). On the other hand, measurements of the azimuthal anisotropy may be used to image aligned fracture systems (Schoenberg and Sayers 1995) or provide information about the orientation of the in situ stress tensor (Verdon and Wüstefeld 2013).

In the field data applications included in this thesis, a detailed study of the anisotropy allows to map microseismic events induced during a hydraulic fracturing accurately and reveals information about fractures existing in the shale gas reservoir what improves the quality of a final microseismic monitoring interpretation.

The thesis is concentrated on the following two hypotheses applicable to microseismic monitoring:

1) Accounting for anisotropy during the process of velocity model building enhances the accuracy of microseismic events locations. A single anisotropic model performs better than a set of isotropic models constructed individually for selected model space (e.g., an area of a single fracturing stage during hydraulic treatment in a shale gas reservoir where anisotropy should be expected);
2) Shear-wave splitting phenomenon occurring in the microseismic records can be utilized to measure the azimuthal anisotropy and estimate fracture density and their orientation within the reservoir.

In order to support those two hypotheses I show synthetic examples and field data applications. First, I present a comparison of microseismic event locations errors resulting from isotropic and anisotropic velocity models inversions, providing means for real data inversion to follow.

Next, the Lubocino case study presents a complete procedure from the initial data processing of the microseismic dataset up to the interpretation of the obtained results. The workflow starts from standard microseismic data processing. Then a 1D velocity model accounting for effective VTI anisotropy (vertical transverse isotropy) is to build and used to accurately map locations of microseismic events induced during the hydraulic fracturing improving the quality of treatment performance evaluation, which is one of the major tasks of microseismic monitoring.

Afterward, measurements of significantly strong shear-wave splitting observed in waveforms of microseismic events are taken. Finally, the obtained VTI parameters together with

shear-wave splitting measurements are utilized in an inversion of an orthorhombic stiffness tensor to identify azimuthal anisotropy revealing information about density and orientation of vertical fracture sets within a dominating VTI media in the shale-gas reservoir.

The most important new technique I developed here is an anisotropic VTI velocity model inversion accounting for traveltimes of all three waves *P*, *SH*, and *SV*, and providing seismic velocities for each layer defined in the model and Thomsen's anisotropic parameters. Other secondary developments are a probabilistic event location algorithm allowing for more reliable assessment of a stimulation performance and a successful application of shear-wave splitting observations for an orthorhombic stiffness tensor inversion by using constraints on VTI fabric parameters derived from different methods in challenging narrow-azimuth observation environment, where weaker azimuthal anisotropy is dominated by VTI fabric.

1.3 Summary of the following chapters

The thesis is composed of five chapters following this Introduction:

Chapter "Theory" provides a theoretical introduction into well established principles and methods being used throughout the thesis and their recent advances such as the phenomena of seismic wave propagation, the definition of anisotropy and its influence on seismic wave propagation, shear-wave splitting and its applications, techniques of velocity model inversion and earthquake location, etc.

In Chapter "Developed methodology and synthetic examples" I describe new methods created by me or already established methods but modified by me, which are used in this research, supplemented with their synthetic tests. A new technique for anisotropic velocity model inversion and probabilistic event location algorithm are introduced. It also contains a synthetic study of expected errors in microseismic event locations when anisotropic media is represented by a number of isotropic models, which is a standard procedure in the industry together with a feasibility study of quasi-real-time anisotropic velocity model inversion during an ongoing hydraulic fracturing job.

Then two field data applications of developed methodologies are presented in the next two chapters. "Building an anisotropic velocity model for microseismic events location" presents a workflow towards the accurate location of events induced during the hydraulic fracturing. The complete data processing scheme starts with data filtering, perforation shots identification, and event detection. The key point is a VTI anisotropic velocity model inversion using the traveltimes of perforation shots. The accuracy of the model provides high-quality locations of microseismic events induced during the hydraulic treatment, which become a basis for a detailed stage-by-stage evaluation of the stimulation performance and provide information about successfully fractured geological units.

In Chapter "Estimating fracture parameters based on shear-wave splitting" shear-wave splitting measurements are utilized to reveal weak HTI anisotropy dominated by stronger VTI fabric produced by the alignment of anisotropic platy clay minerals and by thin horizontal layering. The rock-physics model inversion based on shear-wave splitting measurements is constrained by background VTI parameters from other geophysical methods: microseismic velocity model inversion (previous chapter), 3D reflection seismic, and borehole cross-dipole sonic logs. Finally, an orthorhombic stiffness tensor is inverted, linking the dominant VTI fabric with HTI anisotropy produced by the presence of aligned vertical fracture sets in the shale-gas reservoir.

In the last chapter I summarize the thesis with conclusions.

The majority of the content of this thesis has been already published as articles or extended abstracts with me being the first author in all of them. Both described field data applications have been published as a two-part peer-reviewed article in *Interpretation*, in a special issue

titled *Characterization of potential Lower Paleozoic shale resource play in Poland*, and Chapters 4 and 5 are their elaborated versions, respectively: Gajek et al. (2018b,c).

Some of the newly developed methodologies with fragments of field applications have been published as extended abstract from well-recognized among oil and gas industry researchers EAGE conferences: Gajek et al. (2016, 2017, 2018a).

1.4 Geological setting

Gas-bearing shale formations in Poland are Lower Paleozoic shales deposited on the margin of the East European Craton. They occupy three different basins, Baltic, Podlasie, and Lublin, which differ in terms of their tectonic deformation (Fig. 2).

The study area of this research belongs to the Baltic Basin, which is the most prospective area for unconventional resources in shale formations (Podhalańska et al. 2016). It is located near Lubocino, Northern Poland, in the former exploration block of the Polish Oil and Gas Company (PGNIG SA), where one of the first hydraulic fracturing treatments of gas-bearing shales in Europe was carried out in 2013.

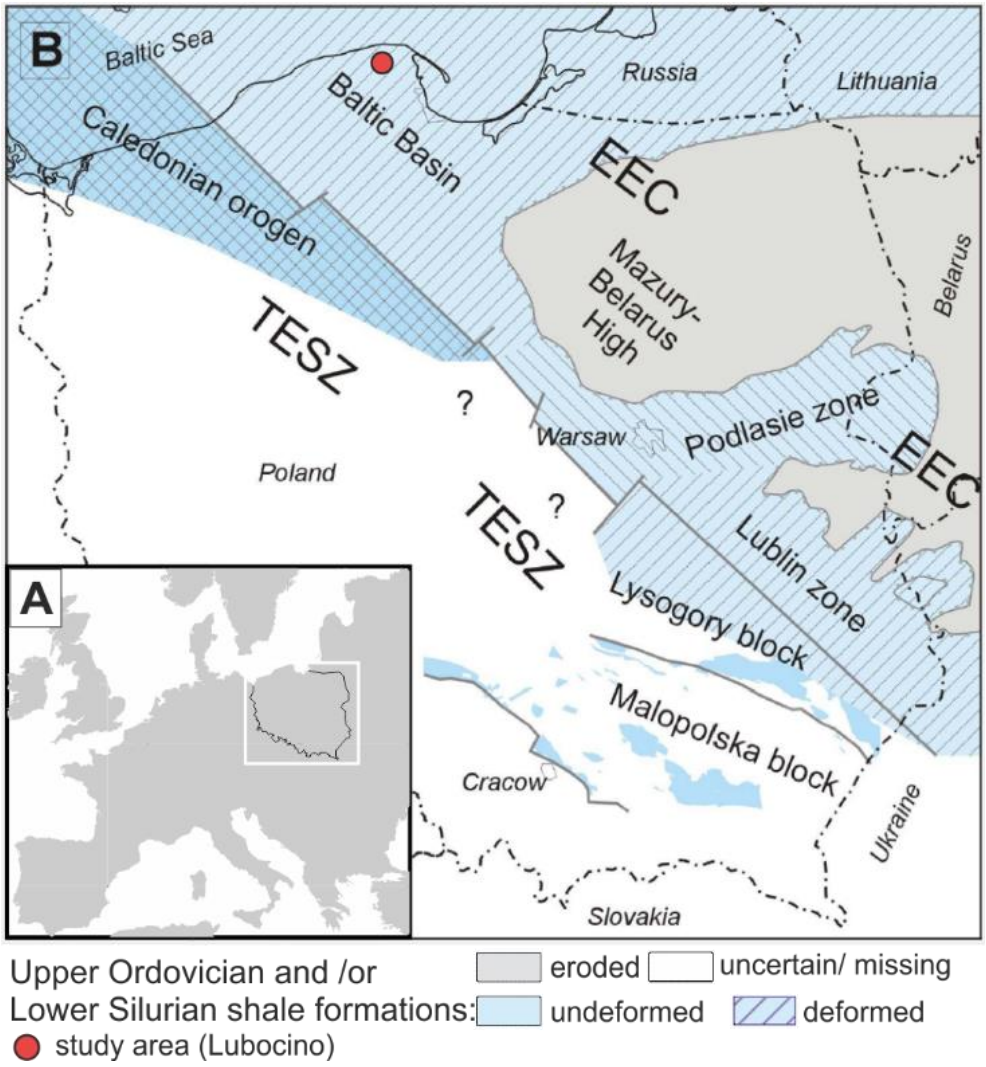

Fig. 2. Location of the study area. Lubocino – red dot, locations of the Lower Paleozoic sedimentary basins (Baltic, Lublin, and Podlasie) and lateral extent of the Lower Silurian and Upper Ordovician shale formations in Poland. (a) Contours of the Republic of Poland in Europe, and (b) location on the Lower Paleozoic sedimentary basins in Poland and area of occurrence of the Lower Silurian and Upper Ordovician shales (after Poprawa 2010; Cyz and Malinowski 2018).

The TOC-rich, most promising intervals with high contents of organic matter (type II kerogen) and silica are the Lower Silurian shales (Jantar member) and the Upper Ordovician shales (Sasino formation) (Krzemiński and Poprawa 2006; Modliski and Podhalaska 2010; Poprawa 2010). However, their thickness is limited to 40 m altogether, and they are deeply buried (at almost 3 km depth) which makes their exploitation challenging. Gas-bearing shale intervals are separated with an 8 m thick barrier made of marls called Prabuty formation. They are capped by shales belonging to the Pelplin and Paslek formations and limited by Kopalino limestones from the bottom. Deviated borehole Lubocino 2H was drilled into the thicker gas-bearing Sasino formation and hydraulic fracturing was performed (6 stages).

1.5 Data used in this research

The data were provided by PGNiG in the frame of the SHALEMECH project. It consists of a dataset from downhole microseismic monitoring from Lubocino 1 (or L1) observation well located nearby the treatment well Lubocino 2H (or L2H) (Fig. 3), geophysical well logs and reports from service company responsible for on-site microseismic monitoring during the hydraulic fracturing job. As a test site, the vertical Lubocino 1 well was well-probed with many geophysical and geologic measurements, including sonic logs, gamma, density, and rich dataset of core samples.

In order to monitor microseismic activity during the hydraulic treatment of the horizontal Lubocino 2H well, an 11-receiver string equipped with three-component geophones was installed in a vertical Lubocino 1 observation well 150–300 m above the target shale formation and 250–700 m horizontally from the perforation shots. The instrument spacing was 15 m, and the length of a tool was 150 m (Fig. 4). The sampling frequency was 2666,(6) Hz.

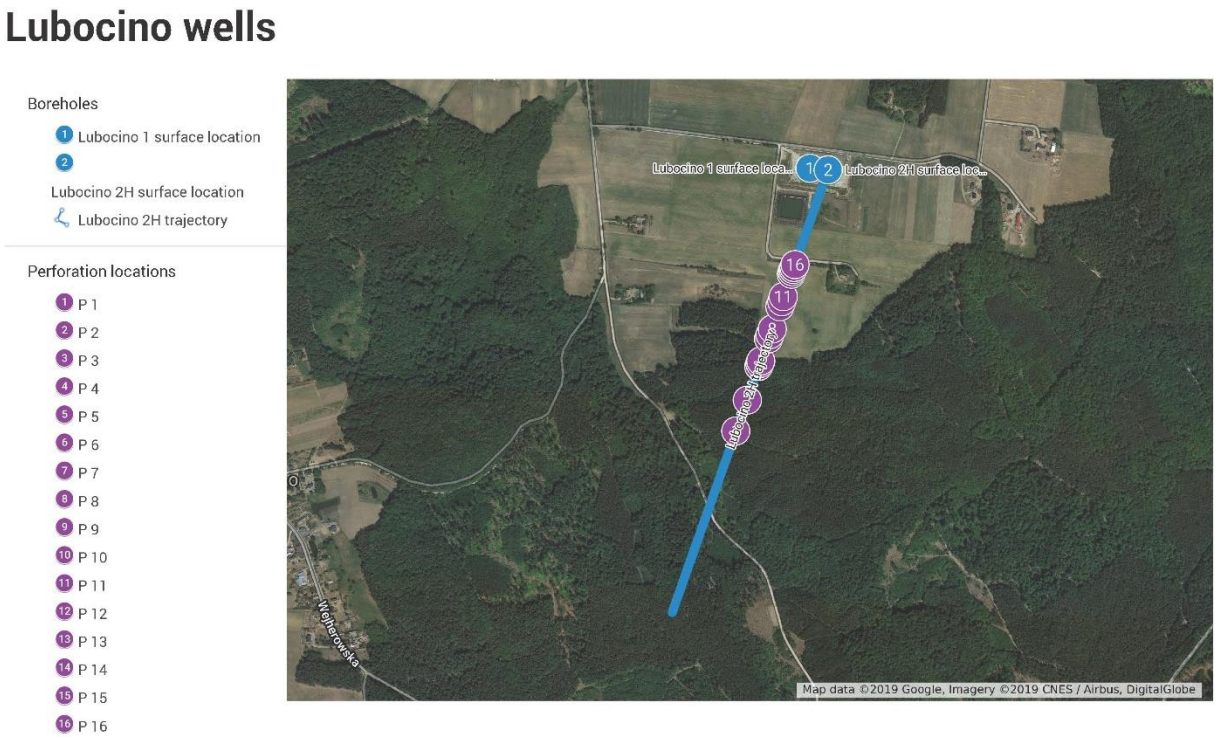

Fig. 3. Detailed surface location of vertical observation well Lubocino 1 – blue dot labeled 1; surface location of horizontal treatment well Lubocino 2H – blue dot labeled 2; projection of Lubocino 2H trajectory – blue line; and locations of all 16 perforation shots – purple dots. Source: https://www.google.com/maps.

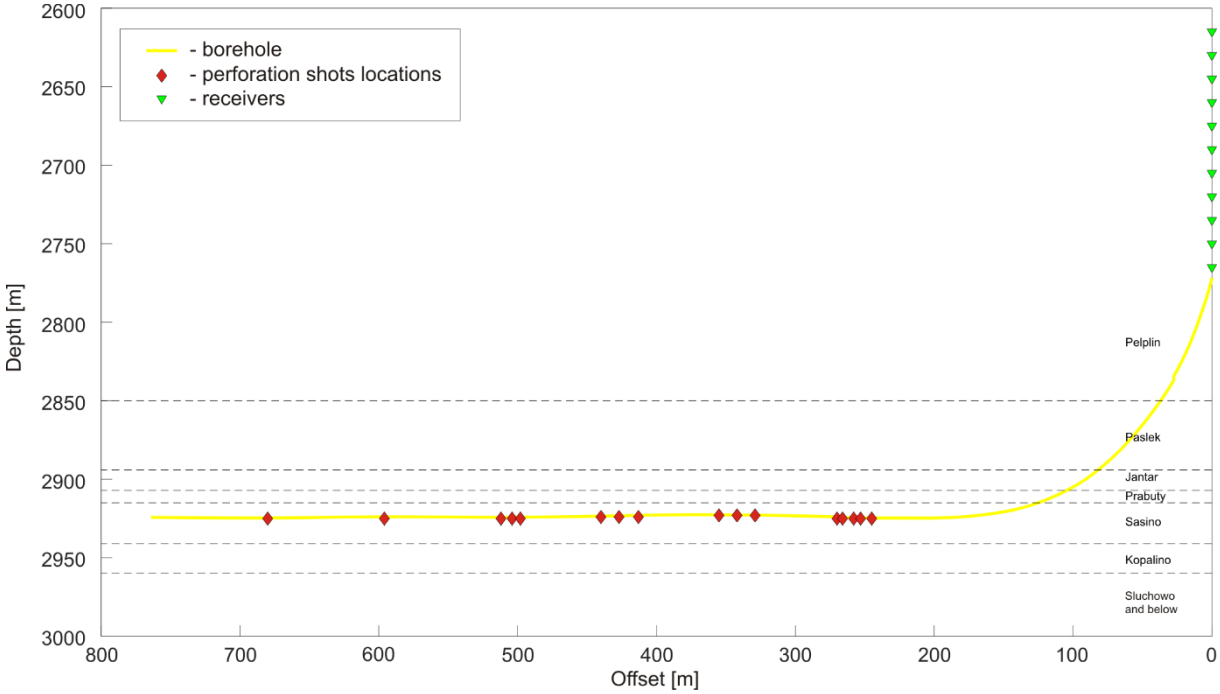

Fig. 4. Vertical cross-section showing microseismic monitoring geometry. Borehole trajectory – yellow solid line; receivers positions – green triangles; locations of all 16 perforations – red diamonds; sedimentary units intervals – black dashed line; depth scale in TVD from KB. Gas-bearing units are Sasino and Jantar.

The microseismic monitoring network was operating from 28 December 2012 to 11 February 2013, being active only at specific time intervals. Due to technical issues, a total number of only six fracturing stages was performed every few days, containing a total number of 16 perforation shots. During the time of the experiment, another network located at the surface was operating, but was not able to register any microseismic events (Wandycz et al. 2018) and is not a part of this dataset.

The downhole microseismic dataset was used by Pasternacki (2016) together with reflection seismic survey. Pasternacki performs fracturing job assessment and uses local, isotropic velocity models for microseismic events location, while in this thesis, I focus on anisotropy estimation and analyze location error resulting from the usage of isotropic velocity models.

2. THEORY

The following section provides a theoretical introduction to well-established principles and methods being used throughout the thesis. Methods already known but expanded or modified by me are included in Chapter 3.

The chapter starts from covering the topic of the seismic wave propagation in anisotropic media, with a focus on transversely isotropic (TI) media. It is supplemented by a description of associated concepts including the concept of Thomsen parameters for a simplified description of seismic velocities, the concept of weak anisotropy approximation and a comparison between exact and approximate solutions of seismic waves velocities in VTI media.

Afterward, a problem and strategies of an earthquake location are explained, followed by the description of different techniques for computation of the traveltimes of seismic waves. Next, a problem of determining the velocity field by velocity model inversion regarding microseismic application is addressed.

Finally, the phenomenon of a shear-wave splitting (SWS) is described, followed by an introduction to methods of SWS measurements. Lastly, the introduction to rockphysics model inversion using the measurements of shear-wave splitting is covered.

2.1 Seismic wave propagation in anisotropic media

Seismic anisotropy is defined as the dependence of seismic velocity upon angle (Rudzki 1911; Thomsen 1986). Its presence influences seismic wave propagation, and hence, it should be taken into account during data processing and imaging, since most rocks display some degree of seismic anisotropy.

There are numerous well-known mechanisms causing anisotropy at various scales, including: preferred mineral or crystal orientation (Johnston and Christensen 1995; Lonardelli et al. 2007; Hall et al. 2008), clay particle alignement (Vernik and Milovac 2011), sedimentary layering (Backus 1962; Liu and Martinez 2014), aligned fracture sets (Hudson 1981; Narr et al. 2006), and the anisotropic stresses (Lynn and Thomsen 1986; Verdon et al. 2008).

Accounting for seismic anisotropy requires an extra effort of introducing more elements into the problem description, which, in turn, increases calculations complexity and raises their computational cost. Hence, sometimes, the anisotropy is purposely omitted and simpler, but less accurate, isotropic solutions are used. Moreover, the anisotropy itself can be introduced either in a simplified or complex way. In order to provide some insight into various descriptions of anisotropic media, a base for calculation of seismic velocities has to be given first.

The equation of motion relates a displacement of particle to a stress:

$$\rho \frac{\partial^2 v_i}{\partial t^2} = \frac{\partial \tau_{ij}}{\partial x_j} \tag{1}$$

where v is the displacement vector in time t and space x, τ is the stress vector, and ρ is the density of the material. Indices i and j represent different directions of stress and displacement.

The strain e is related to the stress τ by the elasticity tensor C, described by the Hooke's law (Hooke 1678):

$$\tau_{ij} = C_{ij\,mn} e_{mn} \tag{2}$$

Seismic waves propagation can be described by the wave equation, which combines the equation of motion with the Hooke's law.

$$\rho \frac{\partial^2 v_i}{\partial t^2} = C_{ij\,mn} \frac{\partial^2 v_m}{\partial x_n \partial x_j} \tag{3}$$

The notation of $3 \times 3 \times 3 \times 3$ elasticity tensor C_{ijmn} having four indices can be simplified to just two because of symmetry of strain and stress. Hence, a 6×6-matrix notation, the Voigt notation, for the elasticity tensor C_{kl} can be used. Therefore, the index combinations of ij and mn are replaced by k and l indices between 1 and 6 (Voigt 1910).

Solving the wave Eq. (3) to predict seismic wave propagation requires to know the media, characterized by the elasticity tensor and density. Here, in order to keep a compact form of a thesis, only the most important formulas are shown. For a step-by-step introduction to elasticity tensor derivation and wave field a reader may be referenced to, e.g., Danek et al. (2010) or Riedel (2015). For the isotropic medium the elasticity tensor C^{ISO} is defined by only two independent elements, related to bulk (K) and shear moduli (m) of the medium (Pujol 2003), (for clarity, repeated elements are given in brackets):

$$C^{\mathrm{ISO}} = \begin{bmatrix} (C_{33}) & (C_{33}-2C_{66}) & (C_{33}-2C_{66}) & 0 & 0 & 0 \\ & (C_{33}) & (C_{33}-2C_{66}) & 0 & 0 & 0 \\ & & C_{33} & 0 & 0 & 0 \\ & & & (C_{66}) & 0 & 0 \\ & & & & (C_{66}) & 0 \\ & & & & & C_{66} \end{bmatrix} \tag{4}$$

$$C_{33} = K + \frac{4\mu}{3} = \rho V_P^2 \qquad \text{and} \qquad C_{66} = \mu = \rho V_S^2 \,, \tag{5}$$

where K is a bulk modulus, μ is a shear modulus.

However, in the case of anisotropic media, solving the wave equation becomes complicated, because of more complex elasticity tensor. In the most complex media (triclinic symmetry), the elasticity tensor is characterized by 21 different elements. For seismic applications, when anisotropy is considered, it is usually a polar anisotropy, generally called transverse isotropy (TI) or an orthorhombic symmetry, with 5 or 9 independent elements of the elasticity tensor, respectively (Tsvankin and Grechka 2011). TI is the simplest type of anisotropy applicable to geophysical problems with the velocity of seismic waves at a given point being dependent on the angle between the raypath and the axis of symmetry only.

There are various applications of TI, related to the orientation of anisotropic media in the subsurface, referred to as: vertical transverse isotropy (VTI), horizontal transverse isotropy (HTI), and tilted transverse isotropy (TTI). In the VTI medium, wave velocities are independent of azimuth and depend solely on the angle of ray propagation from vertical. The VTI medium is a proper description for layered, horizontally deposited sediments like thin-bed sequences (Backus 1962) or unfractured shales, which exhibit intrinsic anisotropy due to the alignment of platy, anisotropic clay minerals within the sedimentary layers (Kendall et al. 2007; Vernik and Milovac 2011). Five independent parameters of the elasticity tensor C_{VTI} describe a VTI (in general TI) medium at a given location (Rudzki 1911; Thomsen 2002):

$$C^{\mathrm{VTI}} = \begin{bmatrix} C_{11} & C_{11}-C_{66} & C_{13} & 0 & 0 & 0 \\ & (C_{11}) & (C_{13}) & 0 & 0 & 0 \\ & & C_{33} & 0 & 0 & 0 \\ & & & C_{44} & 0 & 0 \\ & & & & (C_{44}) & 0 \\ & & & & & C_{66} \end{bmatrix} \tag{6}$$

Horizontal-transverse isotropy (HTI) describes a medium where the velocity depends solely on the azimuth of seismic wave propagation. HTI can be created by the presence of aligned vertical fracture sets in the isotropic medium (Gupta 1973; Crampin et al. 1980). Mathematically, the HTI symmetry is the VTI system rotated by 90° from vertical. An effect of any other rotation from vertical, called tilted transverse isotropy (TTI), may be used to describe sedimentary rocks deposited on an inclined basement or tilted by tectonic forces.

Sedimentary rocks may contain a combination of VTI and fractures, e.g., shales with vertical fractures set, leading to orthorhombic symmetry (Tsvankin 1997; Grechka 2007), described by 9 independent elements of the elasticity tensor C^{ORT}:

$$C^{\mathrm{ORT}} = \begin{bmatrix} C_{11} & C_{12} & C_{13} & 0 & 0 & 0 \\ & C_{22} & C_{23} & 0 & 0 & 0 \\ & & C_{33} & 0 & 0 & 0 \\ & & & C_{44} & 0 & 0 \\ & & & & C_{55} & 0 \\ & & & & & C_{66} \end{bmatrix} \tag{7}$$

Although these parameters give very complex general equations for seismic wave velocities, a handy simplified notation, using so-called Thomsen's parameters, exists (Thomsen 1986), and is ubiquitously used by the industry. Thomsen's parameters for the TI medium are V_P0 and V_S0, describing longitudinal and shear waves velocities parallel to the symmetry axis (vertical, in VTI case), and nonzero dimensionless parameters ε, γ and δ, describing the velocity dependence on the propagation angle. One will still obtain velocities for isotropic medium, after reducing all the Thomsen's parameters to zero. Importantly, γ exists only in a formula for a fast *S*-wave.

$$\varepsilon = \frac{C_{11}-C_{33}}{2C_{33}} \tag{8}$$

$$\delta = \frac{(C_{13}+C_{44})^2-(C_{33}-C_{44})^2}{2C_{33}(C_{33}-C_{44})} \tag{9}$$

$$\gamma = \frac{C_{66}-C_{44}}{2C_{44}} \tag{10}$$

Therefore, to describe a homogeneous anisotropic medium of the simplest form (VTI), one needs five parameters instead of two required for the isotropic medium. Consequently, it is more difficult to fit the appropriate model using inverse methods, when accounting for anisotropy of any complexity.

Introducing the handy notation does not simplify the calculations, yet. Formulas to calculate the exact direction-dependent phase velocities for each wave in VTI media still remain complex (Thomsen 2002):

$$V_P^2(\Theta) = V_P0^2(1 + \varepsilon \sin^2\Theta + D) \tag{11}$$

$$V_{S\perp}^2(\Theta) = V_S0^2\left(1 + \varepsilon\frac{V_P0^2}{V_S0^2}\sin^2\Theta - \frac{V_P0^2}{V_S0^2}D\right) \tag{12}$$

$$V_{S\parallel}^2(\Theta) = V_S0^2(1 + 2\gamma\sin^2\Theta) \tag{13}$$

where

$$D = \frac{\left(1-\frac{V_S0^2}{V_P0^2}\right)}{2}\left[\left(1 + \frac{4(2\delta-\epsilon)}{\left(1-\frac{V_S0^2}{V_P0^2}\right)}\sin(\Theta)^2\cos(\Theta)^2 + \frac{4\left(1-\frac{V_S0^2}{V_P0^2}+\epsilon\right)\epsilon}{\left(1-\frac{V_S0^2}{V_P0^2}\right)^2}\sin(\Theta)^4\right)^{\frac{1}{2}} - 1\right] \tag{14}$$

Nevertheless, some further simplifications can be made, which allow for linearization of the exact solutions, but impose some errors on the results. Of course, any modification to the formula introduces error in the solution. However, up to some magnitude of anisotropy, those errors can be neglected. This is why, the so-called weak anisotropy assumption (Thomsen 1986), allowing to use linearized, hence, much simpler velocity formulas, is made so often. As a proxy, errors can be assumed proportional to the magnitude of anisotropy, i.e. value of Thomsen's parameters. Simplified formulas for velocities of seismic waves under the weak anisotropy assumption for polar anisotropy (Thomsen 1986) are presented here:

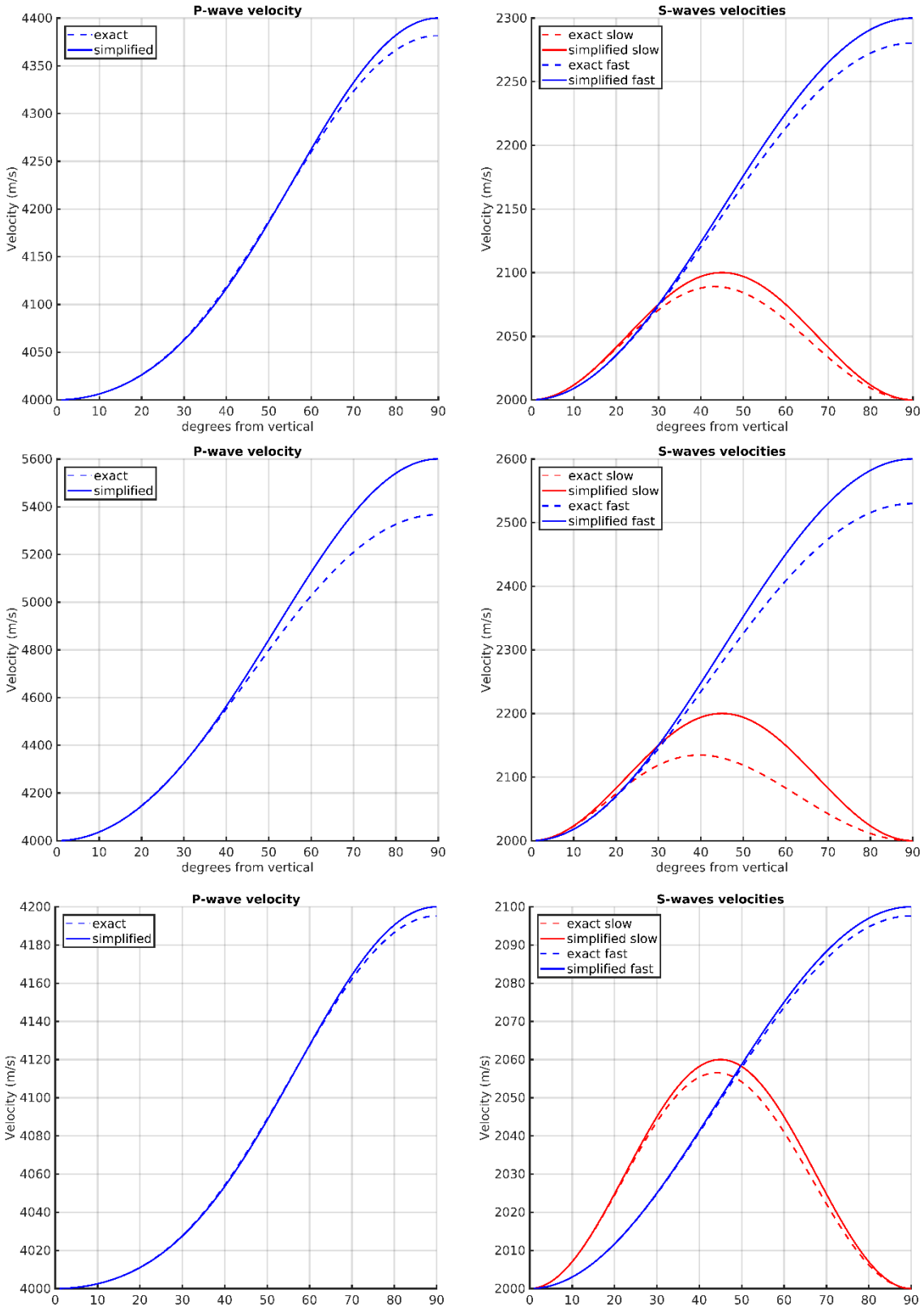

Fig. 5. Comparison of exact and simplified solutions of *P*-, *SH*-, and *SV*-waves velocities for media with various strength of anisotropy, while velocities are kept constant as: V_P0 = 4000 m/s, V_S0 = 2000 m/s. Panels a) and b) showcase relatively weakly anisotropic VTI medium, parametrized by: $\varepsilon = \gamma = 0.05$, $\delta = 0.02$. Panels c) and d) showcase intermediately anisotropic VTI medium, parametrized by: $\varepsilon = 0.1$, $\gamma = 0.15$, $\delta = 0.05$. Panels e) and f) showcase relatively strongly anisotropic VTI medium, parametrized by: $\varepsilon = 0.4$, $\gamma = \delta = 0.3$.

$$V_P(\Theta) = V_P0(1 + \delta\sin^2\Theta\cos^2\Theta + \epsilon\sin^4\Theta) \tag{15}$$

$$V_{S\perp}(\Theta) = V_S0\left(1 + \left(\frac{V_P0}{V_S0}\right)^2(\epsilon - \delta)\sin^2\Theta\cos^2\Theta\right) \tag{16}$$

$$V_{S\parallel}(\Theta) = V_S0(1 + \gamma\sin^2\Theta) \tag{17}$$

There are no exact bounds for Thomsen's parameters limiting the weak anisotropy condition given in the literature. Thomsen (1986) defines the weak polar anisotropy conditions to be $\varepsilon, \gamma, \delta \ll 1$. Some authors report more strict limits, e.g., Pšenčík and Martins (2001) claims that strong anisotropy should be considered if Thomsen's parameters exceed a value of 0.25. Still, any modification to the formulas results in some error, when comparing to exact solutions.

It should be mentioned that the anisotropic medium affects not only the velocity but also the polarization of propagating seismic waves (Crampin et al. 1982). For example, in the case of *P*-wave, the motion of the particles will not be parallel to the propagation direction. Instead, it will marginally deviate, and hence, be called quasi *P*-wave or *qP*-wave. Therefore, in anisotropic media, the seismic waves should be referred to as *qP*-, *qSH*- and *qSV*-waves. Nevertheless, for the brevity of this thesis, the qualifiers in quasi *P*-wave and quasi *S*-waves will be omitted.

In order to provide an insight into error magnitudes, velocities for three subjectively chosen anisotropic VTI media were modeled using both exact (Eqs. (11)–(13)), and simplified (Eqs. (15)–(17)) formulas. Throughout three modeled examples, velocities were kept constant as: V_P0 = 4000 m/s, V_S0 = 2000 m/s, while Thomsen's parameters were being gradually increased, to mimic relatively weak, intermediate, and strong VTI anisotropy. The modeling results are presented in Fig. 5, while exact parameters for each of the scenarios are listed in Table 1.

For each of the scenarios, a parameter of maximum difference (MD) between exact and simplified solution, for each wave was calculated using Eq. (18). All MDs for different cases are listed in Table 1.

$$\mathrm{MD} = \max\left(\frac{|V_{\mathrm{exact}}(\Theta) - V_{\mathrm{simplified}}(\Theta)|}{V_{\mathrm{exact}}(\Theta)}\right)\cdot 100\% \tag{18}$$

From examining Fig. 5 it can be inferred, that differences between exact and simplified solutions change with the strength of anisotropy and with incidence angle. For both *P*- and fast *S*-wave, the largest differences are observed for horizontal propagation, while for slow *S*-wave, at the angle of 45° from vertical.

Table 1

Exact parameters of differently anisotropic media used in the modeling, together with MDs for each wave

	Anisotropy			Maximum differences [%]		
Case	ε	γ	δ	*P*-wave	Fast *S*-wave	Slow *S*-wave
Weak	0.05	0.05	0.02	0.1	**0.2**	0.1
Intermediate	0.1	0.15	0.05	0.4	0.6	**0.9**
Strong	0.4	0.3	0.3	**4.4**	3.6	2.8

Note: Highest MD values for each scenario were given in bold. Velocities were kept constant as: V_P0 = 4000 m/s, V_S0 = 2000 m/s for all cases.

For weakly anisotropic medium MD is equal to only 0.2% (for fast *S*-wave) (Fig. 5a,b). For intermediate anisotropy MD equals 0.9% (for the slow *S*-wave) (Fig. 5c,d). When considering strong anisotropy, MD rises up to 4.4%, and the *P*-wave solution becomes most affected (Fig. 5e,f).

A set of Thomsen's parameters called intermediate case is later used for the synthetic study of expected errors in microseismic event locations when anisotropic media is being represented by number of isotropic models (Chapter 3).

2.2 Problem of earthquake location using a downhole monitoring array

Seismic events, most commonly known as earthquakes, but also as microearthquakes, mining blasts, icequakes, etc., are being detected by the networks of seismometers all around the world. Numerous detection algorithms based on different signal characteristics exist, such as amplitude (threshold trigger, e.g. Havskov and Alguacil 2004), frequency content (Shensa 1977), signal envelope (STA/LTA, e.g. Allen 1978; Houliston et al. 1984; Trnkoczy 1999), fractal dimension (Tosi et al. 1999), correlation with master events (Withers et al. 1999), to name the most popular. Event detection and trace preconditioning became separate research fields in seismology, and hence, I will not cover those topics extensively, since event detection is beyond the scope of this thesis. Instead, I refer to overviews and comparisons of different methods presented by, e.g., Withers et al. (1998) or Sharma et al. (2010).

Once the events were detected, they need to be located in order to provide valuable geological information. For this purpose, arrival times of seismic waves are required (Geiger 1912; Gibowicz and Kijko 2013). Traveltime picking or first-breaks picking procedure involves determining a correct arrival time of seismic phases at seismic stations, that build up a seismic network. It can be challenging in case of noisy environment or weak signals, which are typical conditions for hydraulic fracturing jobs (Vera Rodriguez et al. 2012; Cesca and Grigoli 2015; Sabbione et al. 2015; Huang et al. 2017). Low accuracy of first breaks will then lead to significant location errors (Eisner et al. 2011). Picking can be performed manually or automatically (based on cross-correlation (e.g. Senkaya and Karsli 2014), nowadays often employing various machine learning techniques (e.g. Murat and Rudman 1992; Chen 2020)), however, both methods usually impose some errors, due to, e.g., inconsistent phase picking or false phase recognition.

In principle, location procedure requires to find a cell within a model space, at which calculated traveltimes are equal (or, in practice, close enough) to the observed ones.

In a homogeneous 2-D medium with wave velocity V and slowness u defined to be $u = 1/V$, the arrival time, t_{obs}, at an observation point x_{obs}, z_{obs} of a signal emitted at origin time t_0 from a source location at offset x_0 and depth z_0 is:

$$t_{\text{obs}} = t_0 + u\,[(x_{\text{obs}} - x_0)^2 + (z_{\text{obs}} - z_0)^2]^{\frac{1}{2}} \tag{19}$$

The equation above (19) is formed for the simplest, homogeneous slowness field, when rays between source and receiver are straight. Nevertheless, any change in spatial position of the source introduces non-linear change in the observed traveltime. When the slowness field becomes inhomogeneous e.g., layered, the arrival time formula needs to be updated to:

$$t_{\text{obs}} = t_0 + \int_{r_0(s)} u(r_0)ds \tag{20}$$

where $r_0(s)$ denotes a distance s between source and receiver along a ray path r_0. Then, any modification to spatial source coordinates changes a ray path r_0. Thus, a problem of seismic event location is a non-linear problem (Lomax et al. 2009).

Therefore, to successfully locate an event the knowledge about three elements is necessary: observed traveltimes of the event, a velocity model of the subsurface together with associated

traveltimes, and a geometry of an observation network. Coordinates of seismometers are usually well-known, and observed traveltimes are also available, providing the event was detected. The next section will then discuss the calculation of theoretical traveltimes.

2.2.1 Traveltime calculation

Theoretical (i.e., calculated or modeled) traveltimes are in most of the cases necessary to obtain the location of the seismic event. There are methods, based on full waveform inversion, that do not need exact traveltimes, such as reverse time migration (RTM) (McMechan 1982; Fink 1999), which backpropagates recorded waveforms in time, to the point of maximum energy focus, which is considered as a source location. Nevertheless, those methods are rarely used in real data applications because of poor performance with noisy data, but also due to their complexity, high computational costs, and hence low applicability in complex geology. The most common methods are then the traveltime based approaches, which are more efficient but require accurate traveltimes.

For the most common location approach, theoretical traveltimes for an assumed velocity model between receivers and every possible source location are necessary for each seismic wave arrival being considered by the location algorithm. A set of traveltimes for each receiver, once obtained, can be stored as so-called look-up tables in order to be easily accessible when locating numerous events.

There are two families of methods being used to model the traveltimes. These are ray methods and eikonal methods.

Ray methods provide traveltime for a ray path between source and receiver, assuming the infinitely high frequency of waves propagating in a smooth velocity model (Červenỳ and Pšenčík 1979; Aki and Richards 1980). This technique is most efficient when applied to simple geology being then solved analytically. For more complex, 3D or detailed structures, iterative ray-tracing techniques are used to determine the traveltime, by narrowing the initial ray shooting angle towards the desired target point, which can become time-consuming (Virieux and Farra 1991). Ray methods can support wave conversion, but do not account for diffracted arrivals (which in some cases are the first arrivals), except of some special techniques like two-point (Um and Thurber 1987), perturbation (Farra and Madariaga 1987) or ray-bending (Wesson 1971; Chander 1975; Julian and Gubbins 1977). Another drawback is that rays tend to avoid low-velocity zones, and preferentially sample high-velocity anomalies. In general, despite their simplicity, computational effort to calculate traveltimes in complicated geology using ray methods may become significant. However, thanks to the rise of computing power, they are widely used in different scales for seismological (Rawlinson et al. 2010) and industrial applications (e.g. Zelt and Barton 1998).

Eikonal methods provide traveltimes of the first arriving phase by propagating the high-frequency wavefront through the whole velocity model grid using finite difference approximation by iteratively solving the eikonal equation (Vidale 1988; Thurber and Kissling 2000; Rawlinson and Sambridge 2004). In each subsequent iteration, a large number of Huygen's sources are considered along the actual wavefront, emitting the wave further into the model space. Due to the wavefront evolution over time, calculation of the traveltime is possible only in grid cells adjacent to Huygen's sources. Hence, some iteration strategies can be employed to optimize the whole workflow, designed either in more intelligent, e.g., fast marching method (Sethian 1996) or robust manner, e.g., fast sweeping (Zhao 2005) or brute-force mapping (Schneider Jr. et al. 1992). This method is computationally efficient and applicable to complex, 3D velocity fields (Gillberg et al. 2012). A particularly important feature of eikonal solvers is that they provide traveltimes for whole model space with single modeling by assuming reciprocity, which makes them well-suited for location purposes (Lomax et al. 2009). A concise

description of eikonal methods can be found in a PhD thesis of Marko Riedel (Riedel 2015), whose code I applied for traveltime computation in my research.

2.2.2 Traveltime-based velocity model inversion

Each of the methods introduced in the previous section requires a velocity model to compute the traveltimes. Hence, the velocity model building procedure is a crucial step in seismic applications, because it contributes to the final position of events or reflectors (Guo and Fagin 2002; Maxwell et al. 2010). Contrary to active seismic methods, which know the source positions and tries to obtain an image of the subsurface, passive seismic methods assume a known propagation medium to locate and characterize the microseismic sources (Bardainne and Gaucher 2010). Therefore, the velocity field needs to be obtained prior to microseismic sources location.

The velocity field is initially unknown and needs to be constructed using available information. It can benefit from various information, such as geological models, borehole trajectory profiling, borehole sonic logs, perforation shots, additional surface or borehole seismic data, and core analysis (Maxwell et al. 2010). Accuracy of the computed microseismic source locations obviously depends on the accuracy of temporal and directional observations from the seismograms, as well as the accuracy of the velocity model (e.g. Eisner et al. 2009; Maxwell 2009). Furthermore, the velocity model also has relevance to mechanical properties, that can be used to investigate the geomechanical aspects of the hydraulic fracturing (e.g. Hudson 1981; Verdon and Wüstefeld 2013; Gajek et al. 2018c).

A typical workflow for velocity model construction is to begin with a geologically relevant earth model and then populate the model with upscaled values from a dipole sonic log. Since microseismic data normally contains both compressional and shear waves, both *P*- and *S*-wave velocities are required for the source location (Maxwell et al. 2010). In the case of anisotropic medium, both *S*-wave modes should be accounted (Grechka and Yaskevich 2013). Some form of a check shot is then desired to validate the apparent velocity of the arrival times of various phases. Additional constraints can be imposed if the check shot detonation time is recorded; however, due to technical difficulties usually only its position is provided. In downhole microseismic monitoring, check shots are often perforation shots in a wellbore about to be fractured (Grechka and Heigl 2017). In that case positions of perforation shots as well as receivers are known from borehole trajectory, and a goal is to find the best fit between observed and modeled traveltimes for locations containing check shot sources.

Having information about positions of both sources and receivers, and about the respective traveltimes, an inverse problem has to be solved to obtain a velocity model. Due to the nonlinearity of traveltime computation (Lomax et al. 2009) this problem can rarely be solved efficiently using the analytic approach (see Section 2.2.1).

Subsurface regions illuminated by the perforation shots may differ from the ones covered by the microseismic sources (Grechka 2010). What's more, for specific monitoring geometries incidence angles or azimuths covered by calibration shots can be too narrow for stable inversion of all desired model parameters (Grechka and Duchkov 2011), while in some cases no perforation or calibration shots data is available. An alternative approach may then be a simultaneous inversion of velocity model parameters and seismic events locations, called joint inversion (e.g. Grechka et al. 2011; Huang et al. 2019). The velocity model resulting in the least misfit of events traveltimes is assumed to be a correct representation of the subsurface. The events locations have to be re-evaluated with each modification to the velocity field, which increases the computational cost of joint inversions. In some cases, model space will be resolved better due to wider spatial distribution of seismic sources than in case of traditional inversion using calibration shots with known position (Li et al. 2013). On the other hand, lack of calibration shots

with known location rises the non-uniqueness of the resulting model parameters (Jansky et al. 2010), hence, the applicability of this approach may be case dependent.

As an inverse problem, velocity field estimation suffers from a number of difficulties, including non-uniqueness, instability, and convergence problem (Guo and Fagin 2002). In order to find the solution of this inverse problem (most often best fitting, i.e., approximate solution) forward modeling for various realizations of parameter space needs to be performed, and then the best fitting solution needs to be identified. The most straightforward method to sample the parameter space is to follow a grid-search scheme (Rodi and Toksoz 2000), i.e., the full grid-search. However, in geophysics, the parameter space may be highly dimensional, and grid dimensions can become too large to be tackled with just a grid search approach, especially when fine grid resolution is required. Therefore, directed and efficient sampling of the parameter space is necessary to drastically speed-up the calculations.

Consequently, global optimization methods have become a wide research topic, and numerous families of methods have been developed and already well established in order to optimize the inversion procedure. Those big families include modified grid-search approaches like directed grid-search or nested grid-search (Bentley 1975;Wuestefeld et al. 2018) implementations, Monte Carlo methods (Metropolis and Ulam 1949; Robert and Casella 2013), simulated annealing methods (Kirkpatrick et al. 1983; Černỳ 1985), genetic algorithms (Goldberg and Holland 1988; Goldberg 1989), stochastic optimization methods, like, e.g., neighborhood algorithm (Sambridge 1999a) or particle swarm optimization (Eberhart and Kennedy 1995). A thorough overview of global optimization methods is given by Sen and Stoffa (2013), while Wuestefeld et al. (2018) provides a benchmark of optimization function regarding the earthquake location problem.

Despite optimization algorithm implementation, the inverse problem can still be too costly to be solved with the desired resolution, which is necessary to obtain a global minimum of the misfit function. Then, effective utilization of a priori information may limit the parameter space and helps in constraining the inversion (Tarantola 1984; Ellis and Oldenburg 1994). The constraints put on the parameter ranges can be inferred from, e.g., borehole sonic logs or core analysis. Finally, the assessment of inverted model reliability should be performed by, e.g., inferring marginal distributions of the inverted parameters (Sambridge 1999b) in case of probabilistic methods or using ray coverage, checkerboards method, or resolution matrices in case of iterative inversion algorithms (Zelt 1999).

2.3 Shear-wave splitting

Shear-wave splitting (SWS) is the most direct indicator of the anisotropy. A shear-wave propagating through anisotropic medium splits into two orthogonally polarized shear waves traveling with different velocities (see Fig. 6). The polarity of the fast and slow *S*-wave modes and the delay time between them is determined by the anisotropic symmetry system and the direction of wave propagation relative to this symmetry system. The delay time is also determined by the magnitude of the anisotropy (Ando et al. 1980; Crampin et al. 1980; Silver and Chan 1991). The intuitive way to report the strength of anisotropy is a shear-wave velocity variation (in percent) expressed by an approximation (Wuestefeld et al. 2010) as:

$$A = \frac{V_S \cdot dt \cdot 100}{r} \tag{21}$$

where r is the source-receiver-distance, V_S is the mean *S*-wave velocity and dt is the delay in arrival time between fast and slow shear-waves.

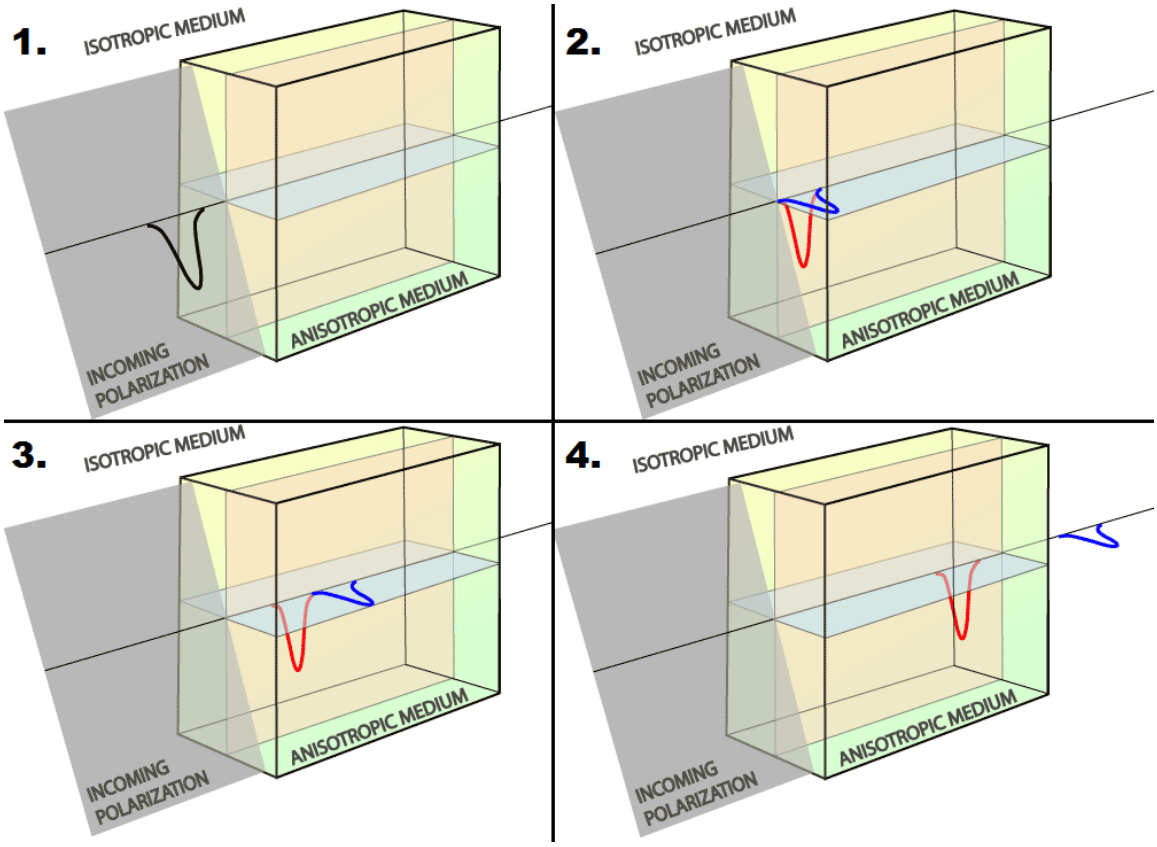

Fig. 6. A step-by-step visualization of shear-wave splitting in an anisotropic medium. A black wave indicates an initially polarized shear-wave in isotropic media. A blue wave indicates a vertically polarized fast shear-wave in anisotropic media. A red wave indicates a horizontally polarized slow shear-wave in anisotropic media. Source: http://garnero.asu.edu/research_images/anis/garnero_splitting.gif (accessed on 8 March 2019).

The SWS phenomenon has been exploited in various settings to retrieve important features of the subsurface at various scales. It is observed in laboratory tests on stressed or fractured rocks (Nur and Simmons 1969; Xu and King 1989; Ebrom et al. 1990; Tillotson et al. 2012), as well as in global seismology for long-period waves propagating through the crust and mantle (e.g. Vinnik et al. 1989; Silver and Chan 1991; Savage 1999). After being recognized as a useful phenomenon at exploration scale (Crampin et al. 1980; Lynn and Thomsen 1986; Willis et al. 1986), SWS has been used in fracture detection from surface seismic (Martin and Davis 1987; Mueller 1991; Liu and Martinez 2014), and multicomponent and walk-away VSP (Lynn et al. 1999; MacBeth 2002; Horne 2003; Gholami et al. 2016). SWS is also conventionally used in cross-dipole sonic logging for measuring in-situ azimuthal shear-wave anisotropy around the borehole (Mueller et al. 1994; Patterson and Tang 2001).

Two split shear modes are frequently observed during three-component downhole microseismic monitoring in hydrocarbon reservoirs (e.g. Crampin and Zatsepin 1995; Al-Harrasi et al. 2011). This length scale is usefully positioned between the lab-scale and larger-scale seismic observations (Verdon and Wüstefeld 2013). Unlike VSP and reflection seismic imaging, measuring SWS with downhole receivers benefits from the proximity of seismic sources (microearthquakes) and receiver arrays. Hence, it can be efficiently used to image anisotropy within the reservoir without the overburden influence that affects other methods (Wuestefeld et al. 2011).

Measurements of seismic anisotropy from microseismicity can be used in a number of ways, including: improving the accuracy of the velocity model (e.g. Grechka et al. 2011), enhancing the precision of event locations (Grechka and Yaskevich 2014), investigation of fracture alignment (e.g. Miyazawa et al. 2008; Verdon and Kendall 2011; Gajek et al. 2018c) and fracture connectivity (e.g. Baird et al. 2013; Verdon and Wüstefeld 2013); and determining changing stress conditions generated by subsurface operations (e.g. Verdon et al. 2011). Measurements of seismic anisotropy have been utilized in the geothermal industry (e.g. Rial et al. 2005) and for carbon capture and storage (e.g. Verdon et al. 2011), although its most common application with respect to microseismic data is during hydraulic fracturing of shale and tight gas reservoirs (e.g. Verdon and Wüstefeld 2013).

2.3.1 Measuring the shear-wave splitting

SWS parameters include the polarization (φ) of the fast shear-wave and the time delay (dt) between the two split shear modes. Those parameters need to be inverted on the basis of seismic records (Wolfe and Silver 1998; Teanby et al. 2004).

Obtaining theses parameters is not trivial, and various techniques were proposed, which can be divided into two groups. The first, called multi-event techniques, analyzes simultaneously a set of records coming from different azimuths. These methods operate on stacks of events, either weighted by azimuths (Kosarev et al. 1984; Vinnik et al. 1989), which makes an error assessment impossible, or binned in similar azimuthal bins (Chevrot 2000).

The second group, called single-event techniques, treats each trace individually from each event. These methods apply the so-called splitting correction by rotating phase and shifting the delay, which removes the effect of splitting from the seismic traces. Then, splitting parameters are found using a grid search, and the difference between various parameters is introduced by different implementations for the best correction. Bowman and Ando (1987) assumes that fast and slow shear modes are identical and use cross-correlation to identify their best match after correction. Silver and Chan (1991) seek for most linear particle motion utilizing the eigenvalue method. Wolfe and Silver (1998) looks for a parameter set resulting in minimum energy of the splitting correction residuals (transverse component).

All described methods require a shear-wave analysis window to be selected, which can be laborious and user-dependent. Nevertheless, those methods were successfully adopted for wide use in seismology to study regional scale tectonics (Vavryčuk 1993; Harris 1996; Gao et al. 1997; Vauchez et al. 1998; Crampin et al. 2003) and upper mantle anisotropy (Nicolas and Christensen 1987; Gao et al. 1994; Alsina and Snieder 1995; Gledhill and Gubbins 1996; Kendall and Silver 1996; Savage 1999; Niu and Perez 2004).

For single-event techniques, a measurement can be made for each source-receiver pair. This implies massive amount of data when seismometer or geophone arrays are used for such purposes like regional scale tectonic investigations (e.g., USArray (Hongsresawat et al. 2015) or AlpArray (Salimbeni et al. 2017)) or industrial monitoring applications including: oil and gas exploration (Martin and Davis 1987; Van Dok et al. 2003; Jones et al. 2014), geothermal water injections (Rial et al. 2005; Tang et al. 2005), hydraulic fracturing (Baird et al. 2013; Verdon and Wüstefeld 2013), CO_2 storage (Verdon 2011; Stork et al. 2015).

Hence, facing a need for robust SWS data processing, Teanby et al. (2004) proposed a fully automated method of SWS measurement, which is not dependent on the window selection. Instead, analysis is performed for a range of window lengths, and then results that are stable over various window lengths are selected using cluster analysis followed by quality factor estimation. Wüestefeld (2007) proposed to use all the single-event techniques described above, followed by QC based on characteristic differences between the two independent eigenvalue

and cross-correlation techniques (Wuestefeld et al. 2010). The last, most advanced strategy byWuestefeld et al. (2010) is utilized in this thesis.

2.3.2 Inversion of SWS measurements for rock-physics parameters

A single measurement of *dt* and φ along a single ray-path is not sufficient to constrain the overall anisotropic symmetry system. Instead, a population of SWS measurements along a range of ray-paths must be inverted to reveal the overall anisotropy. Typically, a rock-physics model, assuming a particular anisotropic symmetry system, must be created, which is then compared with the observations, with the best-fitting rock-physics model parameterization being taken as the result (e.g. Verdon and Kendall 2011; Baird et al. 2016).

In this thesis, the rock-physics parameters inversion is performed following the method developed by Verdon et al. (2009) and Verdon and Wüstefeld (2013). Their method utilizes an effective compliance approach developed by Schoenberg and Sayers (1995) to parametrize fractured VTI medium (hence, orthorhombic medium) by superposition of an anisotropic, though unfractured background rock compliance and compliance of penny-shaped fractures, assuming their idealized geometry (Hudson et al. 1996).

The effective compliance tensor (inverse of effective stiffness tensor, $S = C^{-1}$) of the fractured rock defined as the sum of the compliance tensor of the unfractured rock frame S^r, and the compliance tensor of single or multiple parallel fractures or aligned fractures sets ΔS, as:

$$S = S^r + \Delta S \tag{22}$$

The compliance of rock frame S^r can be isotropic or anisotropic, e.g., of VTI symmetry due to horizontal layering. Then, the VTI rock frame compliance $S^{r,\mathrm{VTI}}$ is given by the inverse of Eq. (6), which is:

$$S^{r,\mathrm{VTI}} = \begin{bmatrix} C_{11} & C_{11}-C_{66} & C_{13} & 0 & 0 & 0 \\ & (C_{11}) & (C_{13}) & 0 & 0 & 0 \\ & & C_{33} & 0 & 0 & 0 \\ & & & C_{44} & 0 & 0 \\ & & & & (C_{44}) & 0 \\ & & & & & C_{66} \end{bmatrix}^{-1} \tag{23}$$

and the fractures compliance $\boldsymbol{\Delta S}$ (Nichols et al. 1989; Schoenberg and Sayers 1995) is introduced by:

$$\Delta S = \begin{bmatrix} Z_N & 0 & 0 & 0 & 0 & 0 \\ & 0 & 0 & 0 & 0 & 0 \\ & & 0 & 0 & 0 & 0 \\ & & & 0 & 0 & 0 \\ & & & & Z_{Tv} & 0 \\ & & & & & Z_{Th} \end{bmatrix} \tag{24}$$

where Z_N is the normal compliance, and Z_{Tv} and Z_{Th} are the shear compliances in the vertical and horizontal planes, defined as:

$$Z_N = \frac{4}{3}\left(\frac{\xi}{C_{66}^r}\right)\left(\frac{C_{11}^r}{C_{11}^r - C_{66}^r}\right), \tag{25}$$

$$Z_{Th} = \frac{16}{3}\left(\frac{\xi}{C_{66}^r}\right)\left(\frac{C_{11}^r}{3C_{11}^r - 2C_{66}^r}\right), \tag{26}$$

$$Z_{Tv} = \frac{16}{3}\left(\frac{\xi}{C_{44}^r}\right)\left(\frac{C_{33}^r}{3C_{33}^r - 2C_{44}^r}\right), \tag{27}$$

where ξ is the non-dimensional fracture density. Z_{Tv} and Z_{Th} will only differ when significant VTI anisotropy is present (Backus 1962; Hudson 1981; Verdon et al. 2009). The fracture compliance is frequency-dependent due to the model assumptions. However, authors assume fracture scale to be much smaller than the wavelength (low-frequency assumption) to reduce free parameters in the inversion, and hence, focus on ξ due to neglecting other parameters like fracture aperture or rock permeability (Verdon et al. 2009). Therefore, fractures become equivalent to the Hudson (1981) model with vertically aligned, unfilled, penny-shaped fractures.

Those assumptions are then implemented into forward modeling for the inversion needs. The background *P*- and *S*-wave velocities, V_P0, V_S0, and density, are held constant through the model space. Inversion itself is resolved by iterating over a parameter space including fracture density ξ, fracture azimuths α, δ, and γ. The effective compliance tensor providing velocities and polarizations of *S*-waves for any direction is computed. Computation is done by solving a Christoffel equation (Crampin 1984; Carcione 2007), hence, limitations that may be caused by weak anisotropy assumptions are omitted. The inversion is guided by Neighborhood Algorithm sampler (Sambridge 1999a). The results are then evaluated in terms of posterior probability analysis (Sambridge 1999b). The detailed workflow and sensitivity tests are described in detail by Verdon et al. (2009); Verdon and Wüstefeld (2013).

3. DEVELOPED METHODOLOGY AND SYNTHETIC EXAMPLES

This chapter describes new methods created or modified by me, which are used in this research.

First, a probabilistic event location algorithm for downhole monitoring is introduced, featuring a comprehensive error assessment capabilities thanks to the Bayesian inference being employed (Tarantola 1984). The problem of the event location (introduced in Chapter 2) is split into two parts. The first part involves computing the probability density map of the event location in a vertical (offset-depth) plane. The other part involves the back-azimuth estimating together with its uncertainty. Then, a vertical slice of location probability density is combined with information about azimuthal uncertainty of back-azimuth estimation in order to provide a three-dimensional volume of location probability density.

Next, I introduce a technique of traveltime anisotropic velocity model inversion using a single vertical array of receivers and perforation shots data. The anisotropic eikonal solver (Riedel 2015) is being used for forward modeling, while Neighborhood Algorithm (Sambridge 1999a) is applied to optimize inversion procedure. The inversion utilizes *P*-, *SH*-, and *SV*-waves[1] traveltimes of perforation shots, whose locations are known.

In this chapter, I argue that it is always beneficial to account for anisotropy by using anisotropic velocity model instead of a number of isotropic models, which is a common practice in the industry. In order to support this statement, which is one the hypothesis addressed in this dissertation, the introduced methodology is supplemented by a set of synthetic tests showcasing microseismic events' mislocations being introduced whenever anisotropic media is described by isotropic models only. Synthetic modeling is performed for two downhole monitoring geometry scenarios from real-case applications of microseismic monitoring of hydraulic fracturing, providing a quantitative interpretation of location errors expected to be present when anisotropy is being neglected during the inversion of the velocity model. Also, the limitations of the proposed methodology in terms of minimal resolvable layer thickness are examined.

The application of this methodology to real data follows in the next chapter.

Finally, I present a feasibility study of quasi-real-time, on-site anisotropic velocity model inversion during an ongoing hydraulic fracturing job.

[1]For the brevity, the qualifiers in "quasi *P*-wave" and "quasi *S*-waves" are omitted.

3.1 Probabilistic event location

A number of conclusions are drawn from studying locations of microseismic events, i.e., inferring fracture geometry and size (Warpinski et al. 1998), taking decisions on treatment parameters in consecutive stages, or assessing the stimulated reservoir volume (SRV) (Mayerhofer et al. 2010). Thus, it is crucial, if locations of the microseismic events are reliable (Maxwell 2009). Therefore, so much effort is devoted to increase the location precision and reduce its uncertainty (e.g. Grechka et al. 2015; Yaskevich et al. 2016). Understanding the uncertainty is particularly

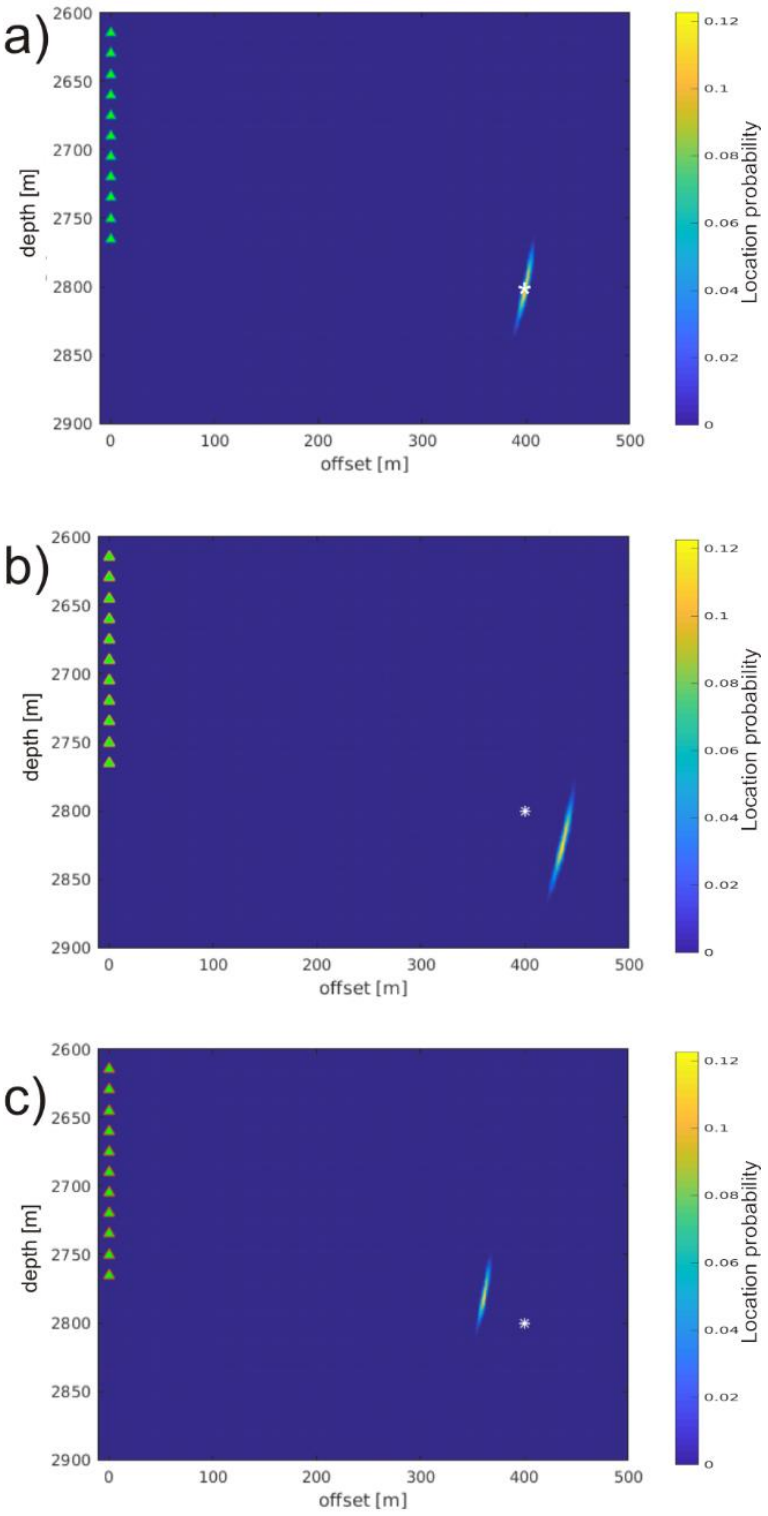

Fig. 7. Maps of location probability of a synthetic event assuming some picking uncertainty. The shape of the uncertainty distribution is dependent on event location – white star, and receivers position – green triangles. Panel a) shows the location probability when an exact velocity model is used. Panels b) and c) show the location probability when velocities are too high by 10%, and too low by 10%, respectively.

important for downhole measurements in a single borehole because this geometry results in the highly asymmetric distribution of the events' locations uncertainty (Eisner et al. 2009) and no other method gives a sense of its real shape. An example of the asymmetric distribution is given in Fig. 7a. Importantly, the probabilistic approach can integrate uncertainties originating from various inputs, e.g., first break picking errors, receivers location uncertainty, or inaccuracy of the velocity model. The approach I have implemented in this thesis accounts for uncertainties introduced by first break picking, and by the inaccuracy of picked-modeled travel times fit, only. The location uncertainty may also be affected by the inaccuracy of the velocity model - the effects of using the wrong velocity model are shown in Fig. 7b,c. Then, true location can be missed even though the cloud of probability is focused and well resolved.

Traditionally, in the so-called "dots-in-the-box" visualization, each event is presented as a dot (Fig. 8b), whose size can be scaled by different parameters (Fig. 8d,f). Its location uncertainty, if given, is often described by discrete values of horizontal and vertical uncertainties that do not reflect actual, two-dimensional distribution of uncertainty. Those ranges can be plotted together with the dots; however, they dramatically lower the legibility of the figure. Another drawback is dots' overlapping, especially when scaled, which can be somehow solved by constructing event density maps.

The probabilistic representation has several advantages over the standard method. The most important one is the sense of uncertainty, particularly in this case of acquisition geometry. The probability density function (PDF) of the single event is tilted relative to the center of the array (Fig. 7). This shape cannot be correctly explained in terms of horizontal and vertical errors. What's more, dots are more prone to misinterpretation due to the poorly resolved locations – the events with high uncertainty look the same as those with low uncertainty. Contrary, probabilistic representation spreads the PDF of poorly resolved events more than in case of the well-resolved ones.

PDFs for multiple events can be easily summed to obtain cumulative event density maps. The cumulative PDF of all events shows clearly the main epicentral region indicating the most fractured area – this information is hard to infer from the overlapping dots.

Maps of location probability may be interpreted directly, but also weighted by physical parameters like individual events' magnitudes, in order to highlight the most promising fragments of fractured reservoir (Gajek et al. 2016). The location PDF weighted by local magnitude M_0 or seismic moment magnitude M_W gives a sense of the size of the event. M_0 is directly related to the energy; therefore, it is particularly good as it has more physical meaning than the magnitude. Its cumulative representation shows the regions, where most of the seismic energy was radiated from, which are the most fractured regions. Figure 8 presents a comparison of traditional "dots-in-the-box" visualization and probabilistic approach.

For the probabilistic events location I am using a Bayesian approach (Tarantola 1984), which gives an individual probability distribution for each event. The idea of traveltime-based location procedure is to minimize a difference between theoretical (t^i_{cal}) and observed (t^i_{obs}) onsets of waves for each receiver i in a given velocity model m and for source time t_0. The notion of probability is introduced to the formula for location probability $\rho_{\mathrm{m}}(X, Z, t_0)$ by a Gaussian likelihood function (the argument of exponent) and picking uncertainty for each receiver σ_i. For downhole, single borehole setting, only the depth (here noted as Z) and offset (here noted as X) of an event can be obtained using the traveltimes. In order to determine the direction towards the event, a back-azimuth procedure (addressed later) has to be used.

For isotropic case, with only *P*- and *S*-waves onsets ($t^{P,i}_{\mathrm{obs}}$, $t^{S,i}_{\mathrm{obs}}$), the formula for location probability $\rho_m(X, Z, t_0)$ is given by:

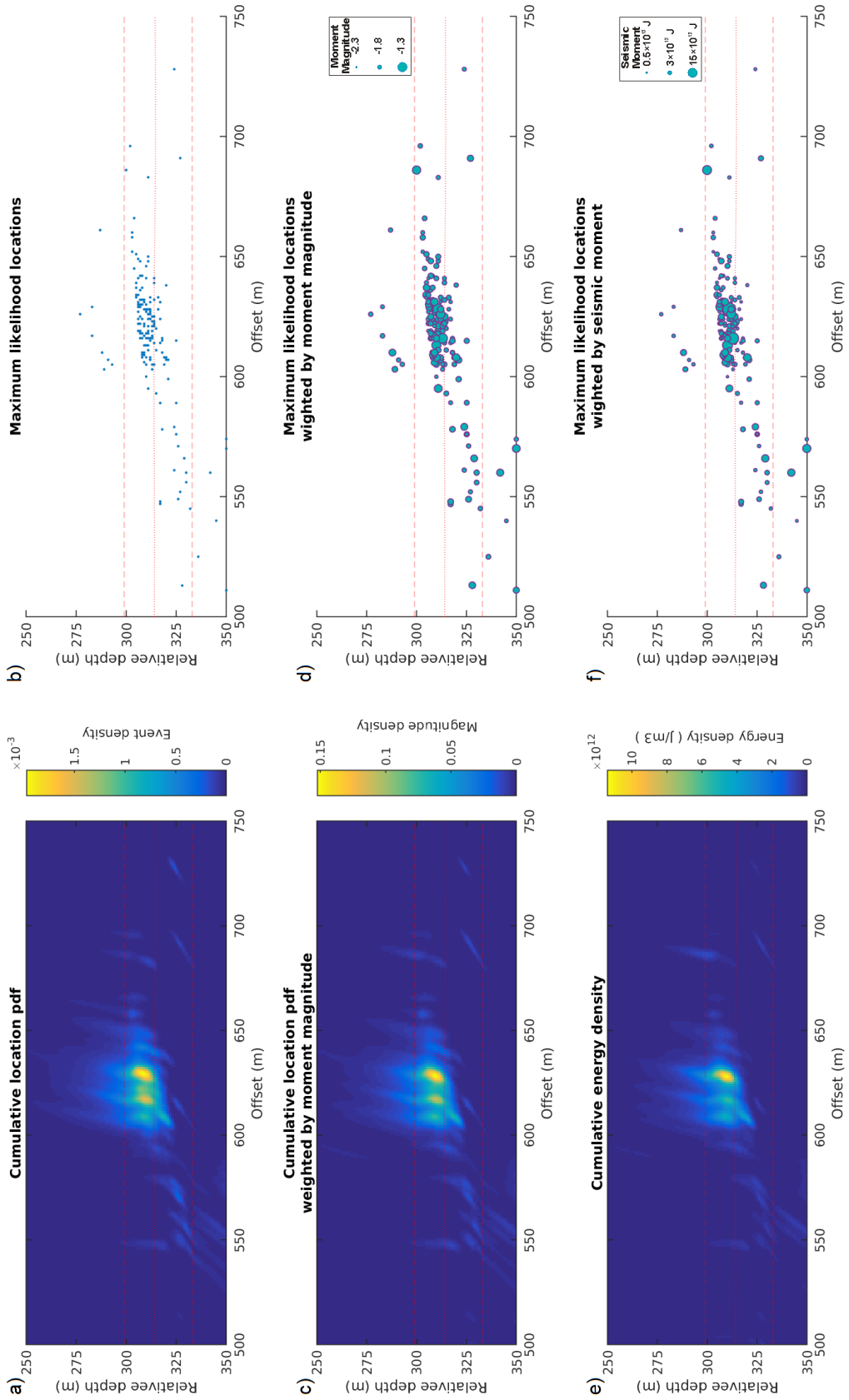

Fig. 8. Locations of 183 microseismic events from Lubocino hydraulic fracturing dataset: a) cumulative location PDF, b) maximum likelihood locations – a "dots-in-the-box" representation, c) cumulative location PDF weighted by moment magnitude, d) maximum likelihood locations scaled by moment magnitude, e) cumulative energy density, f) maximum likelihood locations scaled by seismic moment. Borehole trajectory – red dotted line. Top and bottom of the target layer – red dashed lines. Source: Gajek et al. (2016).

$$\rho_m(X,Z,t_0) = k \cdot \exp\left(-\frac{\sum_{i=1}^{n}\left(\left(t_{\text{obs}}^{P,i} - t_{\text{cal}}^{P,i}(X,Z)+t_0\right)^2 + \left(t_{\text{obs}}^{S,i} - t_{\text{cal}}^{S,i}(X,Z)+t_0\right)^2\right)}{2\sigma_i^2}\right) \quad (28)$$

where n denotes the total number of receivers, X the offset, Z the depth, and k the scaling constant.

In case of an anisotropic medium, when the *S*-wave is split into fast and slow shear wave modes (here *SH* and *SV*, respectively), the formula for location probability has to be expanded to:

$$\rho_m(X,Z,t_0) = k \cdot \exp\left(-\frac{\sum_{i=1}^{n}\left(\left(t_{\text{obs}}^{P,i} - t_{\text{cal}}^{P,i}(X,Z)+t_0\right)^2 + \left(t_{\text{obs}}^{SH,i} - t_{\text{cal}}^{SH,i}(X,Z)+t_0\right)^2 + \left(t_{\text{obs}}^{SV,i} - t_{\text{cal}}^{SV,i}(X,Z)+t_0\right)^2\right)}{2\sigma_i^2}\right) \quad (29)$$

In seismological practice inverting for an earthquake location involves also inverting for its origin time t_0. Usually, a broad range of possible origin times has to be checked. Here, due to both, a lack of interest in accurate origin times and a need to lower computational cost of calculations, the range of time term t_0 has been greatly reduced; however, it is still present in the formula to enhance inversion accuracy.

In order to omit inverting for the source time t_0, all the observed and calculated traveltimes are reduced by $\min\left(t_{\text{obs}}^{P}\right)$ and $\min\left(t_{\text{cal}}^{P}\right)$, respectively, so the time of first of the arrivals is reduced to 0. Hence, all those terms become directly comparable without accounting for the source time. Nevertheless, t_0 term is still introduced in order to handle possible outliers, as a linearly spaced time interval:

$$t_0 \in \langle 0,2\left|t_{\text{obs}}^{P,1} - t_{\text{obs}}^{P,2}\right|\rangle\,; \quad (30)$$

Figure 9 presents a synthetic example of t_0 fitting when the first pick is an outlier. In the example, theoretical traveltimes were generated by adding some Gaussian noise (mean 0, vari-

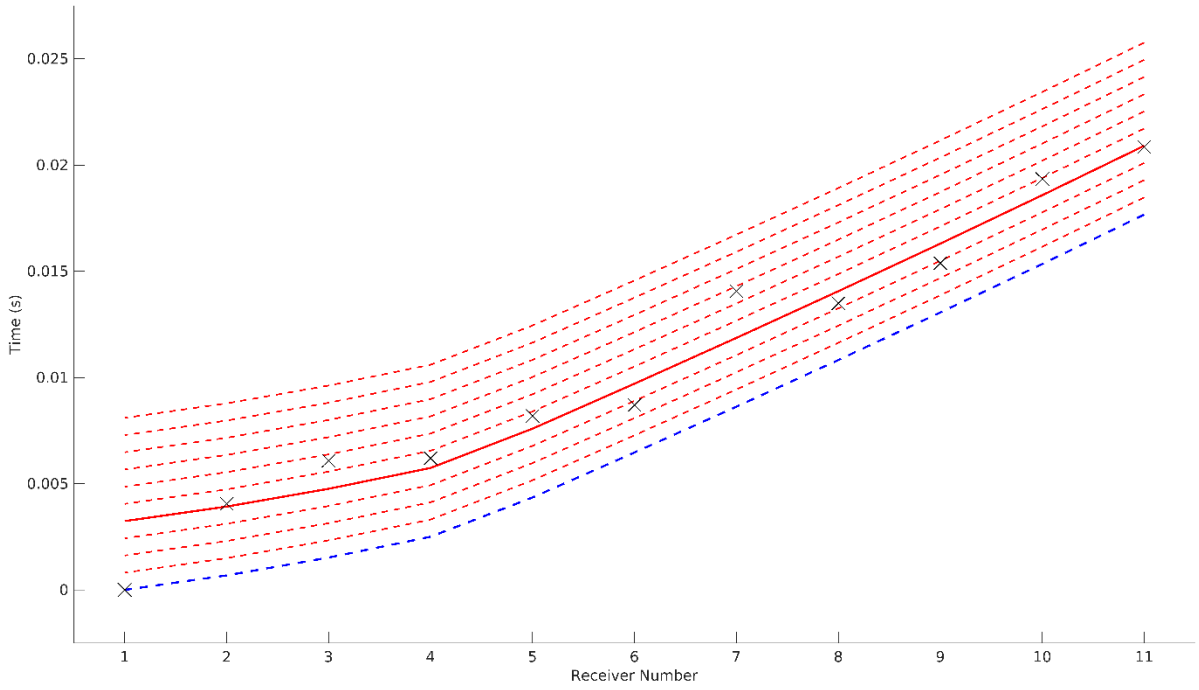

Fig. 9. An example of t_0 fitting. Black crosses represent observed traveltimes, lines represent all possible calculated traveltimes for a true model with t_0 added. Blue dashed line shows scenario for t_0 = 0 s (i.e. without t_0 term), solid red line shows least RMS fitting (t_0 = 0.32 s).

ation 0.00375 s) to the modeled traveltimes. Then both calculated and theoretical traveltimes were reduced by $\min(t^P_{\mathrm{obs}})$ and $\min(t^P_{\mathrm{cal}})$, respectively. This approach allows finding a good fit despite the outliers, using a limited range of t_0 values, comparing to inverting the actual source time. Hence, the range of t_0 values can be densely probed.

3.1.1 Station-event back-azimuth estimation

The back-azimuth procedure is used in seismology to estimate a direction towards incoming energy based on the analysis of particle motion (Flinn 1965). As the name suggests, back-azimuth refers to the estimation of the azimuth only; however, it is easily expandable to be applied to three dimensions (e.g. Vidale 1986; Jurkevics 1988; Walck and Chael 1991) in order to get both azimuth and incidence angle. When numerous receivers are available (in case of, e.g., few observation boreholes or a significant number of surface geophones) both azimuth and incidence angle can be inferred from traveltimes only (Maxwell 2014; Grechka and Heigl 2017).

The back-azimuth estimation becomes particularly important when only a single 3C station or a single vertical string of 3C receivers is available, which is the case study included in this thesis. Then, the only possibility to estimate the horizontal distribution of seismic events is to analyze particle motion directivity. Borehole techniques for microseismic monitoring benefit a lot from a methodology developed for single station event location problem in regional seismology (Magotra et al. 1987; Roberts et al. 1989; Lay and Wallace 1995).

The back-azimuth can be estimated using few different methods based on arrival hodogram analysis, including covariance matrix analysis (Flinn 1965), Principal Component Analysis (Rao 1964; Hagen 1982), maximum amplitude or linear fit (Maxwell 2014).

Despite the chosen method of back-azimuth estimation the result will be affected by uncertainty imposed by noise contributing to the observed seismograms, particularly amplified during the hydraulic treatment, which is a common issue in microseismic monitoring (Eisner et al. 2008; Caffagni et al. 2016; Trojanowski et al. 2016), anisotropy (e.g. Crampin et al. 1982) and uncertainty of receiver orientation. Importantly, angular uncertainty results in increased azimuthal location error at increasing source-receiver distances (Maxwell 2014).

Accuracy of back-azimuth estimation can be enhanced by e.g., signal conditioning or stacking. In the case of the 3C geophones string in a vertical borehole, horizontal components can be stacked in order to increase the efficiency of the back-azimuth estimation by decreasing random interferences and increasing the S/N, providing that orientation correction has been already applied (Klemperer 1987; Zaręba and Danek 2019). Nevertheless, errors in back-azimuth estimation should be statistically analyzed to provide an assessment of azimuth uncertainty (Christoffersson et al. 1988).

Therefore, I use least-squares linear regression with uncertainties in both axes for the purpose of horizontal event location performed in this thesis. A mean value of filtered or detrended seismic trace is expected to be 0. Hence, applying linear regression ($y = ax + b$) with intercept parameter $b = 0$ to the hodogram of horizontal components containing *P*-wave arrival will give slope parameter *a*. Tangent of parameter a will be a counter clock-wise angle measured from the positive X-axis towards the positive Y-axis, from which azimuth can be easily calculated.

Quality of linear fit is usually assessed with a coefficient of determination R^2, which is the proportion of the variance in the dependent variable that is predictable from the independent variable (Rao et al. 1973; Glantz and Slinker 1990). R^2 provides insight into the quality of a particular fit, but do not inform about the uncertainty of the slope parameter estimation. Since both horizontal components contain background noise introducing uncertainty to the slope parameter a, a regression cannot be implemented in a classical way, which imposes some error on the ordinate axis only. Instead, an error should be introduced to both axes. Then, e.g., least-

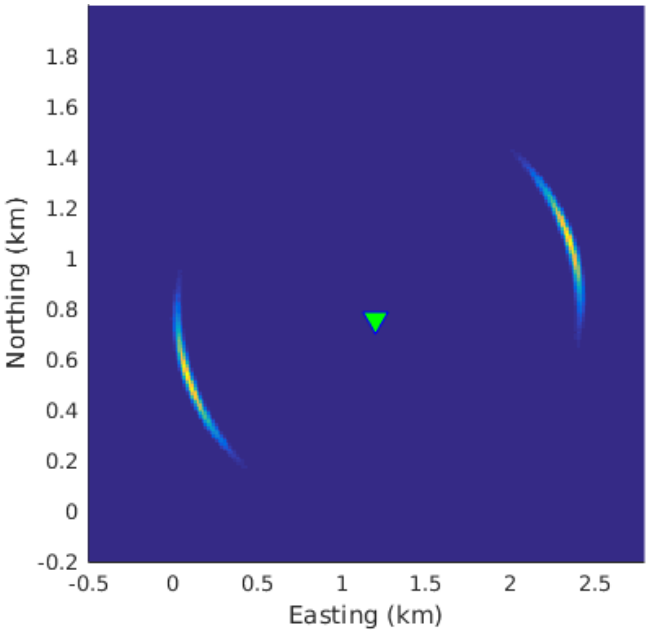

Fig. 10. Synthetic result of single station back-azimuth estimation. Map shows a horizontal surface PDF distribution slice of an event location with hot color indicating high probability density, and green triangle indicating position of a seismic station. The distribution of PDF has two maxima due to the 180° direction ambiguity.

squares regression with uncertainty in both axes proposed by Tarantola (2005) can be applied in order to obtain a PDF of slope parameter a distribution.

I estimate the back-azimuth of microseismic events using sections of 3C seismic traces containing picked *P*-wave arrivals. One hundred and one samples (0.0375 s) long sections with the middle sample being the *P*-wave pick are stacked (receivers were prior corrected for orientation in the borehole). First 25 samples are used to obtain the RMS of background noise, which I assume to be Gaussian and directionally independent. Next, least-squares regression with uncertainty in both axes is performed, with noise RMS taken as an error for both of the axes, and PDF of slope parameter a is obtained. Then, the PDF of a is fitted with a normal distribution curve in order to obtain the median value and standard deviation. Finally, the median value after correction for the geographical coordinate system is taken as an azimuth towards the event, while standard deviation is considered as an error of azimuth estimation. After obtaining an event's offset using a traveltime based location approach, the error in the offset-depth plane is distributed radially according to the Gaussian back-azimuth distribution (Fig. 10). Such an approach provides individual back-azimuth for each event and associated uncertainty estimation, dependent on the linearity of first arrivals particle motion, signal quality, and present background noise conditions.

Another problem of back-azimuth estimation is the direction ambiguity due to 180° arctangent periodicity. This ambiguity can be resolved when the mechanism of a seismic source is known, which is the case for check shots, perforation shots, or any shots in controlled source seismic methods. However, for tectonic earthquakes or induced (and triggered) seismicity, the source mechanism remains unknown imposing ambiguity on the direction (Fig. 10). Therefore, the back-azimuth estimation needs to be supplemented with some a priori constraints. In hydraulic fracturing operations, the direction towards the area where microseismic events are expected is known so the back-azimuth ambiguity can be easily resolved.

3.2 VTI velocity model inversion scheme

In each microseismic monitoring experiment being performed a knowledge about the velocity model is indispensable. It can be either obtained through the inversion procedure or taken from a nearby setting. Nevertheless, if taken from a nearby survey, it does not guarantee the same

accuracy and should be calibrated. Different strategies for the inversion were already introduced in Chapter 2. Here, I present a scheme and synthetic tests of my method's performance.

Developing a new inversion tool on my own was stimulated by the lack of availability of specific software. The requirements for the software were to:

1) account for anisotropy by producing traveltimes of P-, SH-, and SV-waves,
2) account for refracted waves,
3) be applicable to use with downhole settings,
4) be computationally efficient and applicable as inversion forward solver,
5) be available to purchase or free of charge.

Some oil and gas companies developed their in-house software capable of dealing with the above requirements; however, they are not willing to share it publicly. There are some scientific software packages available, fulfilling some, but not all of the requirements. For example, the Anivec package designed for reflection seismic (Mallick and Frazer 1988) does not support downhole geometries, ANRAY (Pšenčík 1998) is a good raytracing modeling tool, however, does not account for head waves, what was necessary in the studied case. Norsar 3D was not able to simulate expected seismic phases for all traces in desired geometry due to challenging source effects. What's more, possibilities to use some particular tools were not available at the time when this work has started. Hence, I decided to develop the inversion tool on my own, taking advantage of some already existing software packages, that could be used to some extent.

The procedure of VTI velocity model building through traveltime inversion was designed in order to obtain a velocity model providing accurate locations of perforation shots, resulting later in reliable locations of microseismic events. Traveltimes for the inversion and location procedures were computed using an eikonal traveltime solver by Riedel (2015), which accounts for all three types of waves (*P*, *SH*, and *SV*) propagating in the TI medium. The *SH* phase is not always visible in the records of perforation shots due to the explosive source mechanism. Then, an extra effort is necessary to obtain the γ parameter. Such a case is discussed in the field data application in Chapter 4. Nevertheless, it is incorporated by default in the inversion procedure since other authors report a distinctive *SH* phase in the perforation shot records (Mizuno et al. 2010; Grechka and Duchkov 2011; Tan et al. 2014). The standard version of the eikonal traveltime solve was created for the purpose of surface seismic applications and was supporting only *P*-wave traveltime modeling. Due to collaboration with the author it was adopted to account also for both shear-waves for this particular reason. Then, a full procedure of inversion including, e.g., establishing communication between different programs and MATLAB in Unix environment, traveltimes import, error assessment, code parallelization, and optimization, was developed and encoded in MATLAB by me. The inversion procedure was tested on synthetic datasets and finally applied to real data (Chapter 4).

The objective function ζ is based on the L2 norm differences between the observed (t^{P}_{obs}, t^{SH}_{obs}, t^{SV}_{obs}) and modeled traveltimes of *P*-, *SH*-, and *SV*-waves ($t^{P,i}_{\mathrm{cal}}$, $t^{SH,i}_{\mathrm{cal}}$, $t^{SV,i}_{\mathrm{cal}}$) including arbitrary time term t_0, analogically to the event location procedure. Calculations are performed for each receiver *i* and each available calibration shot *j*:

$$\zeta = \sum_{j=1}^{p} \sqrt{\frac{\sum_{i=1}^{n}\left(\left(t^{P,i,j}_{\mathrm{obs}} - t^{P,i,j}_{\mathrm{cal}} + t_0\right)^2 + \left(t^{SH,i,j}_{\mathrm{obs}} - t^{SH,i,j}_{\mathrm{cal}} + t_0\right)^2 + \left(t^{SV,i,j}_{\mathrm{obs}} - t^{SV,i,j}_{\mathrm{cal}} + t_0\right)^2\right)}{n}} \tag{31}$$

where *p* denotes the total number of calibration shots and *n* denotes the total number of receivers.

Using this approach layer-dependent *P*- and *S*-wave velocities and global Thomsen's anisotropic parameters for the whole model space are inverted. It is flexible to be applied to various settings, in terms of sources and receivers numbers and positions, isotropic, VTI media or

mixed. Inversion can be run using all *P*-, *SH*-, and *SV*-waves, and any combinations of them as well (providing then a limited number of output parameters).

During the synthetic tests, the inversion is run using a MATLAB encoding of Neighborhood Search Algorithm by Sambridge (1999a), coded by James P. Verdon, freely available at his personal web page: https://www1.gly.bris.ac.uk/~gljpv/software.html (last access on 29 October 2018).

3.2.1 Synthetic tests

Anisotropic velocity models are used to generate input data for all of the tests. Inversions of both isotropic and anisotropic velocity models are then performed using traveltimes generated in anisotropic models (with some random noise imposed) in order to:

1) present consequences of ignoring the anisotropy during velocity model building,
2) illustrate how the anisotropy influences the procedure of velocity model building, and consequently the accuracy of resulting microseismic events locations, by providing a quantitative measure of location errors,
3) validate a newly developed method of VTI velocity model inversion, examine limits of its capabilities, and present its advantages over the isotropic approach.

The geometry of synthetic tests showcases a common setting during hydraulic fracturing operations, where the observation well is close to the heel of the injection well, while the fracturing stages proceed from the toe to the heel. The velocity model is calibrated using the perforation shots. Therefore, the data for model calibration is being gathered from the first till the last stage execution. Since more shots are becoming available during the treatment, the velocity model has to be either updated every stage or substituted with a set of isotropic models (single-stage approach), used for a single stage only. In the tests, two different geometries – with proximate and distant calibration shots are considered, displaying geometries that have been used in hydraulic fracturing jobs done for PGNiG at Lubocino (dataset presented in next two chapters of this thesis) and Wysin sites.

Two different approaches to isotropic inversion were tested to analyze how the location error is distributed when moving away from calibration shots location, i.e., to what extent isotropic models can reliably describe anisotropic medium in the vicinity of perforation shots used for the inversion. Then, the anisotropic inversion was run for the two different model geometries to validate how the accounting for anisotropy improves the accuracy of the inverted velocity model. Also, the topic of inversion limits is addressed.

In total, six modeling examples are presented in this thesis, chosen in the way to highlight differences between various approaches to the velocity model inversion problem for two real-case geometries. In each of the tests, different velocity model is being inverted in order to address a particular aim. Each test, together with the interpretation of its results, is described in detail in the following paragraphs. The tests with their brief descriptions are listed below:

I. Proximate single-stage isotropic
   The individual isotropic velocity model is inverted per stage (3 perforation shots each). Shot offsets range from 245 to 610 m from the monitoring borehole (identical to Lubocino experiment setting).
   The aim is to assess the accuracy of this approximate solution and examine its reliable spatial extent.

II. Proximate isotropic
   The single isotropic velocity model is inverted for all the stages, updated every stage by 3 additional perforation shots. Shot offsets range from 245 to 610 m from the monitoring borehole (identical to Lubocino experiment setting).

The aim is to verify how accurately the anisotropic medium can be described by a single isotropic model and confront the findings with the results of test I.

III. Proximate anisotropic
Single VTI anisotropic velocity model is inverted for all the stages, updated every stage by 3 perforation shots, for Lubocino geometry. Shot offsets range from 245 to 610 m from the monitoring borehole.
The aim is to validate the correctness of the developed inversion procedure.

IV. Distant anisotropic
Single VTI anisotropic velocity model is inverted for all the stages, updated every stage by 3 perforation shots, for Wysin geometry. Shot offsets range from 1245 to 1610 m from monitoring borehole.
The aim is to validate the correctness of developed inversion procedure in an alternative setting.

V. Thinning layer accuracy test
Single VTI anisotropic velocity models are inverted using all data from all 5 stages (no updates), for incrementally decreasing thickness of the middle, anisotropic layer, while other layers are being isotropic. Shot offsets range from 245 to 610 m from the monitoring borehole (identical to Lubocino experiment setting).
The aim is to assess the limits of inversion reliability when considering a thin, anisotropic layer.

VI. Effective anisotropic
Two VTI anisotropic velocity models are inverted using all data from all 5 stages (no updates), for two different strengths of anisotropy in individual layers. Shot offsets range from 245 to 610 m from the monitoring borehole (identical to Lubocino experiment setting).
The aim is to verify how accurately the differently anisotropic layers can be described by the effectively anisotropic medium with various velocities but global Thomsen's parameters for the whole model space.

In the synthetic tests, the existence of weak elastic anisotropy was assumed (Thomsen 1986) with Thomsen's parameters: $\varepsilon = 0.1$, $\gamma = 0.15$, $\delta = 0.05$ (comparison between exact and simplified velocities for weakly anisotropic assumption for given parameters was provided in Fig. 5). Perforation shot traveltimes for *P*-, *SH*-, and *SV*-waves were generated using an eikonal solver accounting for anisotropy (Riedel 2015). Then a Gaussian noise with mean 0 and standard deviation 0.000375 s (one sample of data from Lubocino) has been imposed on the picks. A simple model with three flat layers, absorbing boundary conditions and parameters listed in Table 2 is assumed. The model layout and its parameters correspond to the geological setting in Lubocino, in terms of the strength of anisotropy and the presence of a low-velocity shale

Table 2

Parameters of synthetic model used in the modeling

Layer	Top depth [m]	Thickness [m]	V_P0 [m/s]	V_S0 [m/s]	ε	δ	γ
1	0	100	4200	2500	0.10	0.05	0.15
2	100	100	4800	3000			
3	200	120	3700	2000			

layer capped by higher velocity formations. A constant layer thickness of 100 m of capping formations was assumed (except test V). Such a model with no complex geology aims at highlighting the influence of intrinsic anisotropy only, without any structure-induced anisotropy. There are five groups of perforation shots, i.e., five treatment stages, three shots per stage, resulting in a total number of 15 shots.

Inverting for isotropic models is much faster, since for n layer model with fixed layer interfaces only $2n$ parameters need to be found. In the case of the VTI anisotropic model with global anisotropy parameters, one needs to invert for $2n + 3$, having an additional ε, γ, and δ. For isotropic velocity model inversion only *P*- and *SH*-wave picks were used, assuming *SH*-wave to be isotropic *S*-wave.

Initial parameters limits for the isotropic inversions were as follows:

- $V_P \in \langle 3300, 5300 \rangle$
- $V_S \in \langle 1500, 3500 \rangle$

Initial parameters limits for the anisotropic inversions were:

- V_P0 = true $V_P0 \pm 500$ m/s
- V_S0 = true $V_S0 \pm 500$ m/s
- ε, γ, δ = true ε, γ, $\delta \pm 0.03$

Parameters ranges were restricted in order to speed up the calculations, reflecting a priori constraints made from the sonic log interpretation. The grid resolution in all of the examples was 5 m.

The methodology for each of the inversions and the assessment of its results follow the steps listed below:

1) Prepare an events grid by generating traveltimes for all possible events locations using the synthetic VTI anisotropic model described in Table 2 (modified for tests V and VI).
2) Extract traveltimes of events at the calibration shots locations (perforation shots), add random noise to those traveltimes (mean 0 and standard deviation 0.000375 s).
3) Invert isotropic or anisotropic model for all perforation shots or shots from selected stages. In the case of scenario V, consider the different thickness of the middle layer.
4) Calculate locations of each event from the events grid (obtained in step 1) using the inverted velocity model and calculate the mislocation as a Cartesian distance between obtained and true locations.
5) Compute the Correctness Factor CF0 for each of the inversions to measure model correctness in the vicinity of perforation shots. CF0 is defined as a ratio of events located with 0-error to all events number in the defined range. The range is corresponding to the area where microseismic events are expected and is marked in the following figures (±50 m from extreme coordinates for all available data). In some cases also CF1 is calculated, which is equal to CF0 with 1 grid node error tolerance (±5 m).

I. Proximate single-stage isotropic

Inversions for isotropic, single stage models resulted in good calibration shots locations, with 11 out of 15 shots locations being just exact (Fig. 11). Location errors of 4 mislocated shots were not greater than diagonal grid node spacing (7 m). However, when moving away from the calibration shots locations, the error grows considerably (Fig. 12). Least values at the mislocation maps are kept on the axis pointing from the calibration shots location towards the receiver array, which can be expected due to the presence of anisotropy.

From inspection of Fig. 13 it can be seen, that inverted locations are shifted according to a consistent pattern. Events are circularly shifted around calibration shots following an anticlockwise motion, i.e., events located more distant or above the calibration shots are moved up

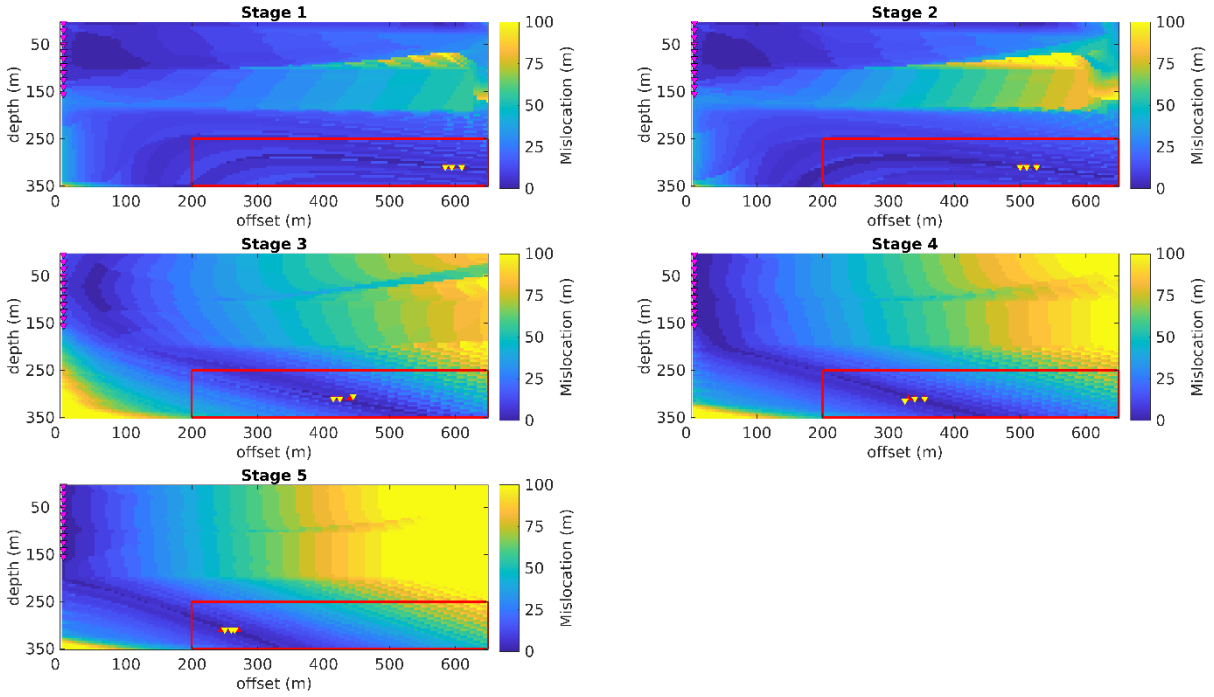

Fig. 11. Complete map of events mislocation for a set of 5 isotropic models (each per stage) for whole model space (test I). Mislocation is calculated as a Cartesian distance between expected and obtained location using actual velocity model for each grid point. Expected positions of calibration shots are marked with red triangles, calibration shots locations obtained using inverted velocity model are marked with yellow upside down triangles. The red rectangle marks the area taken into account for CF0 calculation.

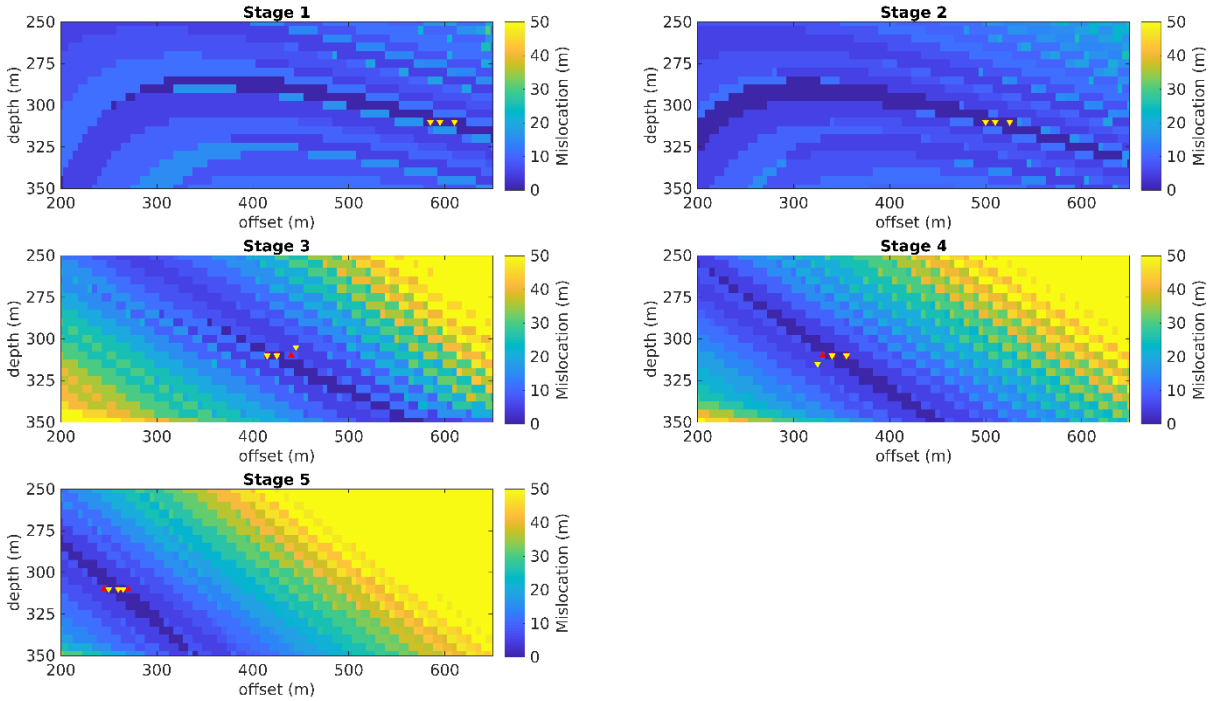

Fig. 12. Map of events mislocation for a set of 5 isotropic models (each per stage) enlarged for selected area (zoomed into red rectangle in Fig. 11). Mislocation is calculated as a Cartesian distance between expected and obtained location using actual velocity model for each event. Expected positions of calibration shots are marked with red triangles, calibration shots locations obtained using inverted velocity model are marked with yellow upside down triangles. CF0 is calculated for whole visible area.

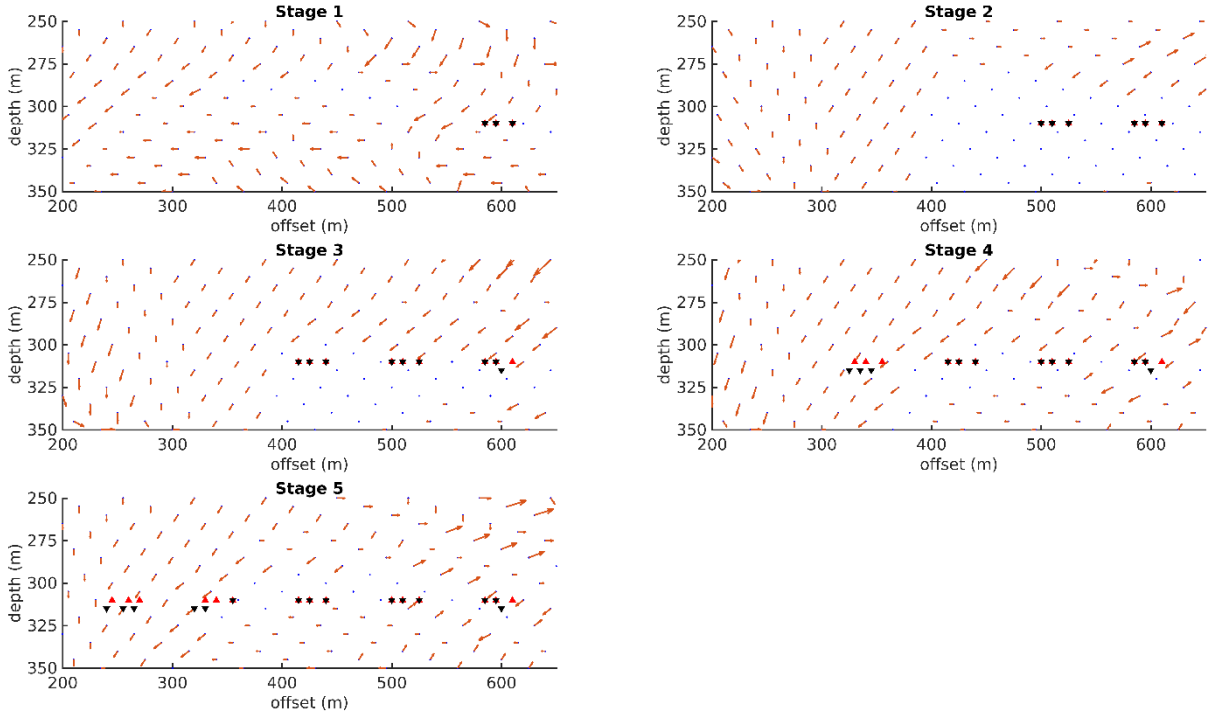

Fig. 13. Map of events mislocation directions for a set of 5 isotropic models (each per stage) enlarged for selected area (derived from Fig. 11). Vectors point from expected towards the obtained location, but their lengths have been downscaled for clarity; therefore, for mislocation magnitudes the reader is referred back to Fig. 12. Expected positions of calibration shots are marked with red triangles, calibration shots locations obtained using inverted velocity model are marked with black upside down triangles.

and towards the monitoring array, while locations of closer and lower-lying events are decreased and moved away from the monitoring array.

The CF0 for all of the stages remains lower than 0.1, meaning that less than 10% of the events can be located correctly (for details see Table 3).

II. Proximate isotropic

In this stage-by-stage updated test, all currently available information was used, i.e., calibration shots from subsequent stages were being added with every stage.

Inversions for isotropic stage-wise updated models also resulted in quite good calibration shots locations. The number of their exact locations was varying between 66 and 100% from stage to stage (Fig. 14). Location errors of mislocated shots were slightly higher than for a single-stage approach and reached 11 m. Nevertheless, this approach resulted in higher location accuracy in the vicinity of calibration shots (Fig. 15).

The largest areas of low mislocation values were observed in Stage 2, with CF0 reaching 0.34. Relatively high CF0 = 0.19 was observed also for Stage 3 (detailed values are given in Table 3).

It may be concluded that unlike in the single-stage case, adding data from consecutive stages takes advantage of increasing the area of subsurface being probed. However, when incidence angle coverage becomes significant, the isotropic model is not capable of providing accurate locations anymore, due to velocity variation with different incidence angles (see Fig. 5). Nevertheless, ultimately providing data from more stages had, in this case, a positive contribution to a final solution resulting in higher CF0s for all the stages when compared to the previous test (Table 3).

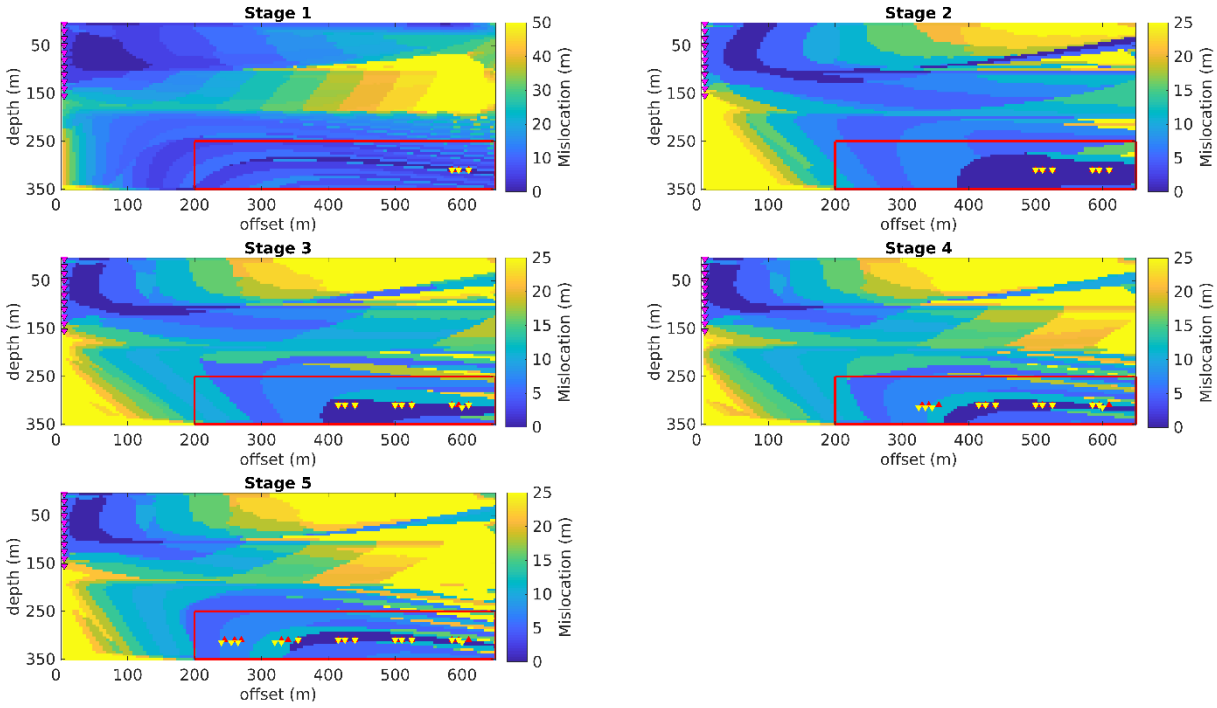

Fig. 14. Complete map of events mislocation for a set of 5 isotropic models (each per stage) for whole model space (test II). Mislocation is calculated as a Cartesian distance between expected and obtained location using the actual velocity model for each grid point. Expected positions of calibration shots are marked with red triangles, calibration shots locations obtained using the inverted velocity model are marked with yellow upside-down triangles. The red rectangle marks the area taken into account for CF0 calculation. Note that the maximum value at the color scale for Stage 1 is doubled.

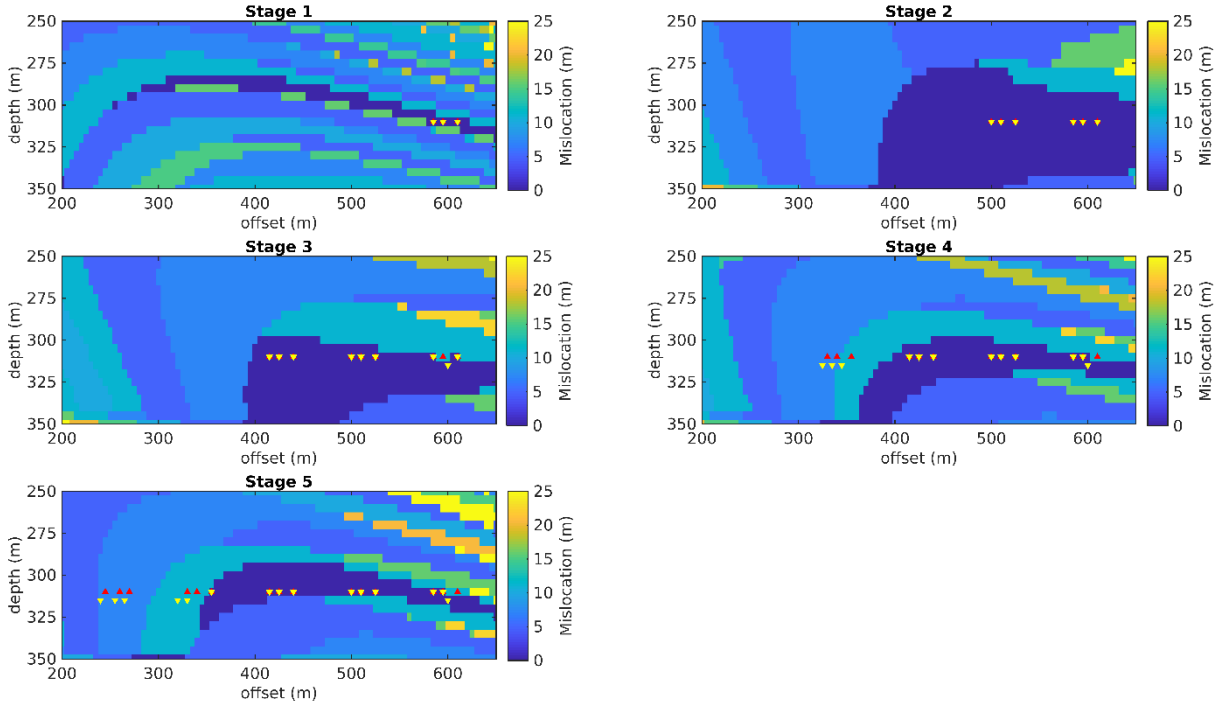

Fig. 15. Map of events mislocation for set of 5 isotropic models (each per stage) enlarged for selected area (zoomed into red rectangle in Fig. 14). Mislocation is calculated as a Cartesian distance between expected and obtained location using actual velocity model for each event. Expected positions of calibration shots are marked with red triangles, calibration shots locations obtained using inverted velocity model are marked with yellow upside down triangles. CF0 is calculated for whole visible area.

Table 3

Model correctness factor CF0 for modeling scenarios I–IV

Stage number	1	2	3	4	5
I. Proximate single-stage isotropic	0.0560	**0.0937**	0.0272	0.0387	0.0262
II. Proximate isotropic	0.0560	**0.3401**	0.1983	0.1282	0.1078
III. Proximate anisotropic	0.1088	0.7106	0.9158	**1.0000**	0.9801
IV. Distant anisotropic	0.0842	0.2517	0.2862	0.5735	**1.0000**

Note: Highest values highlighted in bold.

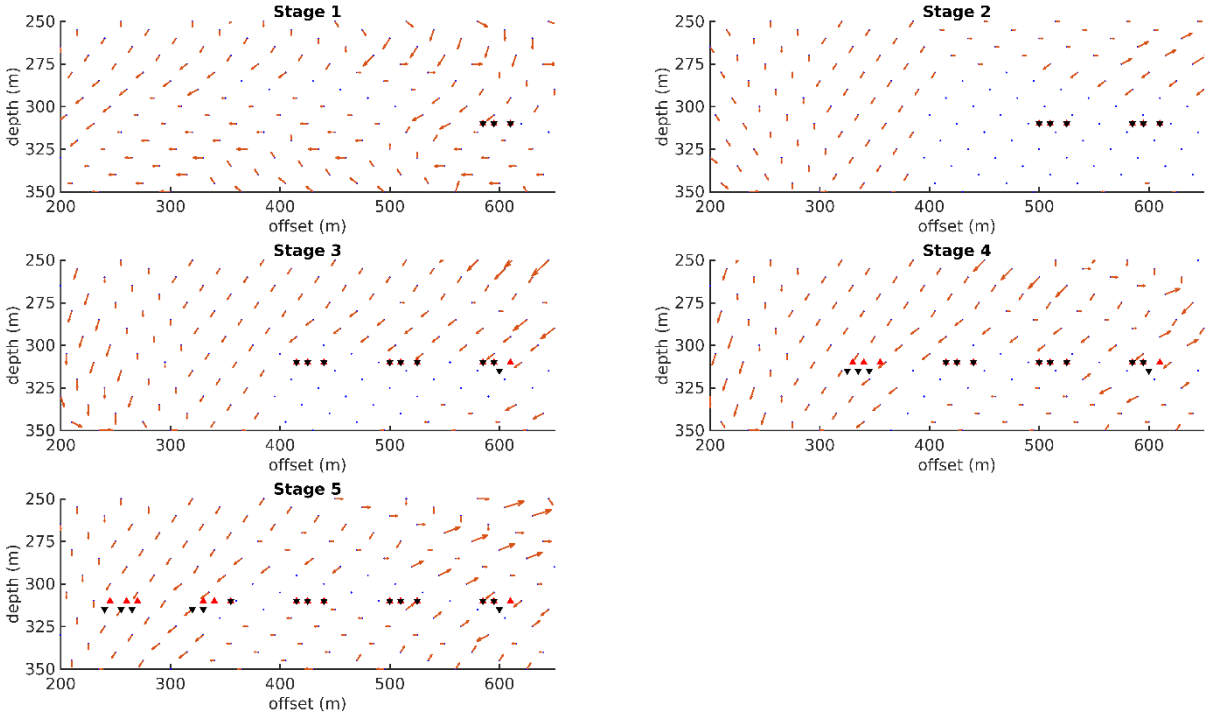

Fig. 16. Map of events mislocation directions for a set of 5 isotropic models (each per stage) enlarged for selected area (derived from Fig. 14). Vectors point from expected towards obtained location, however their length have been downscaled for clarity, therefore for mislocation magnitudes the reader is referred back to Fig. 15). Expected positions of calibration shots are marked with red triangles, calibration shots locations obtained using inverted velocity model are marked with black upside down triangles.

This observation provides an insight into the spatial validity of isotropic solution to anisotropic media. When looking closer at Stage 4 and 5 results (Fig. 15) it can be seen, that the 0-error area is located in the middle of the offset range of perforation shots, while locations of lateral perforations already exhibit some error. Isotropic model is fitted as a median solution, but the data span is too big to be correctly represented by the isotropic model only.

In this case, no consistent pattern can be inferred from Fig. 16.

III. Proximate anisotropic

Including Thomsen's anisotropic parameters in the inversion resulted in a much better resolved model than in both isotropic cases (Fig. 17). In Fig. 18, one can observe how 0 m mislocation area around the perforation shots is constantly expanding while more data is being included.

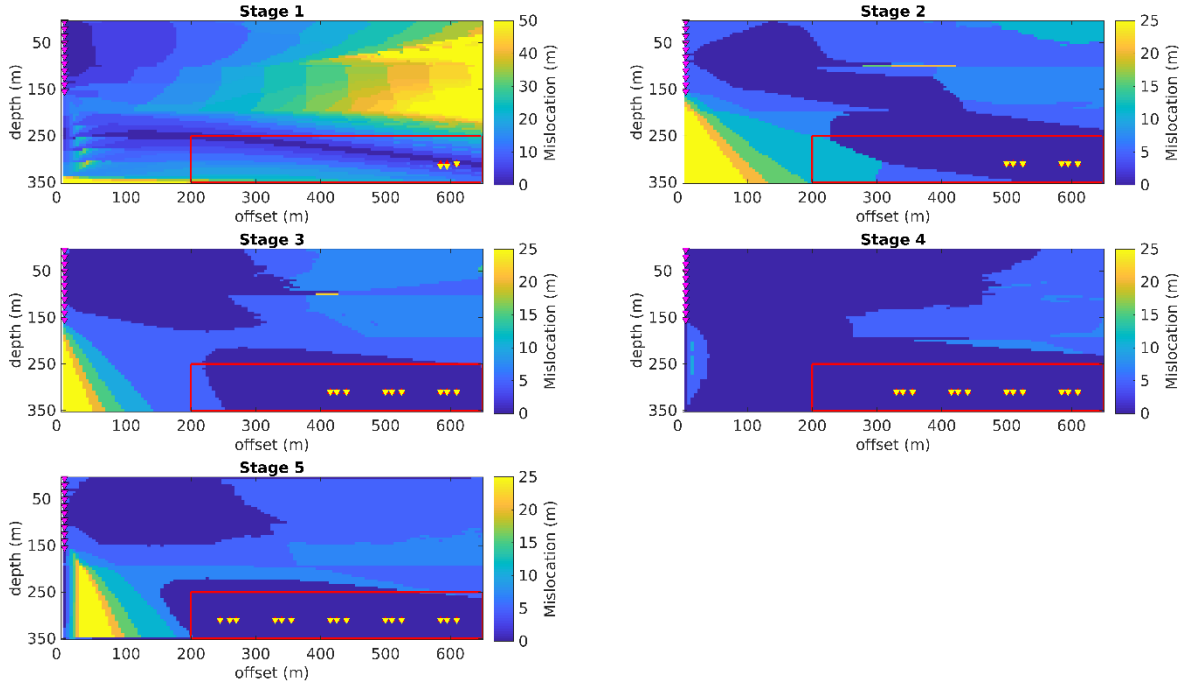

Fig. 17. Map of events mislocation for a set of 5 anisotropic models (updated with each stage) for whole model space (test III). Mislocation is calculated as a Cartesian distance between expected and obtained location using the actual velocity model for each grid point. Expected positions of calibration shots are marked with red triangles, calibration shots locations obtained using the inverted velocity model are marked with yellow upside-down triangles. The red rectangle marks the area taken into account for CF0 calculation. Note that the maximum value at the color scale for Stage 1 is doubled.

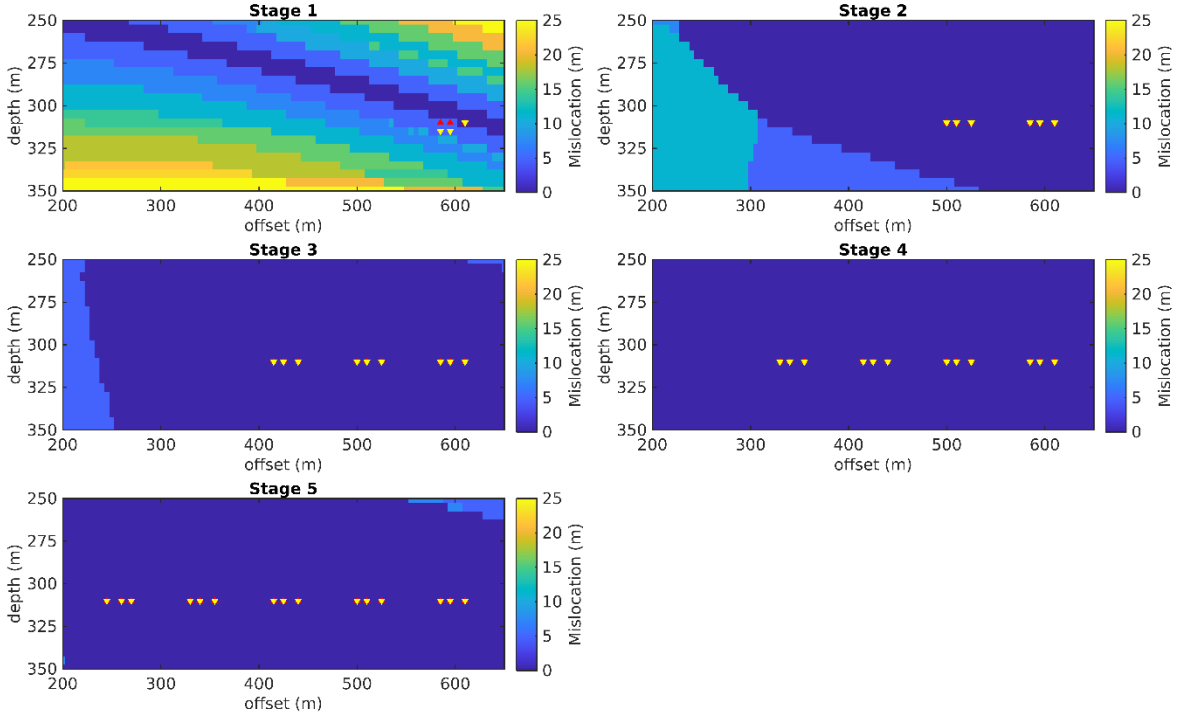

Fig. 18. Map of events mislocation for set of 5 anisotropic models (updated with each stage) enlarged for selected area (zoomed into red rectangle in Fig. 17). Mislocation is calculated as a Cartesian distance between expected and obtained location using actual velocity model for each event. Mislocation is clipped to maximum 50 m for Stage 1, and to 25 m for other stages. Expected positions of calibration shots are marked with red triangles, calibration shots locations obtained using inverted velocity model are marked with yellow upside down triangles. CF0 is calculated for whole visible area.

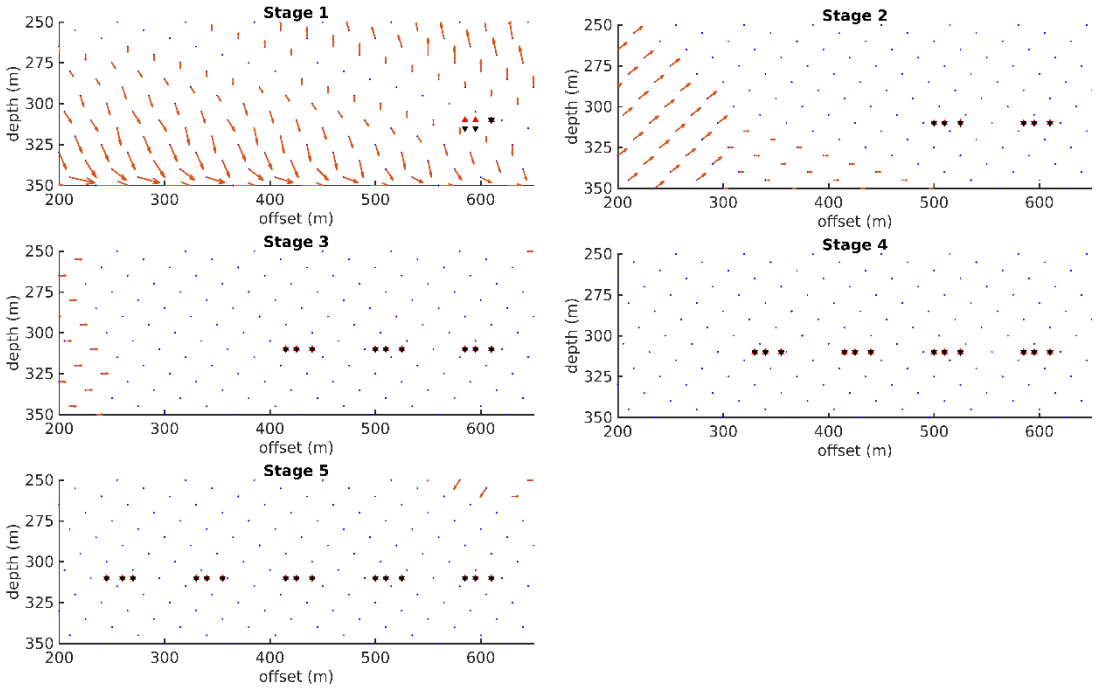

Fig. 19. Map of event mislocation directions for a set of 5 anisotropic models (updated with each stage) enlarged for selected area (derived from Fig. 17). Vectors point from expected towards obtained location, but their length have been downscaled for clarity; therefore, for mislocation magnitudes the reader is referred back to Fig. 18. Expected positions of calibration shots are marked with red triangles, calibration shots locations obtained using inverted velocity model are marked with black upside down triangles.

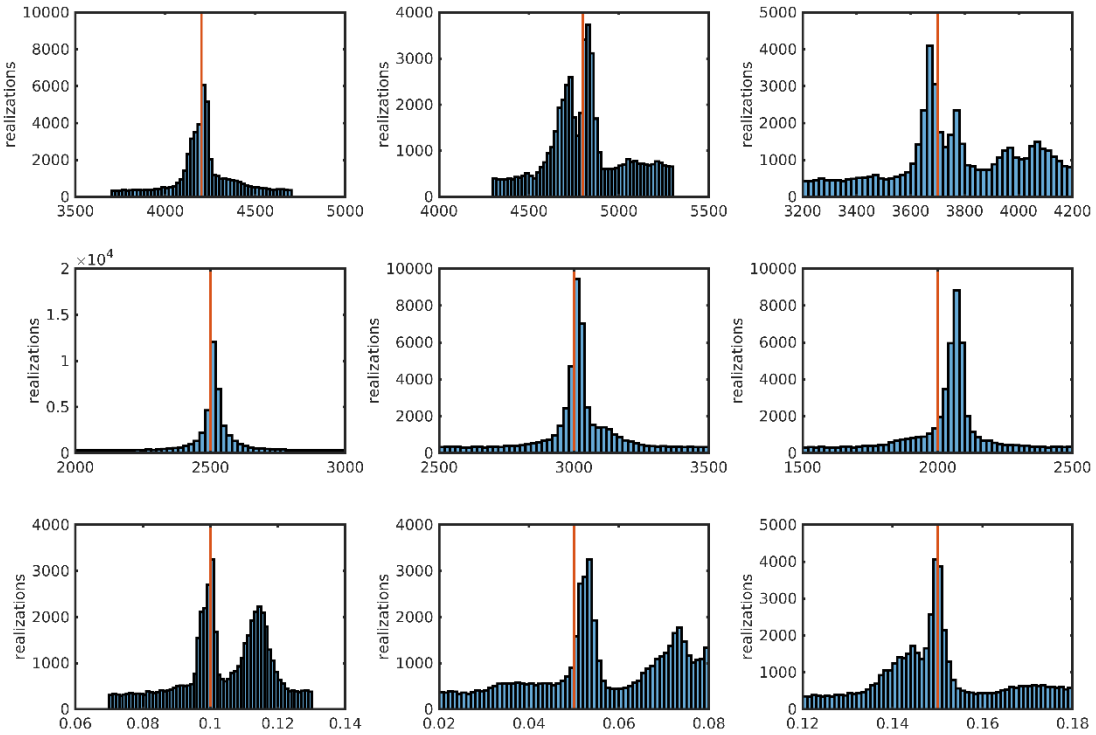

Fig. 20. 1-D marginal PDFs for all 9 model parameters obtained by the sampling algorithm (using the NA ensemble) in inversion for Stage 5. The prior distributions were uniform. The panels are arranged so that 1st row represents V_P0 for each layer, 2nd row represents V_S0 for each layer and 3rd represents Thomsen parameters: ε, δ, and γ, respectively. The red solid lines show the true value of each model parameter.

The Stage 1 model has a strong similarity to the isotropic models in terms of CF0 (only 0.08) and circular trend of events mislocation (Fig. 19). Low CF0 is caused by limited incidence angles among calibration shots, and hence, limited information about the anisotropy, showing limited possibilities of accounting for anisotropy when data span is significantly limited. Nevertheless, in the Stage 2, when more data is available, CF0 already grows to 0.71 showing superiority of this approach over the isotropic multi-stage case already in this early stage.

Finally, when data from consecutive stages is being added further the CF0 continue to grow and reaches 1 at Stage 4 (Table 3). In Stage 5, CF0 decreases to 0.98, which should be accounted for an influence of a random noise added to the traveltimes. An example of marginal distribution of PDF of each free parameter for Stage 5 is presented in Fig. 20 to provide some insight into parameter sampling and inversion convergence. For some parameters, a bimodal distribution can be recognized. Nevertheless, in this case, the solution closer to the expected one has been chosen.

Clearly, much better accuracy of events locations can be reached when anisotropy is included in the inversion. Importantly, the results indicate that accurate locations are obtained not only for the calibration shots but also for their surroundings up to distances where most of the microseismic events are expected to occur during hydraulic stimulation.

IV. Distant anisotropic

This case is analogical to modeling III, but with offsets shifted 1 km away from the monitoring borehole to simulate the geometry of the Wysin experiment. Results show high similarity to the previous case, with CF0 stably growing from stage to stage (Fig. 21), to finally reach 1 in the last of them (Table 3). However, here, the CF0s grows much slower when comparing to the

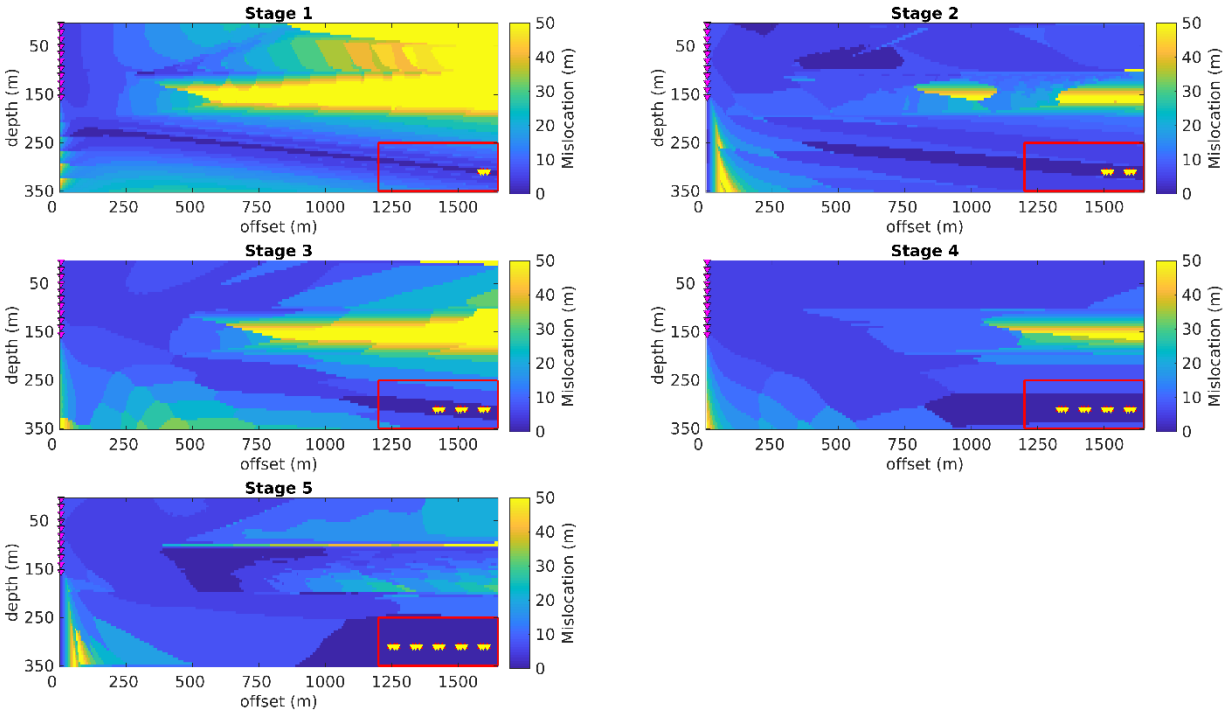

Fig. 21. Map of event mislocation for a set of 5 anisotropic models (updated with each stage) for whole model space (test IV). Mislocation is calculated as a Cartesian distance between expected and obtained location using the actual velocity model for each grid point. Mislocation is clipped to a maximum of 50 m. Expected positions of calibration shots are marked with red triangles, calibration shots locations obtained using the inverted velocity model are marked with yellow upside-down triangles. The red rectangle marks the area taken into account for CF0 calculation.

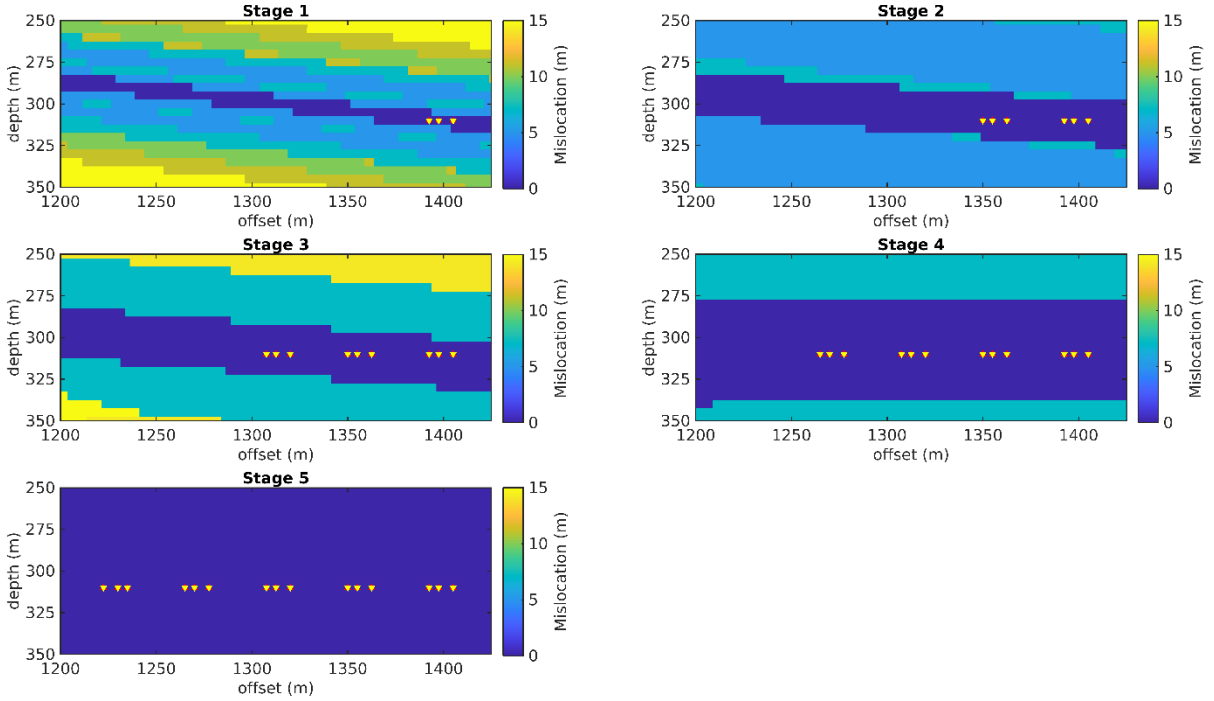

Fig. 22. Map of events mislocation for a set of 5 anisotropic models (updated with each stage) enlarged for selected area (zoomed into red rectangle in Fig. 21). Mislocation is calculated as a Cartesian distance between expected and obtained location using actual velocity model for each event. Expected positions of calibration shots are marked with red triangles, calibration shot locations obtained using inverted velocity model are marked with yellow upside down triangles. CF0 is calculated for whole visible area.

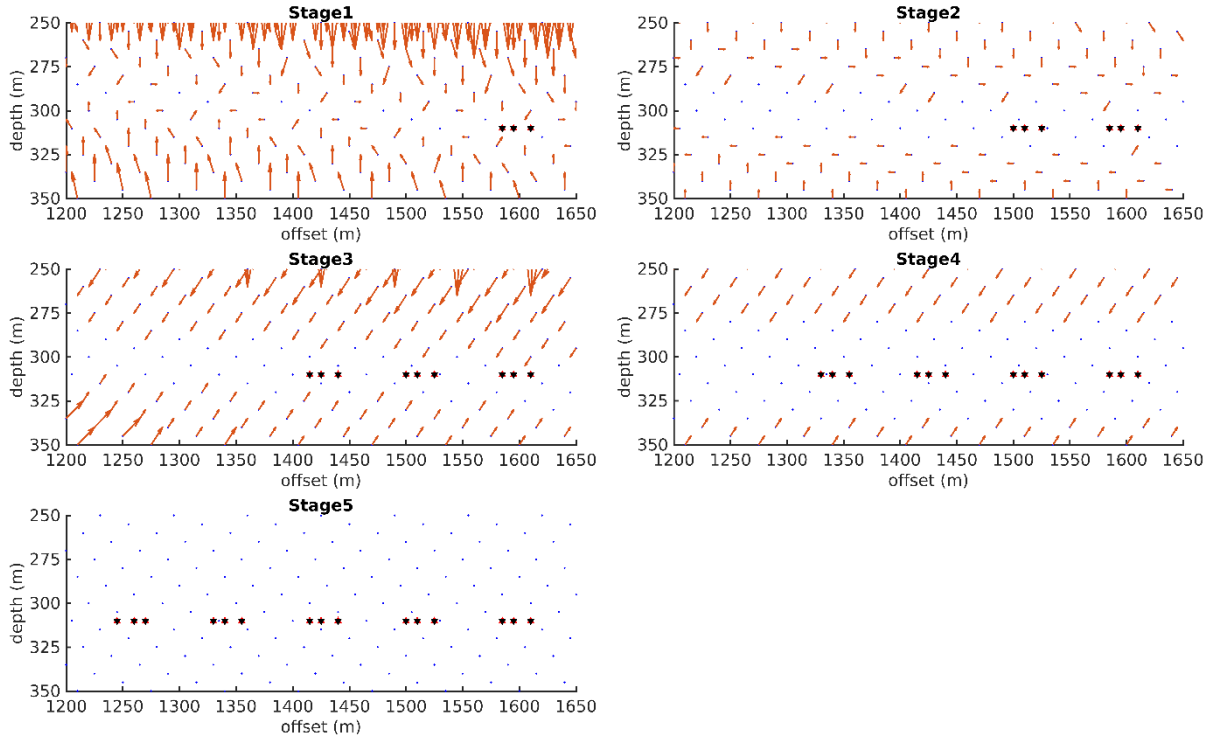

Fig. 23. Map of events mislocation directions for a set of 5 anisotropic models (updated with each stage) enlarged for selected area (derived from Fig. 22). Vectors point from expected towards an obtained location, and their length is shown in a true scale. Expected positions of calibration shots are marked with red triangles, calibration shot locations obtained using inverted velocity model are marked with black upside-down triangles.

proximate case (Fig. 22), because of limited incidence angles sampling due to greater distance. It can also be observed that the 0-error area is limited only to the vicinity of the calibration shots. This effect is caused by the greater distance to the borehole.

From inspection of Fig. 23 it can be seen, that inverted locations are being pushed vertically towards the perforation shot.

V. Thinning layer accuracy test

This test was performed to asses possible accuracy of the inversion in terms of minimum layer thickness for which reliable parameters can be obtained. Differently from previous cases, all the available data from five stages were used at once, to simulate the most favorable conditions. The thickness of a middle layer was being decreased from 100 to 1 m with 5 m increment, resulting in 21 inversion results, keeping the grid resolution of 5 m. When the bottom of the middle layer was moving upwards in subsequent iterations, simultaneously the top of the lowermost layer was lifted to keep the model consistency.

For this test, a 3-layer velocity model, similar to previous cases, was used. Model parameters are given in Table 4. The only differences were varying middle layer thickness, and the presence of anisotropy ($\varepsilon = 0.1$, $\gamma = 0.15$, $\delta = 0.05$) in the middle layer only. The proximate (Lubocino) setting with data from five stages was used.

Table 4

Parameters of synthetic model used in the modeling V

Layer	Top depth [m]	Thickness [m]	V_P0 [m/s]	V_S0 [m/s]	$\in$	δ	γ
1	0	100	4200	2500	0.0	0.0	0.0
2	100	1–100	4800	3000	0.10	0.05	0.15
3	101–200	120–220	3700	2000	0.0	0.0	0.0

The minimal thickness of the anisotropic layer for which its parameters can be reliably retrieved was determined by tracking the stability of inverted parameters with decreasing layer thickness and corresponding CF0s. Results are plotted in Fig. 24.

From its inspection, it can be inferred that the minimum layer thickness of 60 m should be considered, mainly due to a critical decrease of CF0 below this thickness. Till this limit velocities for all the layers and γ are stable, while ε and δ are slightly fluctuating around the expected values. Nevertheless, CF0 is kept as 1 as long as the thickness stays above 60 m. This limit is dictated by lowering the influence of the anisotropy on the traveltimes due to decreasing layer thickness. True parameters of the middle layer cannot be tracked anymore, and the thin anisotropic layer is tried to be explained by increasing the velocities, however the key parameter CF drops dramatically.

When the thickness of anisotropic layers drops to 1 m, the model becomes close enough to isotropic to make the CF0 to increase up to 0.82.

The minimum thickness of the anisotropic layer that has been estimated may be much higher than required for some of the shale gas exploration applications. Therefore, in order to provide a possible solution to account for anisotropic layers that are too thin to be resolved, estimation of the effective anisotropy is examined in the next test.

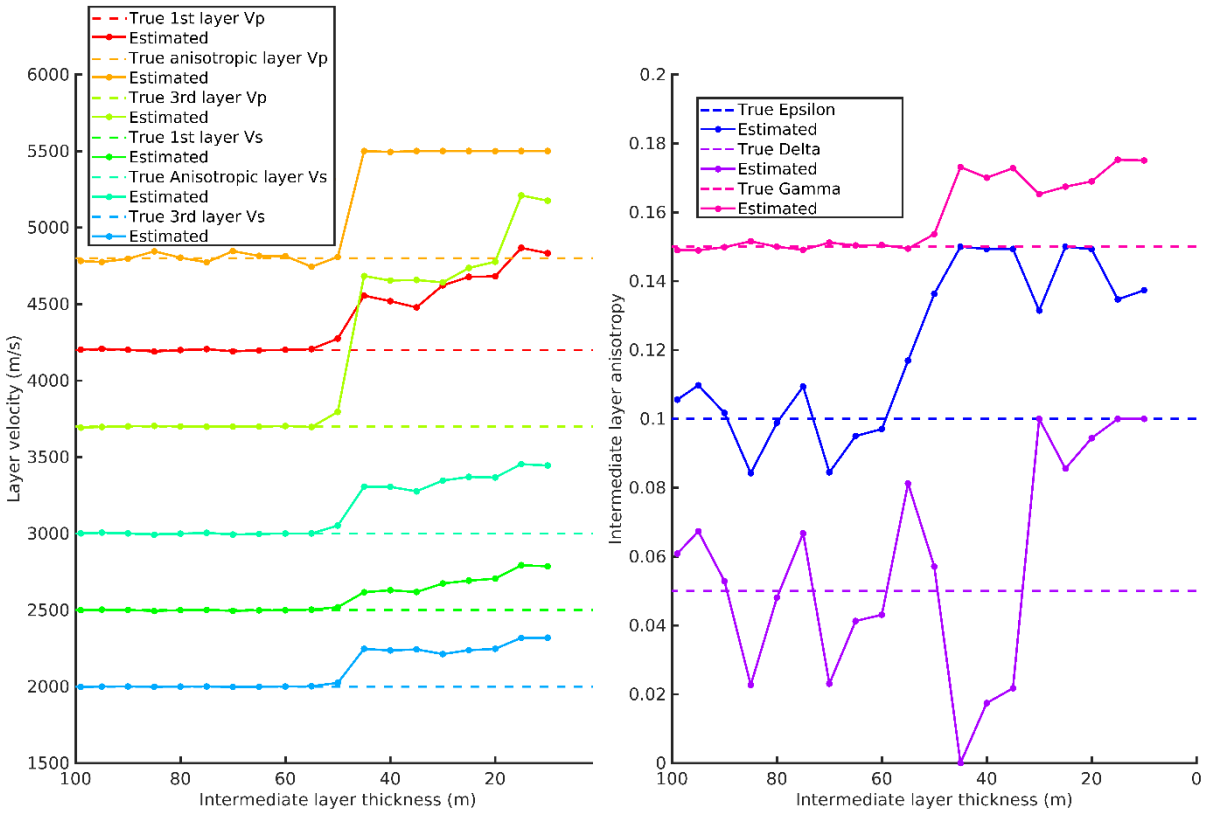

Fig. 24. Best fitted parameters in subsequent anisotropic velocity model inversion with thinning middle layer (test V) and corresponding CFs. The black plot at bottom panel indicates mean relative error of best fitted parameters with respect to expected parameter values.

VI. Effective anisotropy

This test was performed to verify how accurately the anisotropic model built of differently anisotropic layers can be described by effectively anisotropic medium (Banik 1987; Sena 1991) accounting for various velocities but global Thomsen's parameters for whole model space. This inversion scenario may be implemented when the strength of anisotropy is varying from layer to layer or when the layer thickness is too thin to be resolved in test V (Backus 1962).

Two scenarios of anisotropy strength were considered, with varying Thomsen's parameters in the lowermost, thickest layer containing perforation shots. Parameters of both models are listed in Table 5. Since two out of three layers anisotropic parameters are kept equal only the differences were shown (in brackets) for anisotropic scenario 2. Vertical velocities and layer

Table 5

Parameters of synthetic model used in effective anisotropy modeling

Layer	V_P0 [m/s]	V_S0 [m/s]	ε	δ	γ
1	4200	2500	0.04	0.02	0.05
2	4800	3000	0.07	0.03	0.09
3	3700	2000	0.05 (0.1)	0.01 (0.05)	0.04 (0.13)

Note: Thomsen's parameters varying between two presented cases are given in the brackets.

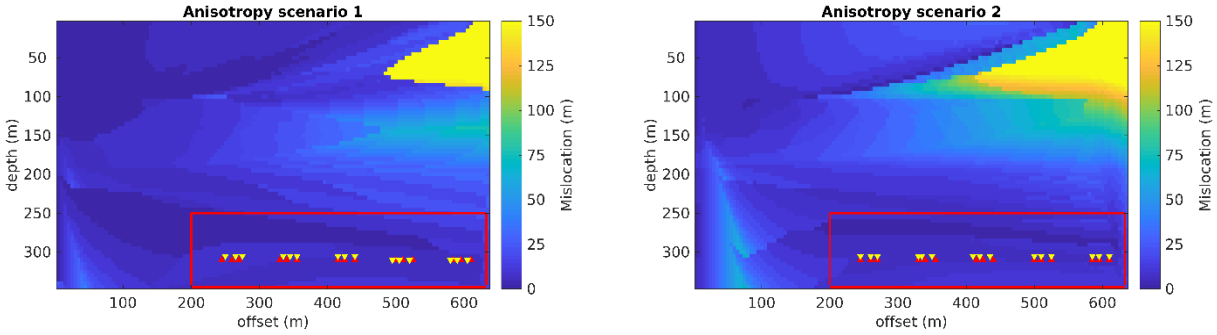

Fig. 25. Complete map of events mislocation for effectively anisotropic models (two scenarios of anisotropy) for whole model space (test VI). Mislocation is calculated as a Cartesian distance between expected and obtained location using the actual velocity model for each grid point. Expected positions of calibration shots are marked with red triangles, calibration shots locations obtained using the inverted velocity model are marked with yellow upside-down triangles. The red rectangle marks the area taken into account for CF0 calculation. Mislocation has been clipped to maximum value of 150 m.

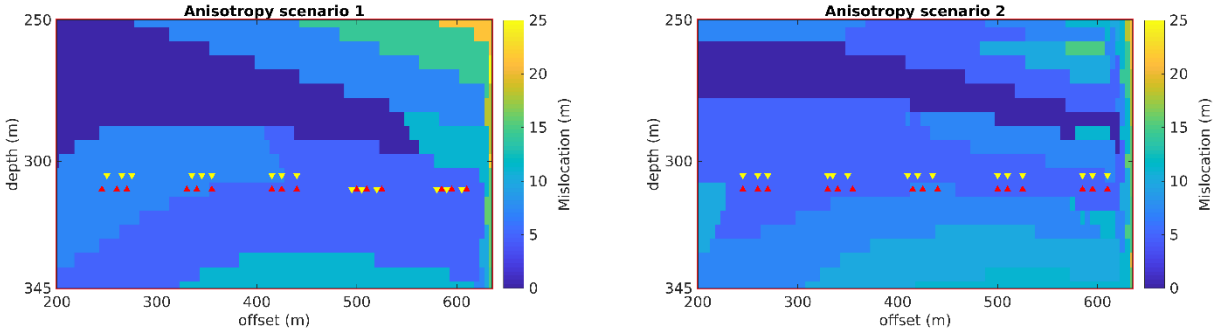

Fig. 26. Map of event mislocation for effectively anisotropic models (two scenarios of anisotropy) (zoomed into red rectangle in Fig. 25). Mislocation is calculated as a Cartesian distance between expected and obtained location using actual velocity model for each event. Expected positions of calibration shots are marked with red triangles, calibration shots locations obtained using inverted velocity model are marked with yellow upside down triangles. CF0 is calculated for whole visible area.

geometry were kept consistent with previous modelings. Mislocation maps were computed as for previous examples.

The obtained results indicate that for tested geometry both anisotropic scenarios can be resolved by an effective anisotropy approach (Fig. 25). When looking at resulting misfit maps in detail (Fig. 26), it can be observed that event mislocation in the area of main interest is not exceeding 15 meters. CF0s for both cases reached only 0.23 and 0.14, respectively. Importantly, small, 5 to 10 m error is present in calibration shots locations. Nevertheless, computing CF1s (CF with the tolerance of one grid node error, 5 m) gave much higher values of 0.81 and 0.77, respectively. This indicates that in this case inverting effectively anisotropic model resulted in models providing not exact, but close to expected locations of microseismic events for almost 80% of the zone of interest area.

3.2.2 Feasibility of real-time inversion

Hydraulic fracturing is a complex, time-consuming operation usually involving from few up to even twenty or more fracturing stages in one horizontal borehole. Prior to each of the stimulations, a particular borehole interval needs to be perforated. Preparation for each stimulation involves gathering the necessary water resources on the site, specifying an amount of proppant to be used in a particular stage and planning the chemical composition of the slurry to maximize the treatment effectiveness. Industrial practice is to advance with subsequent stages usually not

faster than one operation per day. During the stimulation and also after, before proceeding to the next stage, an assessment of its effectiveness needs to be performed.

Therefore, it takes at minimum one day from perforating the desired interval to the main stimulation. To be able to locate the induced microseismicity using an updated anisotropic velocity model, the velocity model inversion should be done during the night.

There are usually only a few perforation shots per stage, so extracting their seismograms and picking the first breaks is not a time-consuming process. Hence, the only concern is on the computational part. Following methodology presented in this thesis, the CPU time will vary due to (i) the model complexity: the number of layers, the size of the model, density of the grid points, and (ii) due to the desired accuracy of the optimization algorithm (here NA sampler by Sambridge (1999a) is employed). The number of perforation shots does not contribute significantly to the computation time, and hence, can be neglected.

Regarding the model complexity factor, I presented examples of two different 3-layer models with dimensions 700×350 m and 1700×350 m and with grid spacing of 5 m. In each isotropic model inversion, 6 free parameters were inverted, while in inversions including anisotropy 9 free parameters were inverted. The more free parameters are being inverted, the more realizations of the forward problem require the inversion to converge in a global minimum. Therefore, the increasing complexity of the model increases the computation time nonlinearly. Respective computation times are given in Table 6.

Although the scope of this thesis is resolving anisotropy, the isotropic inversion was included in the table for comparison.

Table 6

Comparison of computation times for different inversion approaches

Model	CPU time on 22 cores	Total CPU time	Number of realizations	Number of free parameters
700×350 m isotropic	1 h 40 min	36 h 40 min	33000	6
700×350 m anisotropic	6 h	132 h	51000	9
1700×350 m anisotropic	8 h	176 h	51000	9

With nowadays technology total CPU times of the order of 100–200 hours are possible to accomplish, as assumed during the night. These resources can be available on the site. Otherwise, even a small remote computing cluster can be easily used for the calculations. Therefore, implementing on-site real-time inversion of anisotropic velocity model during an ongoing hydraulic fracturing job is undoubtedly possible.

3.3 Conclusions from this chapter

In this chapter, I introduced the algorithm of the probabilistic event location and its possible applications. Also, I developed the technique for VTI anisotropic velocity model inversion using traveltimes of calibration shots or perforation shots. Inversion methodology is supplemented by a set of synthetic tests in order to compare the accuracy of resulting velocity models with isotropic solutions and benchmark the technique in particular applications. The chapter is completed with a discussion on the feasibility of implementing the presented methodology in real-time to ongoing hydraulic fracturing monitoring campaign.

The Bayesian approach for the microseismic event location provides a better insight into the problem than the standard approach in terms of uncertainty assessment. This approach offers individual distributions of location PDF for each event. What's more, those distributions

are unique in their 3D shape. The cumulative location PDF clearly can point out highly fractured zones and show directly the scale and the character of the location uncertainty. Moreover, it can be scaled by, e.g., moment magnitude to produce easy to analyze maps having the advantage of transparency over visualization approaches.

The new technique of traveltime-based anisotropic velocity model inversion proved to be effective in terms of velocities and anisotropic parameters estimation resulting in accurate locations of microseismic events. Presented synthetic tests showed that accounting for the anisotropy in the inversion procedure greatly improves the accuracy of microseismic events locations and that it is always beneficial to account for the anisotropy during velocity model inversion whenever dealing with anisotropic media. The accuracy of locations using anisotropic models is superior when comparing with isotropic ones (tests I, II, and III).

When only isotropic models are inverted (tests I and II), updating the model provides better results in terms of event mislocation than a single-stage approach. Nevertheless, when updating the isotropic models, the performance of the updated model is related to the strength of the anisotropy, and hence, spatial model correctness should be expected to be case-dependent. In the studied case with particular strength of anisotropy, a uniform model for two stages resulted in the best results quantified as the least deviation from the perforation shot location. Model performance can be assessed by synthetic modeling of expected anisotropy; however, when such modeling is available implementing anisotropic inversion is also available. Also in multistage isotropic model approach, least errors are expected to occur in the center of the region containing calibration data, while extreme calibration points can already experience significant mislocation errors (test II).

Tests III and IV positively validated the proposed velocity model inversion methodology. Test results prove that the presented approach provides model accuracy suitable to be used in hydraulic fracturing monitoring operations.

Test V aimed in the assessment of limits of inversion capabilities in case of minimum layer thickness in a particular setting, corresponding to the geometry of the Lubocino experiment described in the next chapter. The minimum layer thickness for which anisotropic parameters and velocities can be inverted correctly was estimated as 60 m.

Test VI presented the accuracy of event locations when effective anisotropy is considered. In this application, inversion methodology resulted in being less accurate. However, still, almost 80% of the zone of interest area was resolved with event mislocation not greater than 5 m, which is still satisfactory in terms of field data applications.

4. BUILDING AN ANISOTROPIC VELOCITY MODEL FOR MICROSEISMIC EVENT LOCATION

In this chapter, I present an application of VTI anisotropic velocity model inversion described in Chapter 3 to the real data from Lubocino microseismic monitoring experiment. Due to the lack of *SH* arrivals in perforation shot records, the methodology presented in Chapter 3 is modified by incorporating traveltimes of microseismic events in order to obtain parameter γ. Then I locate the microseismic events and give the geomechanical interpretation of stimulation performance. The experiment geometry, geological setting, and data availability were described in the Introduction section. This chapter is an elaborated version of Gajek et al. (2018b).

4.1 Data and initial data processing

4.1.1 Perforation shots

The data processing sequence started from identifying the perforation shots in the dataset. Some general information about the perforation shots was provided, but the exact origin times of the shots were unknown. Stack of vertical components from all 11 receivers at the approximate

time of the shots was scanned using STA/LTA based detector (Allen 1978) to detect the strongest events. Then perforation shots were identified as most prominent events having expected moveouts (propagating from the reservoir upwards towards the receiver array). Signals from all shots performed with Hydra-jet technology (hydroperforation) numbered 1, 4, and 5 (Table 7) were not visible in the data. The record of perforation shot example is shown in Fig. 27.

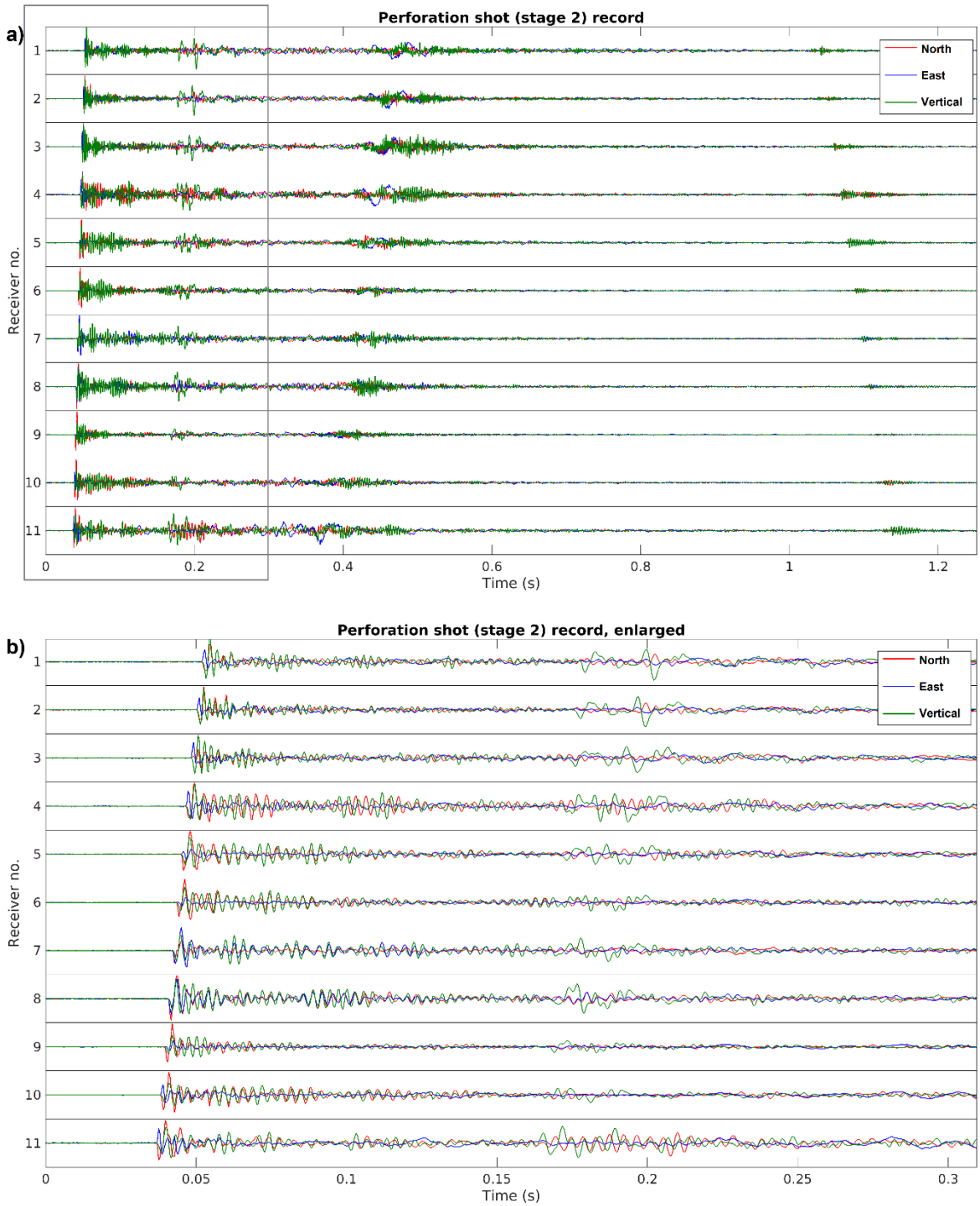

Fig. 27. Raw records of a perforation shot from Stage 2. Note extremely high amplitudes of the signal. Most prominent are the *P*-wave arrivals at 0.05 s, *S*V arrivals visible at 0.2 s, two reflections from some lower and upper reflectors visible at 0.4 s and 1.1 s, respectively, no *SH* wave is visible. Section a) shows a full-length record, section b) shows enlarged *P*- and *SV*-waves arrivals of the same event marked with gray rectangle in section a).

Table 7

Perforation shots

No.	Stage	Type	Offset [m]	Depth [m]	*P*-wave picks	Fast *S*-wave picks	Slow *S*-wave picks
1	1	Hydra-jet	694	2925	0	0	0
2	2	Plug-and-perf	611	2925	11	0	9
3	3	Plug-and-perf	526	2925	11	0	11
4	3	Hydra-jet	513	2925	0	0	0
5	3	Hydra-jet	507	2925	0	0	0
6	4	Plug-and-perf	454	2924	11	0	11
7	4	Plug-and-perf	441	2924	11	0	11
8	4	Plug-and-perf	428	2924	11	0	11
9	5	Plug-and-perf	369	2923	11	0	11
10	5	Plug-and-perf	356	2923	11	0	11
11	5	Plug-and-perf	343	2923	11	0	11
12	6	Plug-and-perf	285	2925	11	0	11
13	6	Plug-and-perf	282	2925	11	0	11
14	6	Plug-and-perf	272	2925	11	0	11
15	6	Plug-and-perf	269	2925	11	0	11
16	6	Plug-and-perf	259	2925	11	0	11

Arrivals of 13 detected perforation shots (those done with blasting) were picked manually. Clear *P*- and mostly clear slow *S*-wave (*SV*)[2] arrivals were observed for each of the shots, while fast *S*-waves (*SH*) were observed only on few traces, but were impossible to pick. The lack of fast *S*-wave energy can be explained by the explosive source mechanism, where theoretically no shearing is observed (Grechka and Heigl 2017) and also unfavorable radiation pattern in case of non-volumetric source mechanism components.

For *P*- and *SV*-waves, clear and high amplitude arrivals were usually observed. *P*-wave was picked for all shots on all traces. Two picks of *SV*-wave were skipped in the case of the first, most distant shot due to the lack of clear onsets and none of the *q-SH* arrivals was picked.

4.1.2 Determining the orientation of geophones

To assure the reliability of microseismic recordings, the knowledge on the position of the sensors is necessary. The depth of the tool string is known with enough precision just by monitoring the cable length when inserting the tool string into the borehole. Information on the depth of the receivers was provided by the contractor. Instruments are assumed to be vertically aligned with the borehole due to having a mechanical arm preventing them from tilting. However, they

[2]For the brevity, the qualifiers in "quasi *P*-wave" and "quasi *S*-waves" are omitted.

still can rotate around the cable during the placement, and the orientation of horizontal components is unknown (DiSiena et al. 1984). Therefore, to be able to determine the position of registered events of unknown locations, a calibration has to be done beforehand (e.g. Becquey and Dubesset 1990; Zaręba and Danek 2019). In order to determine the tool string rotation, a record of some events with known locations can be used, usually, the perforation shots (Maxwell 2014).

To determine the perforations' back-azimuth for each receiver, 100 samples long *P*-wave hodograms of *X* and *Y* horizontal components were used. Taking advantage of an approximately constant borehole azimuth towards the monitoring well for each stage (see, e.g., Fig. 38), hodograms of each of 13 registered shots were stacked at single receivers to limit the fitting uncertainty. A standard linear regression with line parameter $b = 0$ was performed providing a

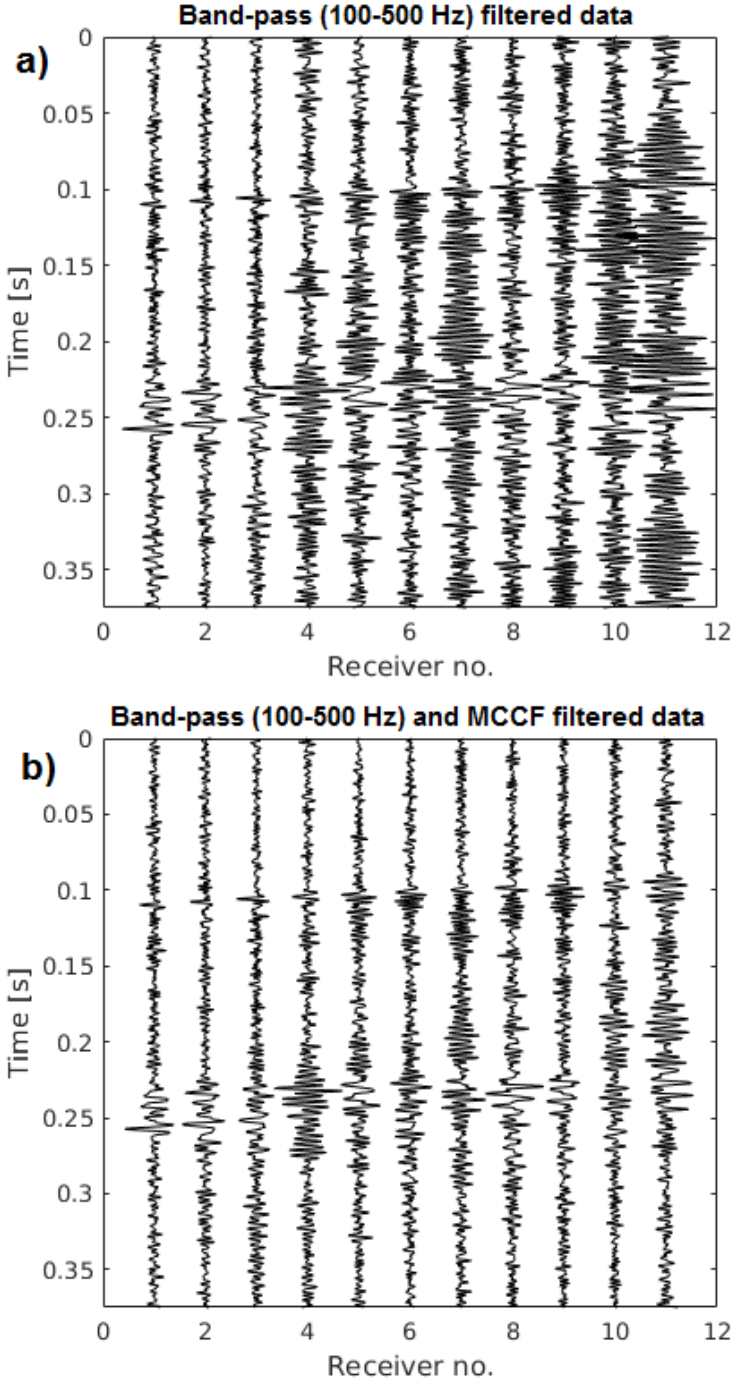

Fig. 28. Downhole array record of an event recorded during hydraulic fracturing (vertical components only). The raw data with a band-pass filter (a) and data filtered by MCCF and then band-pass filter (b) (Trojanowski et al. 2016).

direction towards the shot location due to linear polarization of *P*-waves and positive first arrivals expected from explosive sources. Then, horizontal receiver components were rotated from sensor to geographical reference frame (*Z*, *X*, *Y* to *Z*, *E*, *N*), keeping in mind clock-wise orientation of Avalon receiver components.

4.1.3 Microseismic events detection

For the detection of events, a standard STA/LTA detection algorithm (Allen 1978) was run on each component for the filtered data. Even though the downhole environment is usually more favorable for microseismic monitoring in terms of noise level, because of sources and receivers proximity and the lack of cultural or weather noise, a considerable level of noise was observed most probably due to some open perforations and high fluid level in the observation well (according to the contractor), suppressing some of the weakest events. Hence, the data were prefiltered using a multichannel convolution filter (MCCF) for correlated noise (Trojanowski et al. 2016; Trojanowski 2019) followed by a standard 80–600 Hz band-pass filter. The performance of MCCF is shown in Fig. 28.

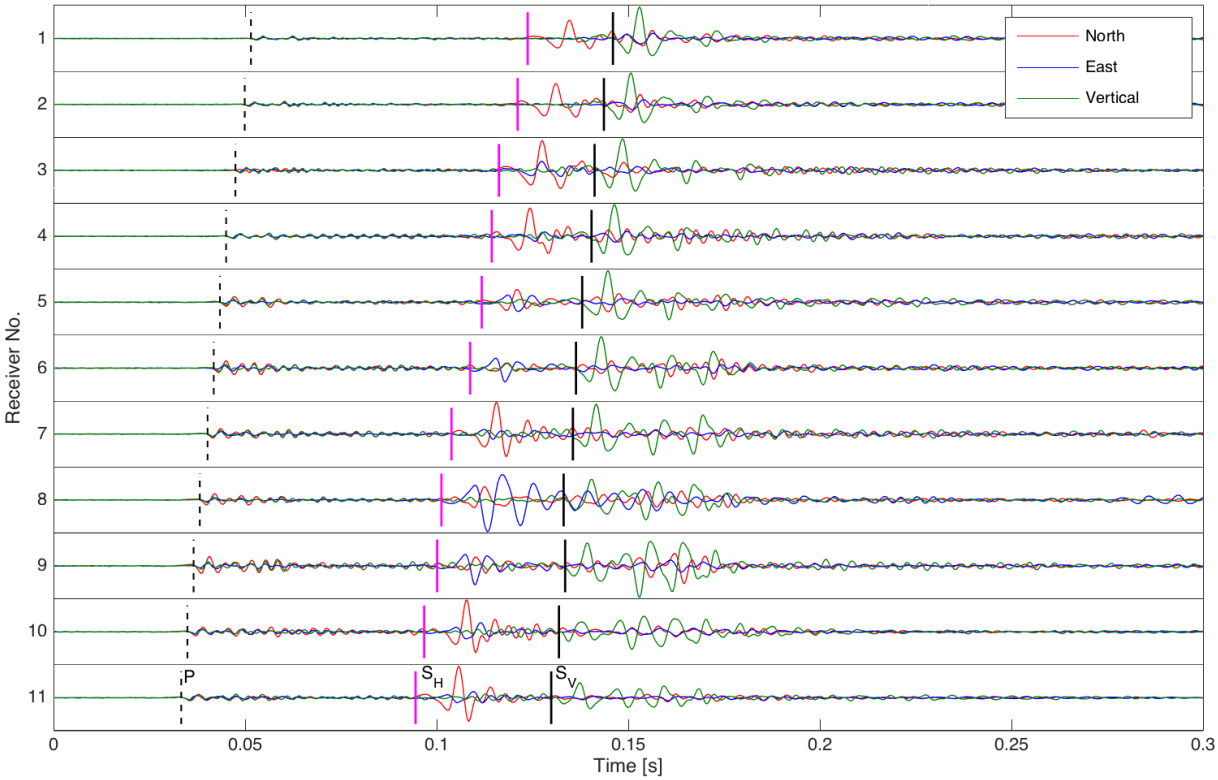

Fig. 29. Waveforms from example of a microseismic event recorded by the 11 3C geophones. An event with strong SWS, producing significant time delays (19–37 ms) between fast and slow *S*-wave. Picks are labeled on the bottom trace, geophones labeled from top to bottom.

4.1.4 Arrivals picking

In order to locate an event using traveltime based methods, accurate onsets of each wave on corresponding traces have to be identified (Fig. 29). This can be done either manually or automatically. In this case, I picked the traveltimes manually to gain sound insight into the data and guarantee a high picking accuracy despite noisy recording conditions. To browse the seismograms and pick the first breaks of *P*-, *SH*-, and *SV*-waves I created a dedicated software – a graphical user interface (GUI) in Matlab (Fig. 30). This software provided means for visual

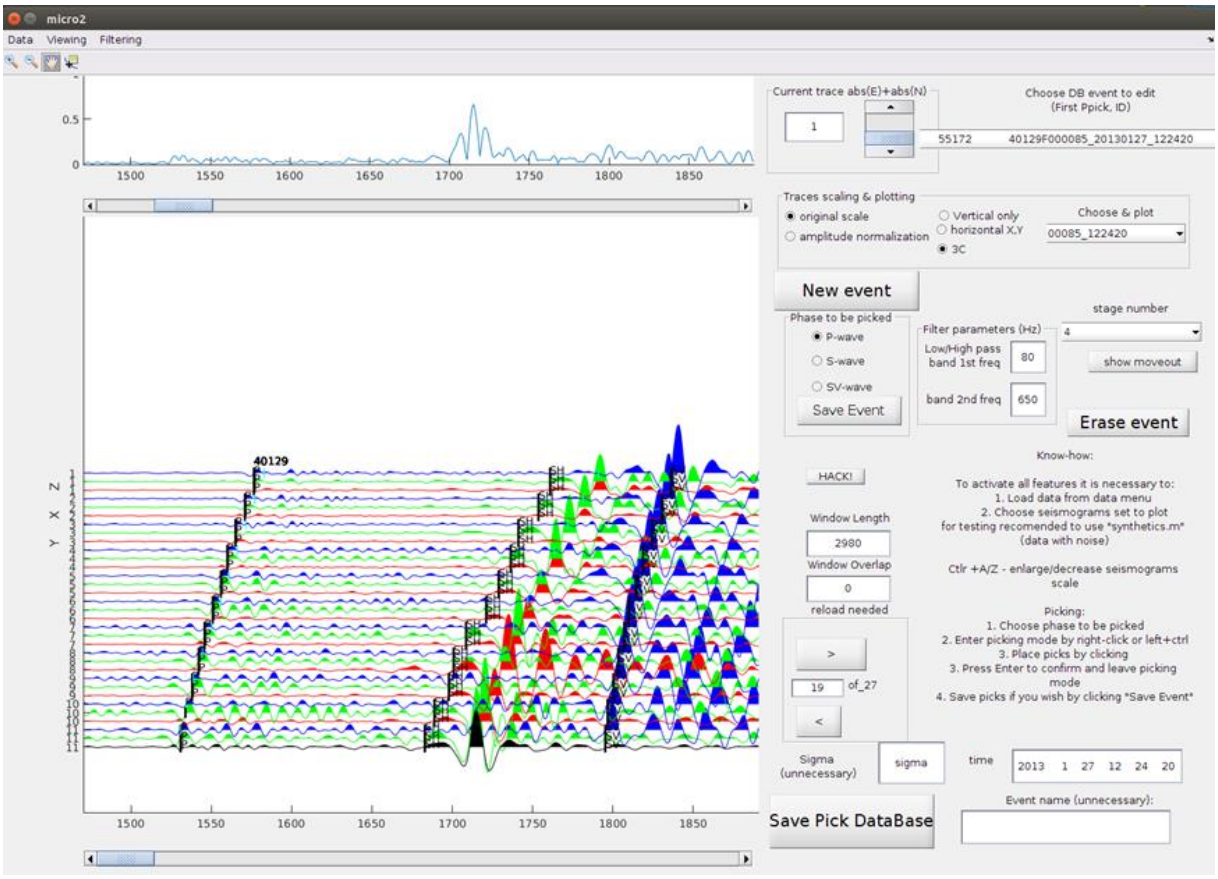

Fig. 30. A Matlab GUI created for microseismic records processing. An example of an event with all three phases picked at all of the receivers is shown in the main window.

inspection of the detections, their quality control (accepting as microseismic event or discarding), picking *P*, *SH*, and *SV* arrivals, filtering, displaying theoretical picks (from rough velocity model based at this stage on sonic logs), setting semi-automated picks within a single event range based on expected moveout projection and updating an external event database.

The majority of the detections had the most prominent, high amplitude *SH*-wave onsets, which were triggering the detector. All detections not having a proper moveout (i.e., propagating downwards) were discarded. If *q-SH* and *P*-wave onsets were distinctive enough to be picked at least on few traces, a detection was considered as an event. When the *q-SV* wave was present, it was always picked when possible. In the end, over 1600 events were picked at the initial stage. However, in the final analysis, 1385 events were taken into account, due to e.g., wrong picked traces, duplicates or being located outside the model space (after inverting the final anisotropic velocity model). The catalog of picks for the 1385 events dataset consisted of 15101 *P*-wave picks, 14974 *SH*-wave picks, and 7418 *SV*-wave picks. *SV* onsets were most often easily recognizable in the records. However, marking the arrival was, in many cases, challenging. Such prepared events were ready to be located just after obtaining an accurate velocity model.

4.2 Anisotropic velocity model building

The velocity model is necessary to obtain locations of microseismic events. Perforation shots, whose locations are known, are used to benchmark the model. A velocity model that provides locations of the perforations close to the expected location will also provide proper locations of microseismic events in their vicinity. The service company provided isotropic velocity models

for each stage. However, locating perforation shots using those models (assuming *SV* arrivals as isotropic *S*-wave) generated huge location errors (order of tens of meters). Hence, there was a need to develop a proper velocity model that will guarantee accurate locations of microseismic events.

A 5-layer VTI model was built in a three-step workflow using traveltimes of 13 available perforation shots spanning laterally from 250 to 600 m away from the sensor string (Fig. 4). The number and depths of the layers were chosen based on the geological information and the sonic log data (Fig. 31a). As a model benchmark I used Backus averaged (Backus 1962) well-log data from well L1 (averaging for $f = 200$ Hz using Seismic Unix) (Liner and Fei 2007), which is a reasonable upscaled approximation of a sonic log data (Maxwell et al. 2010; Bos et al. 2018). The benchmark model has an accuracy of 17 m of average mislocation. Locations were too deep for near offsets and too shallow for far offsets, although still more accurate than locations from isotropic models provided by the contractor. I was inverting for effective Thomsen's parameters and layer-dependent velocities. The free parameters were global e, g, and V_P0 and V_S0 for each layer. δ was kept fixed equal to 0.02 due to its stability in the well-log data (Fig. 31). The three-step workflow included:

1. Inverting for V_P0 and V_S0 of top four layers and Thomsen's ε;
2. Inverting for Thomsen's γ using extra traveltimes of microseismic events;
3. Estimating V_P0 and V_S0 of the bottom layer.

In the synthetic tests performed in Chapter 3 Neighborhood Search Algorithm (Sambridge 1999a) was used to find the minima during the inversion for the velocity model. However, the computational cost of the Neighborhood Algorithm became too heavy to be used with a dense, 1×1 m grid. Therefore, I have implemented a nested grid-search (Bentley 1975) scheme to be used instead. The parameter space was linearly sampled along each dimension to produce the

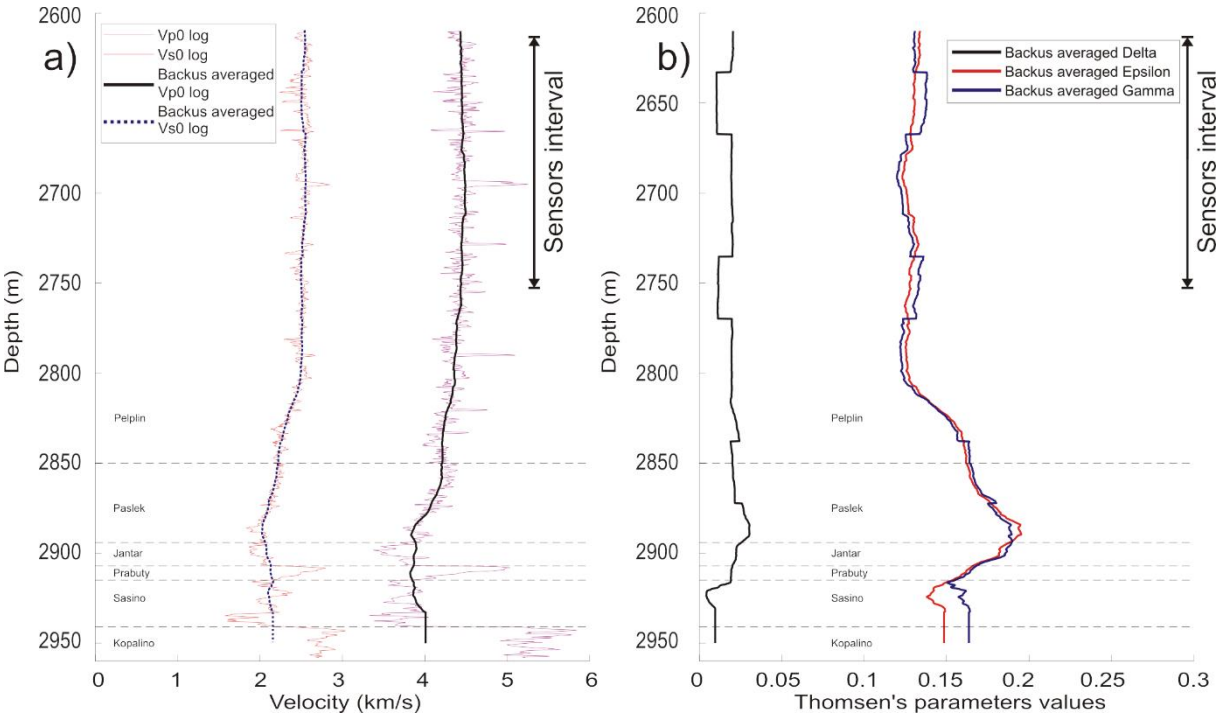

Fig. 31. Well-log data: formation tops – the dashed black lines, depth scale in True Vertical Depth (TVD) from Kelly Bushing (KB); (a) V_P0 from sonic log – the magenta line, V_S0 from sonic log – the orange line, Backus-averaged V_P0 – the black line, Backus-averaged V_S0 – the dashed blue line (Backus averaging for $f = 200$ Hz); (b) the solid lines are the Thomsen's parameters obtained through Backus averaging.

initial grid, which has been narrowed around the best solution after each iteration, then re-sampled and re-searched. Being aware of a trade-off between the accuracy of inverted parameters and computation time, in each subsequent iteration parameter space ranges were limited by 40%. This relatively slow convergence was meant to prevent the algorithm from falling into local minima.

4.2.1 Inverting for V_P0 and V_S0 of top four layers and Thomsen's ε

Due to the lack of *SH*-waves in the recorded wave field of the perforation shots (see Fig. 27), the inversion was run using *P*- and *SV*-waves onsets only. Under the weak anisotropy assumption (Thomsen 1986), Thomsen's γ is present only in the formula for the *SH*-wave velocity, which was not available in the perforation data. Hence, γ was skipped in the first step of the workflow and was inverted from the records of selected microseismic events afterward. Therefore, in the first step, I was inverting for V_P0 and V_S0 of each layer and ε. Hence, the objective function ζ, defined in Chapter 3 (Eq. (31)), was reduced by the *SH*-wave term, to a new form ζ' accounting for the differences between picks and modeled traveltimes of *P*- and *SV*-waves only, including time t_0 (Eq. (32)):

$$\zeta' = \sum_{j=1}^{p} \sqrt{\frac{\sum_{i=1}^{n}\left(\left(t_{\text{obs}}^{P,i,j} - t_{\text{cal}}^{P,i,j} + t_0\right)^2 + \left(t_{\text{obs}}^{SV,i,j} - t_{\text{cal}}^{SV,i,j} + t_0\right)^2\right)}{n}} \tag{32}$$

The obtained best-fitting parameters are listed in Table 8, while the resulting traveltimes comparison is presented in Fig. 32. Perforation shot locations will be discussed in detail after completing all 3 steps of the inversion procedure.

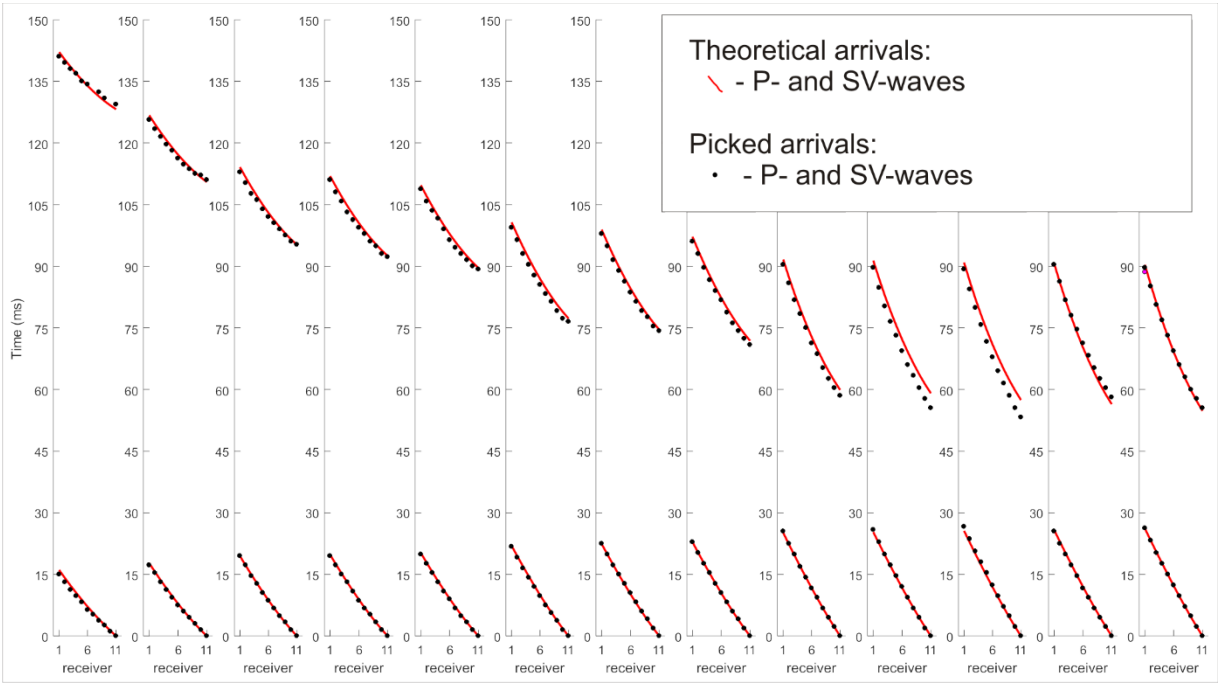

Fig. 32. Comparison of the observed and modeled best-fitted *P*- and *SV*-wave perforation shots traveltimes. For each perforation the RMS misfit is given at the top.

Table 8

The VTI model parameters obtained after 1st step of the inversion procedure

Layer	Top depth [m]	Thickness [m]	V_P0 [m/s]	V_S0 [m/s]	ϵ	δ
1	2615	274	4241	2423	0.15	0.02
2	2889	18	3938	1825		
3	2906	8	4492	1841		
4	2914	24	3677	1800		

4.2.2 Inverting for Thomsen's γ using extra traveltimes of microseismic events

Microseismic events tended to have clear *P*- and *SH*-waves onsets, whereas *SV*-wave onsets were appearing clear enough to be picked in less than half of the records of microseismic events only. Therefore, knowing that γ was crucial to obtain locations of the events because it is present in the *SH*-wave velocity formula (Thomsen 1986) I calculated its value using records of carefully chosen microseismic events (Gajek et al. 2018a). First, the event database was searched for the microseismic events having *P*- and *SV*-wave onsets most similar to the same onsets in perforation shots records. The criterion was the lowest RMS value of the picks differences. Similar moveout guarantees events locations to be close to the corresponding perforation shots locations, which are known. Hence, each perforation shot is supplemented with *SH*-wave onsets from microseismic event best matching *P*- and *SV*-wave onsets. Comparison of perforation shots and selected events is shown in Fig. 33.

Thanks to the rich population of events, the obtained fitting is acceptable except of the first, most distant perforation shot, which was therefore excluded from further γ calculation. Finding well-fitting onsets allowed to assume that the chosen event's hypocenter was at the

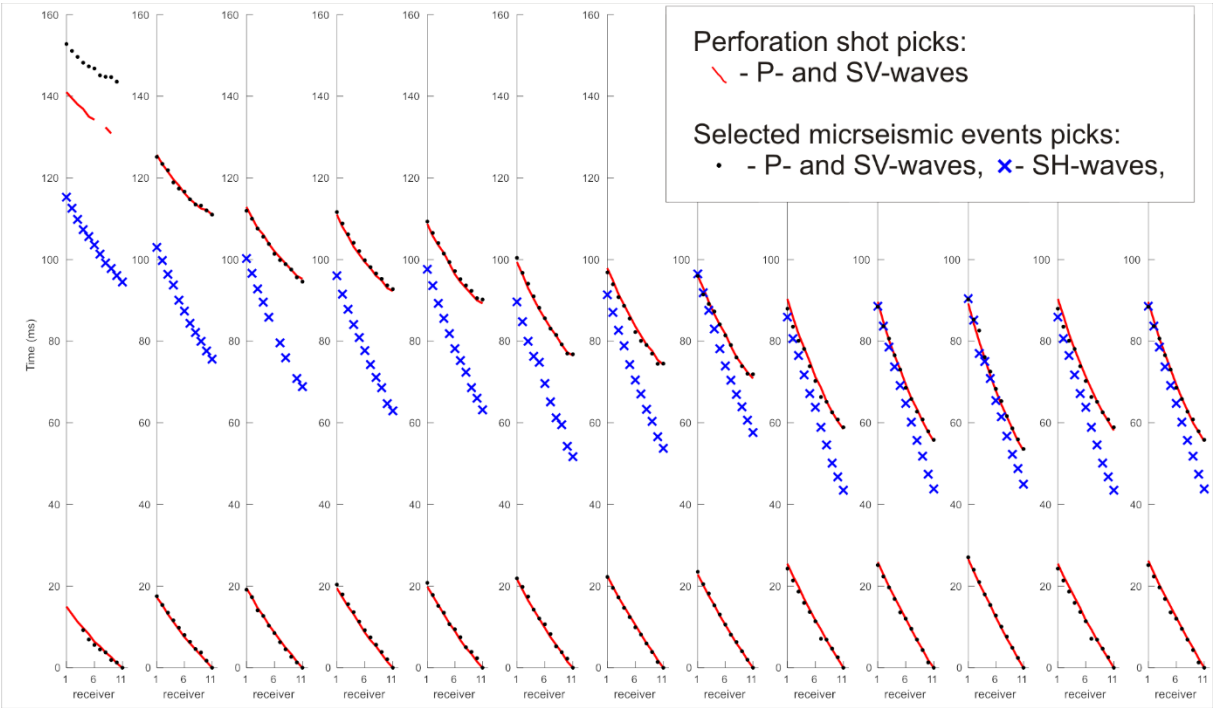

Fig. 33. Comparison of the perforation shots and selected matching event traveltimes. Note that the first pair was considered as an outlier.

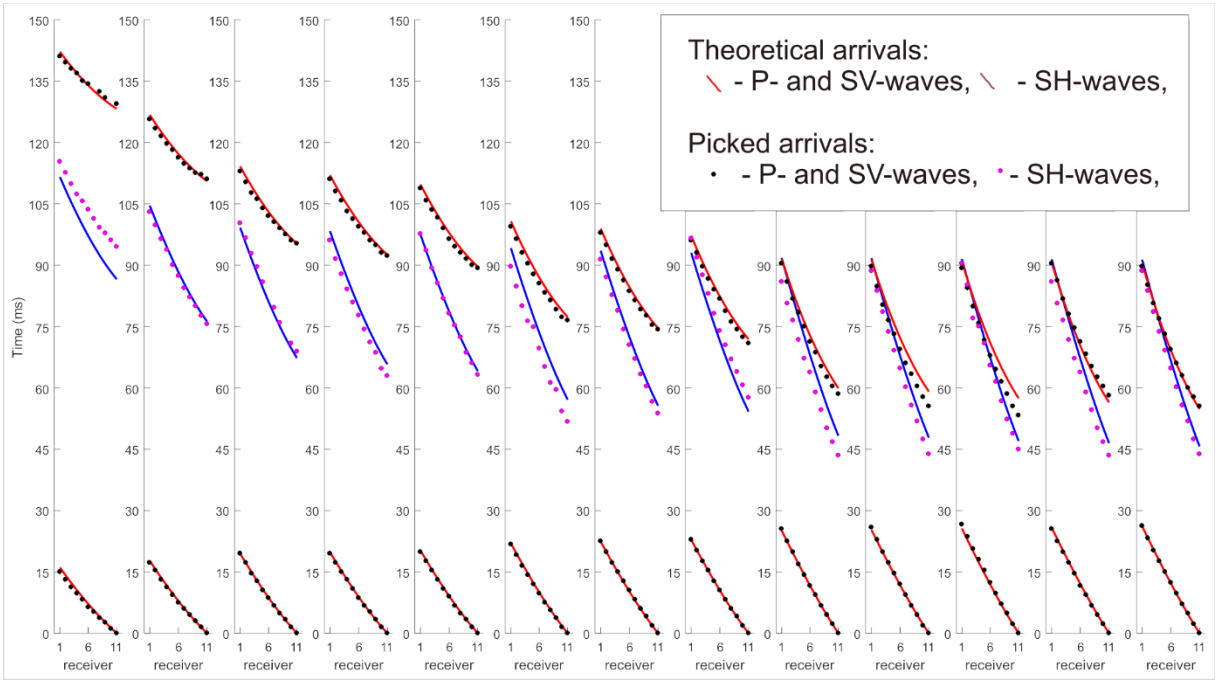

Fig. 34. Comparison of the observed and modeled best-fitted perforation shots and selected event moveouts. *P*- and *SV*-waves picks come from perforation shots records, *SH*-wave picks come from selected events records. For each perforation, the RMS misfit is given at the top.

perforation location; therefore, *SH*-waves that were not visible in the perforation shots should be expected with the same delays as for the matched events. Subsequently, I computed several velocity models for different values of γ, keeping other parameters fixed. By comparing the misfit of the observed delays, I determined that Thomsen's γ equal to 0.27 fits the data best.

The comparison of picked and modeled perforation shots traveltimes is shown in Fig. 34. Note that the first shot was not taken into account in γ inversion.

4.2.3 Estimating V_P0 and V_S0 of the bottom layer

Velocities for the base of the stimulated Sasino formation, i.e., the fast limestone Kopalino layer, were impossible to obtain using perforation shots due to the lack of distinguishable refracted waves in the recorded wave field, meaning there is no information about this layer in the records. When trying to invert at once for all five layers, the Kopalino velocities were marginalized towards low velocities, not contributing to the shape of the moveouts. Nevertheless, this layer still plays a role in the procedure of microseismic events location, since some of them can originate from below the perforation shots locations or even from the Kopalino formation.

Another source of information on the velocities is the sonic well log. However, when comparing inverted velocities from the above layers with well log data, I observed that the latter were higher (Fig. 35), following the velocity dispersion theory (Winkler 1986), so they cannot be directly assigned to the model. Indeed, traveltime modeling with V_P0 and V_S0 values from Backus-averaged well logs caused refraction at the distant perforation shot location, which does not agree with observed moveouts. Hence, I kept on lowering the bottom layer velocities as long as the direct waves became the first arrivals. The velocities of the bottommost layer were finally identified as $V_P0 = 5200$ m/s and $V_S0 = 2730$ m/s. The third step finalized the VTI velocity model building procedure.

4.2.4 The final model

The three-step workflow resulted in the complete set of parameters required to describe the 5-layer VTI velocity model despite challenging limitations in the data. The exact values of inverted parameters are listed in Table 9. The comparison of derived model parameters with the benchmark Backus-averaged model is presented in Fig. 35.

Table 9

The final VTI model parameters obtained after complete inversion procedure

Layer	Top depth [m]	Thickness [m]	V_P0 [m/s]	V_S0 [m/s]	ϵ	δ	γ
1	2615	274	4241	2423	0.15	0.02	0.27
2	2889	18	3938	1825			
3	2906	8	4492	1841			
4	2914	24	3677	1800			
5	2938	62+	5200	2730			

Note: 5th layer had no lower bound and was limited by range of microseismic events, afterwards.

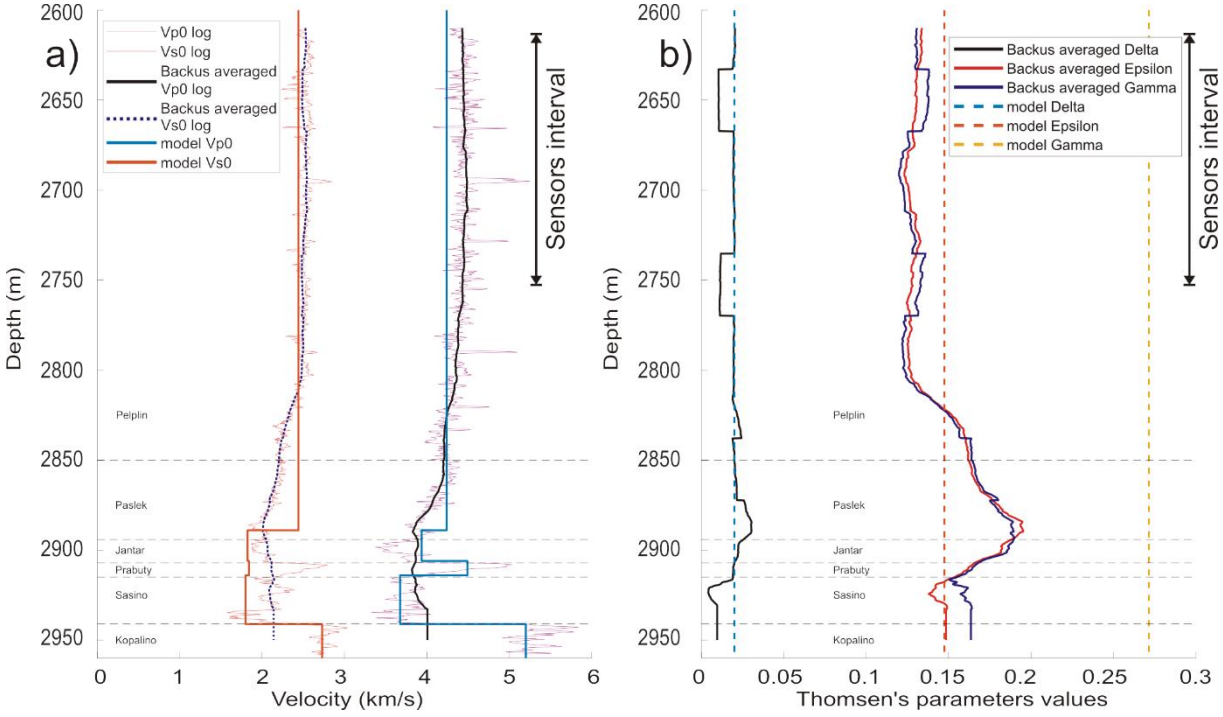

Fig. 35. Well-log data and estimated velocity model parameters for the L1 well: formation tops – the dashed black lines, depth scale in TVD from KB; (a) V_P0 from sonic log – the magenta line, V_S0 from sonic log – the orange line, Backus-averaged V_P0 – the black line, Backus-averaged V_S0 – the dashed blue line (Backus averaging for f = 200 Hz), estimated V_P0 – the light blue line, estimated V_S0 – the red line, and (b) the solid lines are the Thomsen's parameters obtained through Backus averaging; the Thomsen's parameters derived from inversion are shown as the dashed lines.

The inverted model results in accurate locations of perforation shots in offset-depth cross-section are shown in Fig. 36 (the offset-azimuth errors will be addressed in the subsequent section). The average mislocation equals 7 m (average mislocation of the benchmark model was 17 m) and is affected mostly by inaccuracy in offset plane (Fig. 37).

The RMS of inverted model misfit equals 2.4 ms for all three onsets (perforation shots and matched events) and 1.3 ms when considering only *P* and *SV* only (perforation shots only), whereas picking uncertainty for strong perforation shots was assumed to be 0.375 ms (one sam-

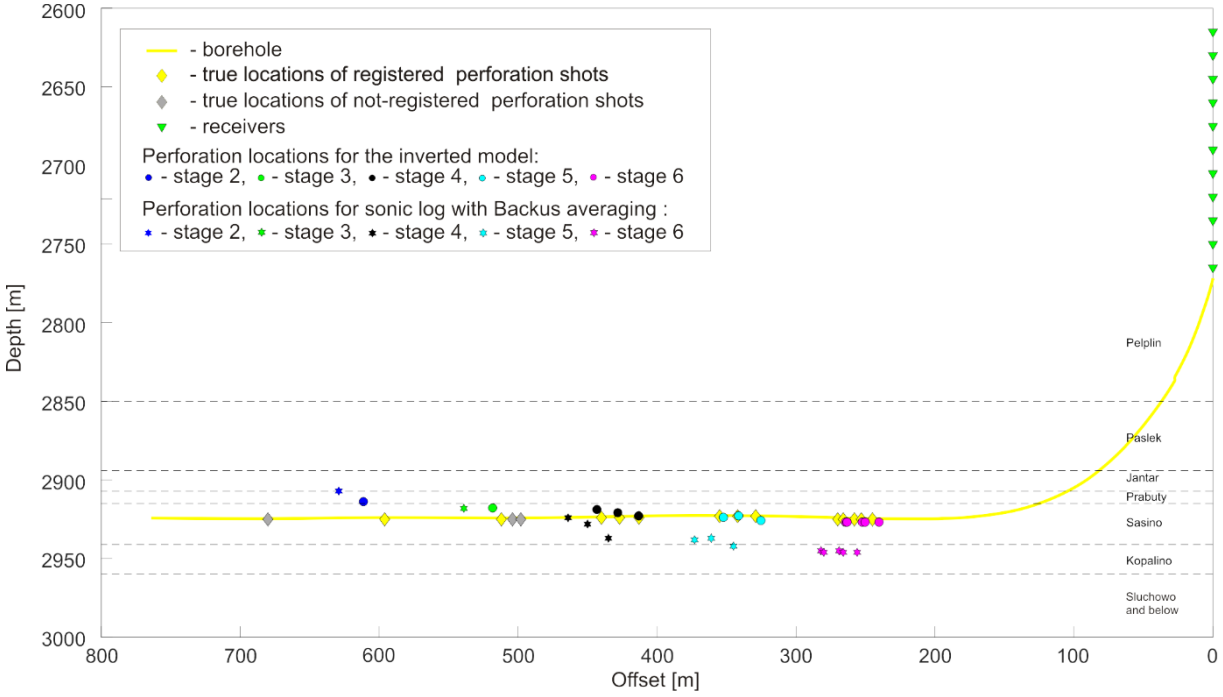

Fig. 36. Perforation shot locations in a vertical cross-section aligned with borehole trajectory. The true locations of all 13 recorded perforations are marked with the yellow diamonds, not-recorded are marked with the gray diamonds. Here, 13 perforation shot locations in the Backus-averaged benchmark model are marked with stage-colored stars. Perforation shot locations in the best obtained model are marked with stage-colored circles, depth scale in TVD from KB.

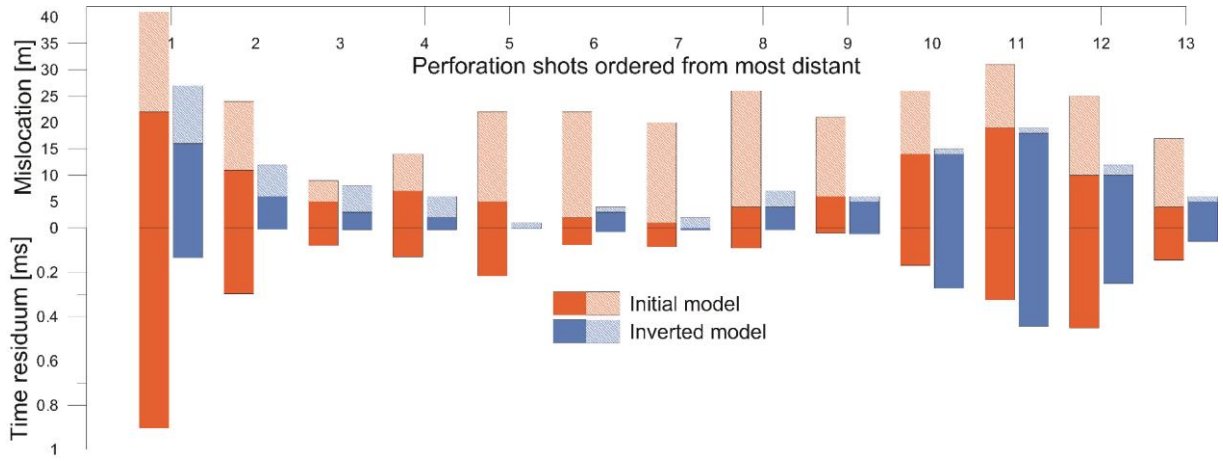

Fig. 37. Comparison of mislocations (upwards pointing axis) and time residuals (downwards pointing axis) between the initial Backus-averaged model (marked in orange) and the final inverted (marked in blue) velocity models. In the mislocation section, the dark bars represent the horizontal component of the location error and the light bars represent the vertical component of the location error.

ple). The comparison between the recorded and modeled moveouts using the final velocity model is shown in Fig. 34 and reveals a very good match for the *P* and *SV* onsets, whereas the *SH*-waves are less-accurately fit, especially for the most distant perforations. This is related to the slightly different location of the microseismic event used for γ calibration.

The surprising disproportion between inverted γ value and value from sonic logs is most probably due to the scale-effect. A vast difference in the frequency content of seismic waves and acoustic logger makes those two methods sensible to different features of the rock, and lower frequencies are prone to see bigger cracks.

4.2.5 Locating the perforation shots in horizontal plane

For a complete inspection of microseismic events location accuracy, also an insight into the perforation shot locations in the offset-azimuth plane is necessary. Even though this subsection does not contribute to the VTI velocity model building, it is added here for completeness.

Location in a horizontal plane is a combination of two independent inputs. First is an offset that changes with different velocity models (already visible in Fig. 36). Second is an azimuth towards the event estimated using a back-azimuth tracking procedure, not dependent on the velocity model. Obtained locations in horizontal plane are presented in Fig. 38.

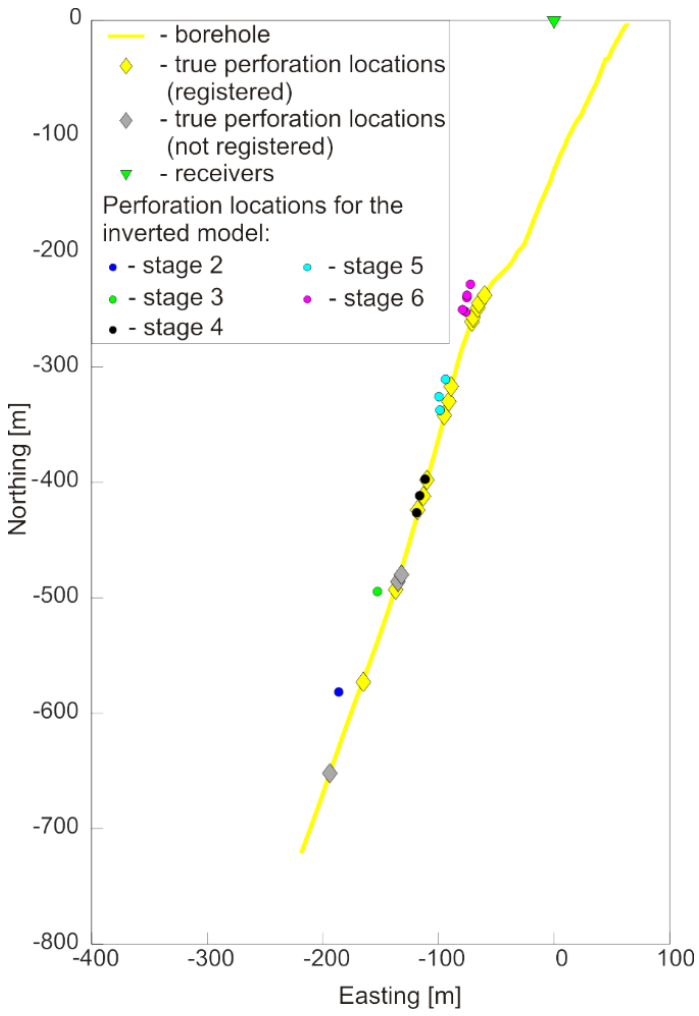

Fig. 38. A map view of stage-colored perforation shot locations in the best obtained model are marked with stage-colored circles. The true locations of all 13 recorded perforations are marked with the yellow diamonds, not-recorded are marked with the gray diamonds.

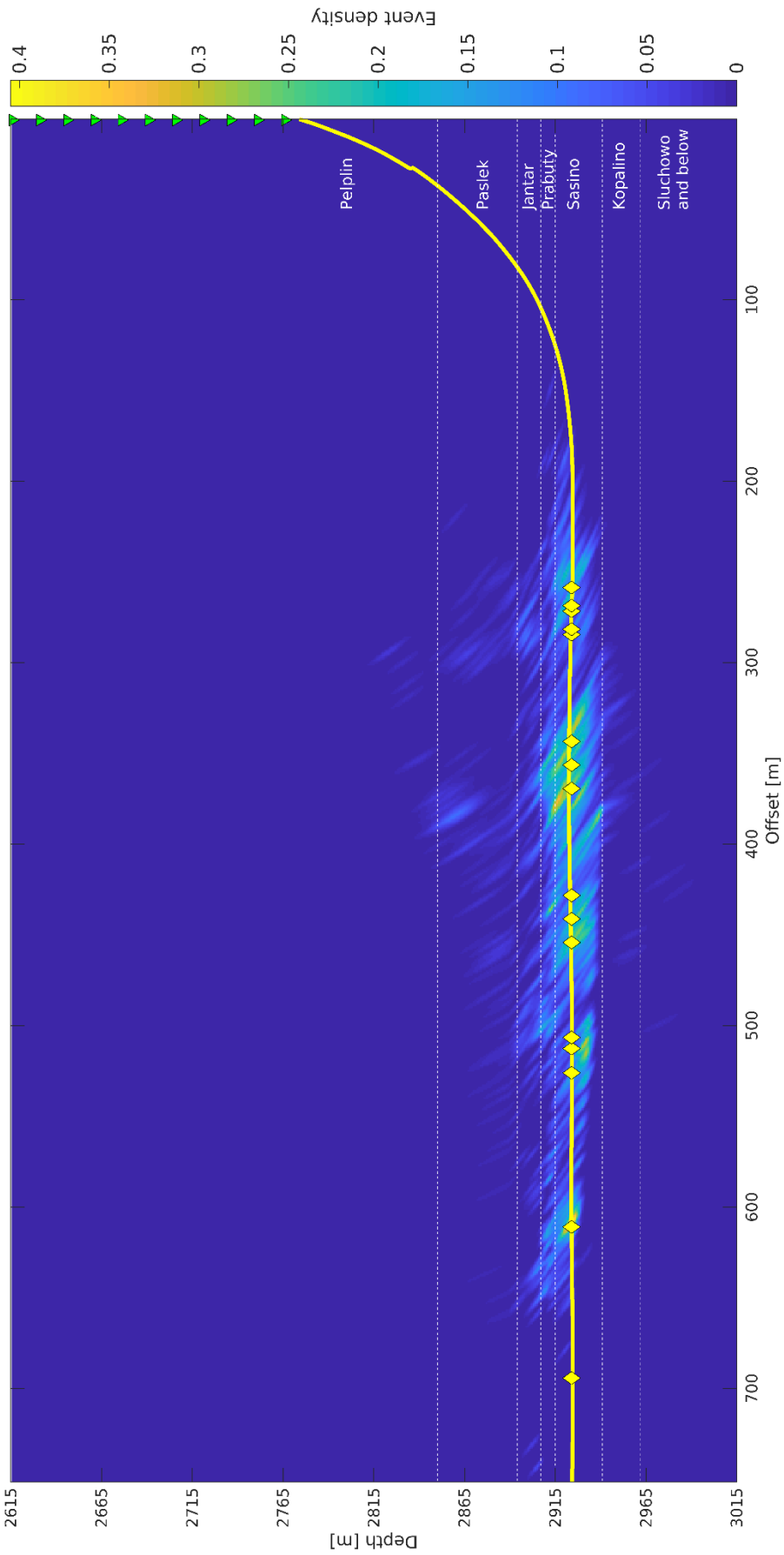

Fig. 39. Marginal probability density of microseismic events locations in the vertical plane aligned with the borehole trajectory, depth scale in TVD from KB. The color scale of an event density provides a probability of on of 1385 events occurring at given coordinates. The borehole projection – yellow solid line; perforation shots locations – yellow diamonds; receivers locations – green triangles; stratigraphic units intervals – white dashed lines.

4.3 Locating the microseismic events

As a rule, the velocity model calibrated with perforation shots guarantees accurate microseismic events locations in the area of model space where calibration was done. However, because of the imperfect inversion solution, the locations will become less and less precise when moving away from the calibrated areas. In this case, all available events of known locations were used for model calibration to ensure the highest precision.

My model space for events location was limited to 800 m offset and 400 m in depth (from the top receiver depth at 2615 to 3015 m). The best-resolved space within the model was the area between offsets 250 and 600 m (stages 2 to 6) and limited in depth to the borehole vicinity. Therefore, very deep or shallow located events, and events on far offsets from stages 2 and 3, should be considered as least precise due to limited calibration data. However, most events were expected to occur close to the densely perforated borehole intervals.

The microseismic events were already detected and picked, hence they were ready to be located. For the purpose of probabilistic events location, Eq. (28) was used. I assumed the picking uncertainty for all events to be 3 samples (1.125 ms), which was 3 times more than for perforation shots. The obtained anisotropic velocity model was used to locate all the identified microseismic events. Even though more than 1400 events were located, some of them have to be discarded, because of having unrealistic locations (e.g., too shallow) or poorly resolved, off-the-borehole azimuths. Finally, 1385 events were kept as a final catalog. Figure 39 shows summed location probability density of all events in vertical cross-section and Fig. 40 as a map view.

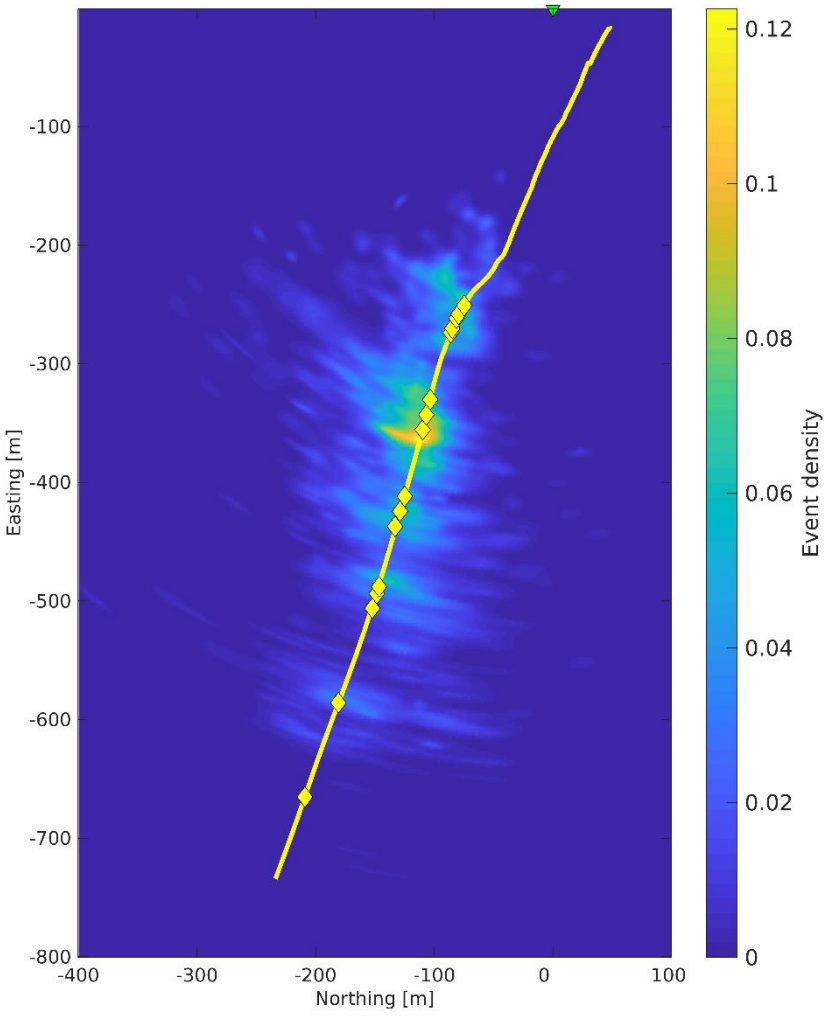

Fig. 40. A map view of marginal probability density of microseismic events locations together with the borehole trajectory. The color scale of an event density provides a probability of one of 1385 events occurring at given coordinates. The borehole projection – yellow solid line; perforation shots locations – yellow diamonds; receivers location – green triangle.

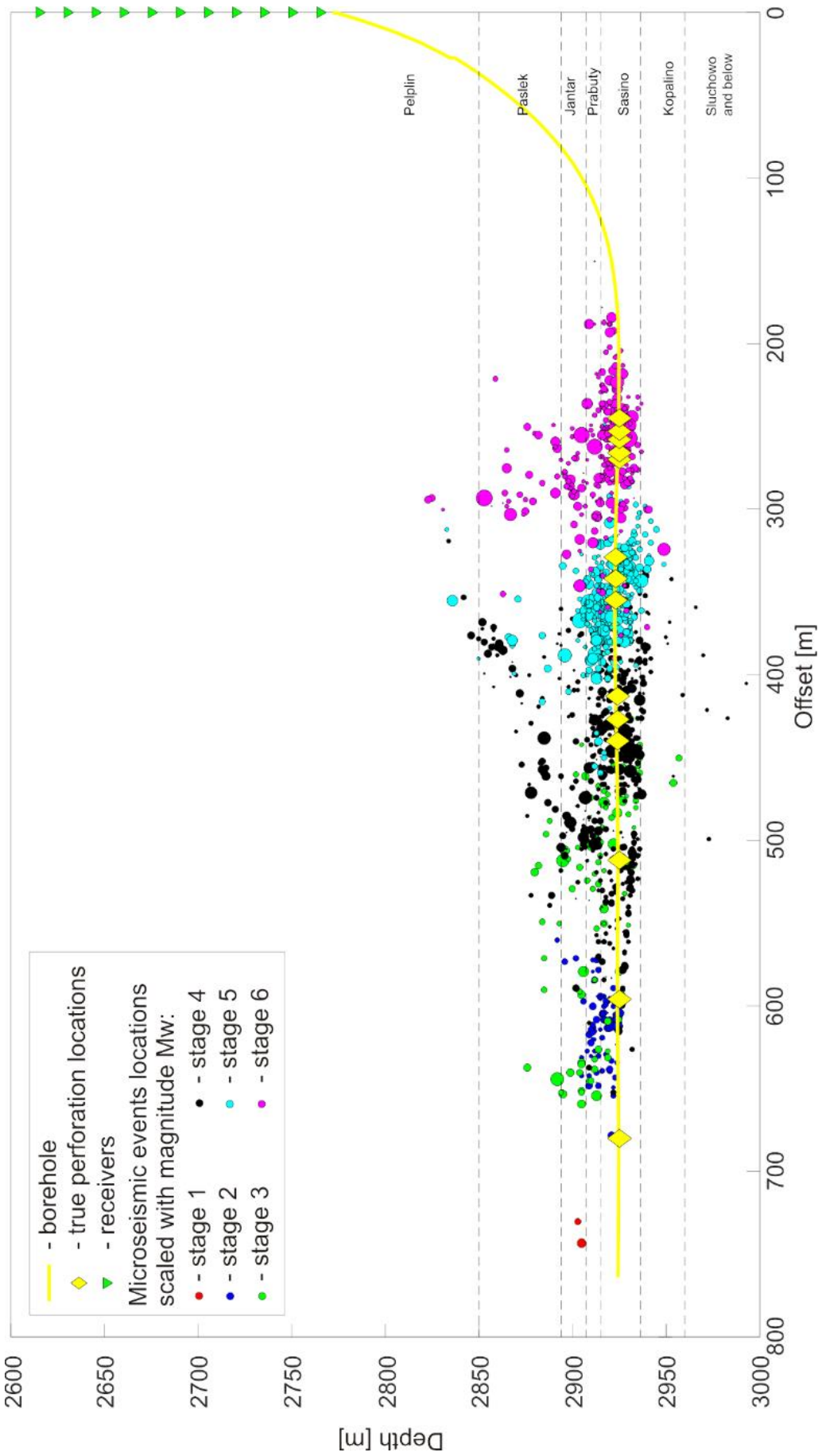

Fig. 41. Locations of stage-colored microseismic events scaled by M_w spanning from −3.6 to −2.0 in the vertical cross section aligned with the borehole trajectory. Depth scale in TVD from KB.

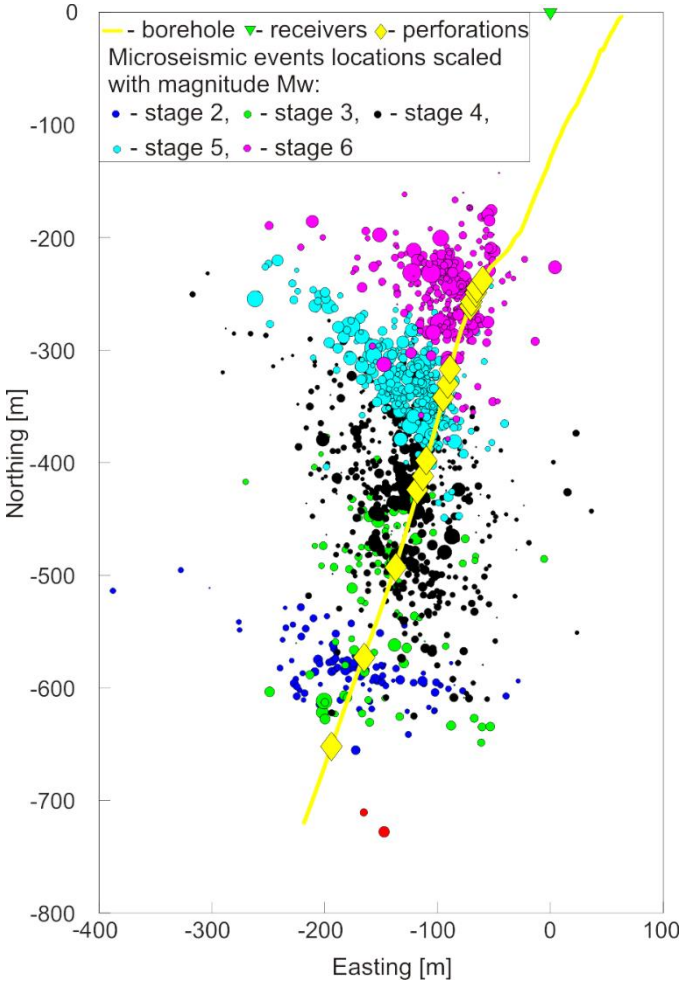

Fig. 42. A map view of stage-colored locations of microseismic events scaled by M_w spanning from –3.6 to –2.0 together with the borehole trajectory.

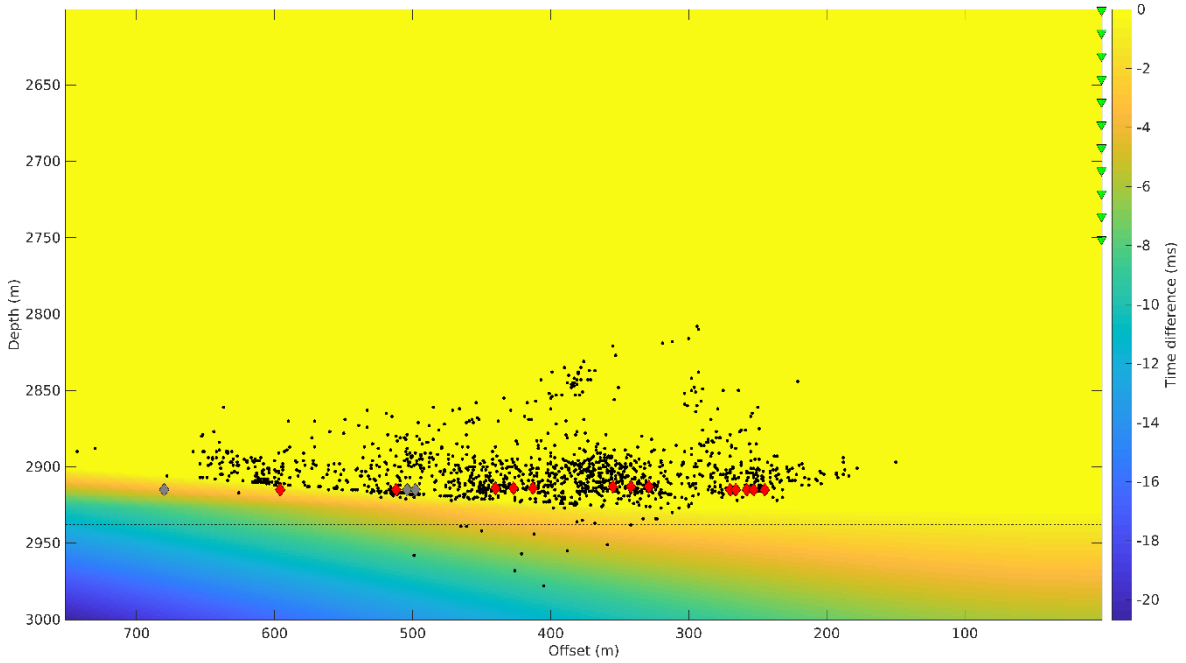

Fig. 43. Map of *P*-wave traveltime difference between the final velocity model (including fast velocity Kopalino layer) and 4-layer model without it for the deepest receiver. The perforation shots used in the inversion are marked in red diamonds, not used perforation shots are marked in gray diamonds, microseismic events located using the final model are marked with black dots, receivers are marked with green triangles. A black dotted line marks the top of the fast Kopalino layer.

Maps of the probability density of a single event location can be easily transformed into a single point by finding the maximum value of the probability density. Such an approach gives a clearer image and allows to scale the dots, still keeping the original information about location uncertainty. The vertical locations scaled by moment magnitude M_w to emphasize dynamics of the stimulation are shown in Fig. 41, the horizontal locations are shown in Fig. 42.

The sharp cut-off in the event locations with an upgoing trend is observed in the vertical cross-section in the toe part of the well (Figs. 41 and 39). This is a clear indicator of the refraction regime caused by the fast, lowermost Kopalino layer. The area of the inverted Kopalino layer refraction regime extent is shown in Fig. 43 in the form of traveltime difference map. It might seem unrealistic; however, in the absence of the farthest jet perforation signal in the recorded wave field, no other data can provide additional constraints for lowering the basement velocity more than was already done. In general, using jet perforations instead of conventional shots within the peripheral stages limits the ray coverage of available shots significantly and hinders the process of accurate velocity model inversion.

4.4 Evaluation of the stimulation performance

The stress direction was determined for both, the stimulated and monitoring boreholes, at the borehole section located approximately 1000 m above the stimulated complex. The measured NNW-SSE maximum horizontal stress direction (SH_{max}) (Bobek and Jarosiński 2018) is similar to the regional trend in this part of the Baltic Basin (Jarosiński 2006). When compared with the elongation of the Microseismic Volumes (MVs) of individual stages, it is clear that they are not parallel to SH_{max}, as in the most typical instances. In such a case, pre-existing faults and fractures are expected to control the stimulation zone. Based on borehole cores and geophysical logging data it is known (Bobek and Jarosiński 2018) that fracture system consists of two main joint sub-vertical fracture sets of regional extent, J1 and J2, striking respectively in the azimuth 20° and 125° (Fig. 44a). Additionally, two diagonal sets, J′ and J″, striking in the azimuth 80° and 170°, are distinguished in the monitoring borehole. These fracture sets are not uniformly distributed among lithological formations (Fig. 44b). The J2 set prevails in the Sasino Fm which hosts the horizontal borehole segment. It also dominates the results of *S*-wave splitting measurement inversion presented in the next chapter, while the J1 set is more pronounced in the Jantar formation. The Prabuty, Kopalino, and lower part of the Paslek formations almost lack open fractures; therefore, they have the potential to create mechanical barriers. There is also some evidence for transitional stress regime between strike-slip and normal faulting and for low differential stress level in a range of 10 MPa (Bobek et al. 2017). The shape and range of individual microseismic clouds varies significantly among stages.

In the first unsuccessful stage, a minor stimulation effect was achieved. Locations of the seismic events 10 m over the top of Sasino formation should be accounted for as velocity model inaccuracy (visible in Fig. 36). The number of microseismic events with satisfactory S/N is insufficient to determine the MV. Also, the Stage 2 of stimulation, in which 139 m^3 of fluid was used, was not completed. The elongated axis of microseismic events cloud is oblique to the trend of SH_{max}, but consistent with a mean direction between the J2 and J′, two main tectonic fracture sets in the Sasino formation. It suggests reactivation of the pre-existing fractures as a main effect of stimulation. In the vertical section, the compact cloud of the microseismic events ranges by 20 m, similarly to the thickness of the Sasino formation. From the top and the bottom, this formation is bounded by mechanical barriers with absence or scarce tectonic fractures.

In the Stage 3, after injection of 416 m^3 fluid, the MV consists of two compact clouds of events. The first, dispersed and circular in the horizontal plane, 120 m in diameter, is located directly near the perforation cluster. The second covers the elongated MV from the Stage 2.

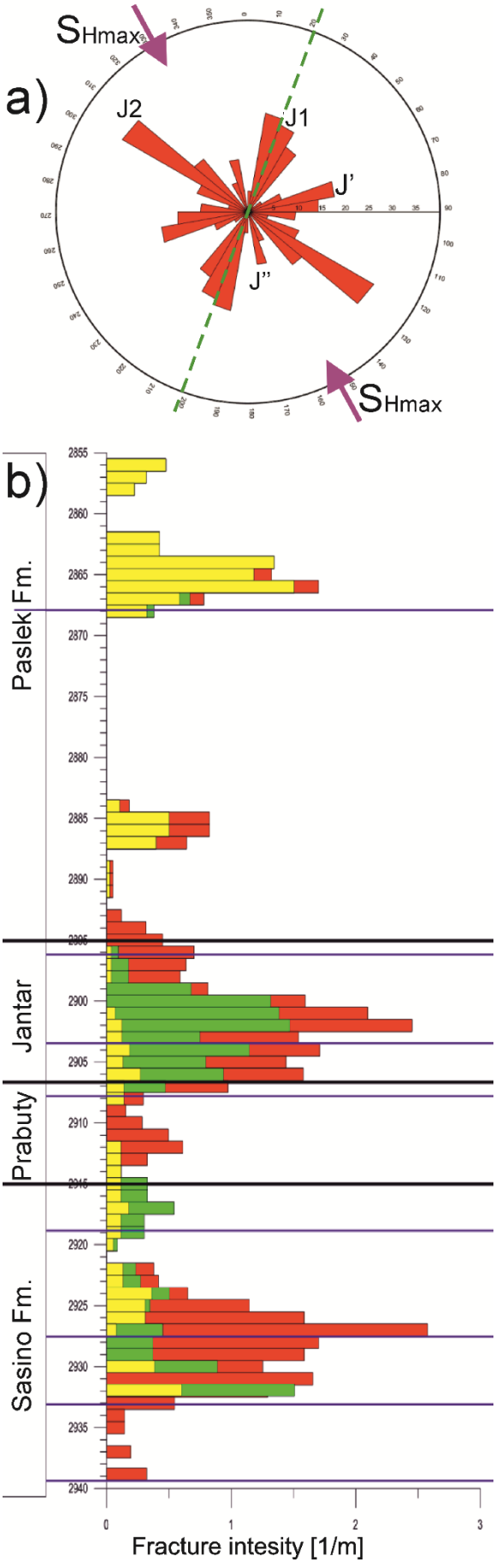

Fig. 44. (a) Orientation of the sub-vertical fracture sets (joints) in the monitoring borehole and the present-day maximum horizontal stress direction (SH_{max}). The green dashed line points to the direction of the stimulated borehole horizontal segment, and (b) fracture intensity profile for the monitoring borehole. Depth scale in TVD from KB. The formation is separated with the thick black lines. The J1 fracture set is marked in green, J2 in red, and in yellow. The lower Kopalino formation J′ + J″ with a complete lack of fractures is not shown.

Such distribution points to the lack of preferred direction of newly stimulated fractures and to the leakage of the fluid into the previously stimulated zones. The vertical range of compact circular cloud reached 40 m, similar to the thickness of the reservoir that comprises both Sasino and Jantar prospective formations. In this case, the weak mechanical barrier of Prabuty formation was broken by increased volume and pressure of the fluid. Similarly to the Stage 2, the tilted bottom of the MV below the perforations is influenced by the refraction regime of the Kopalino layer.

In the Stage 4, the volume of fracturing fluid increased to 820 m^3. The 400 m long cloud of microseismic events is elongated in the direction parallel to the SH_{max}. However, the MV could be again split into two parts: one adjacent to perforation and one covering the MV of the Stage 3. Events propagate in time towards the Stage 3. In the vertical view, initial events stay within the prospective complex of the Sasino and Jantar formations, but then progress up to the upper Paslek formation, which acted as a barrier in the previous stages. Also, a few weak events were located in the Kopalino formation, however not enough to consider that barrier as broken. The bottom layer refraction regime still slightly influences the events' locations towards the toe part of the well, however toward the heel part events start to occur below the top of Kopalino.

In the Stage 5 of stimulation, the injection of 869 m^3 of fluid developed elongated and asymmetric MV. Its 300 m long axis is parallel to the strike of J2 fracture set and the trend of nearby fault visible in 3D seismic data (Kowalski et al. 2014; Cyz and Malinowski 2018). Judging from the microseismic events appearance over time, stimulation started with the development of hydraulic fractures in the direction of the SH_{max} in the near-borehole zone, then continued in the direction of the pre-existing tectonic fractures and probably small-scale faults. In the vertical view, the range of MV is similar to the previous stage, with the individual events located in both, Paslek and Kopalino formations. The influence of Kopalino refraction regime is no longer visible.

In the Stage 6, the injection of 664 m^3 of fluid caused similar effects as in the Stage 5 with some minor differences that might result from lower fluid volume. In horizontal projection, the cloud of microseismic events is almost circular with the longer axis span less than 200 m, while the vertical extent is similar to the Stage 5.

The obtained locations of microseismic events create a relatively complex but comprehensive pattern that, in general, might be explained by natural factors. The elongation of the MVs is mostly controlled by the J2 fracture set, which dominates in the Sasino formation and only to a small extent influenced by horizontal stress direction. A high degree of MV penetration towards the previous stages is explained by an oblique angle between the borehole and SH_{max} direction (approx. 40°) enhanced by the trend of the reactivated J1 fracture set, parallel to the direction of the horizontal borehole segment. In turn, the successive rise of the MV in vertical plane among stages can be explained by the stress shadowing effect in the most intensively stimulated formations (Warpinski and Branagan 1989; Zangeneh et al. 2015) and escape of the fracturing fluid to the more relaxed Jantar and Paslek formations. The systematic rise of the bottom of MV in the stages that are most distant from the monitoring borehole should be explained only by increasing the influence of the fast bottom layer refraction regime.

4.5 Conclusions from this chapter

In this chapter, I presented a complete workflow spanning from very initial data processing using self-developed tools up to microseismic events mapping and providing the interpretation of the treatment performance.

The most important part of my work in this chapter is an inversion of the VTI anisotropic velocity model using limited data. Due to the absence of *SH*-wave onsets, it was impossible to

retrieve Thomsen's γ from the perforation shots records. Thus, I used the *SH*-waves of microseismic events located close to the perforations and retrieved γ from the *SH*-*SV*-wave delay time. Finally, the successful inversion provided much more accurate perforation shot locations (with mean RMS of mislocations only 7 m) than isotropic and Backus-averaged models, and hence, allowed for the reliable location of microseismic events. The accurate locations allow drawing conclusions about the evolution of fractures in the reservoir during the hydraulic stimulation. The most important observations are:

- most of the recorded microseismic events occur within the 40 m thick prospective complex of the Sasino and Jantar formations meaning that the thin Prabuty formation was being predominantly broken;
- microseismic events tend to migrate into previously fractured intervals during the ongoing stimulation;
- the Paslek formation was acting as a barrier in the initial stages of the treatment while has been probably broken during the final 4, 5, and 6 stages;
- the Kopalino formation acts as a barrier for injected fluids throughout the whole treatment;
- the J2 fracture set in the Sasino formation acts as a key factor in the stimulated fracture propagation and influences the fracture openings more than the maximum horizontal stress direction.

5. ESTIMATING FRACTURE PARAMETERS BASED ON SHEAR-WAVE SPLITTING

This chapter presents research conducted on the same data set from the microseismic monitoring campaign performed during hydraulic stimulation in Lubocino 2H well. The experiment geometry, geological setting, and data availability were described in the Introduction section. The theory and details of used methods were described in Chapters 2 and 3. This chapter is an elaborated version of Gajek et al. (2018c).

5.1 Data and SWS measurements

Most of the recorded events had clear, strong *SH*-wave arrivals, and weaker *P*-wave arrivals[3]. SWS was visible on the majority of records – at least 1/3 of 1385 microseismic events had clear *SV*-wave onsets. The anisotropy is manifested by a significant, stagevarying *S*-wave splitting (up to 40 ms for some of the events), necessitating the use of an anisotropic velocity model for the purpose of the microseismic event location. Example waveforms with both strong and weak SWS are shown in Fig. 45. A 1D, 5-layer VTI model was built using traveltimes inversion of 13 perforation shots and selected microseismic events. Detected events were then located using an inverted VTI velocity model and probabilistic location approach (see Chapter 4).

SWS measurements provide the polarization (φ) of the fast shear-wave and the time delay (*dt*) between the two split shear modes (Wolfe and Silver 1998; Teanby et al. 2004). A measurement can be made for each source-receiver pair, resulting in a considerable amount of data when geophone array is used to record hundreds of events. To deal with a large number of measurements, I used the automated method described by Wuestefeld et al. (2010), which is based in turn on that described by Teanby et al. (2004).

The workflow for a single measurement is presented in Fig. 46. Waveforms recorded by a 3C sensor are rotated to the ray-frame coordinates (i.e., radial, transverse, vertical) in order to minimize *P*-wave energy on the *SH* and *SV* components. Next, the SWS correction is applied,

[3]For brevity, the qualifiers in "quasi *P*-wave" and "quasi *S*-waves" are omitted.

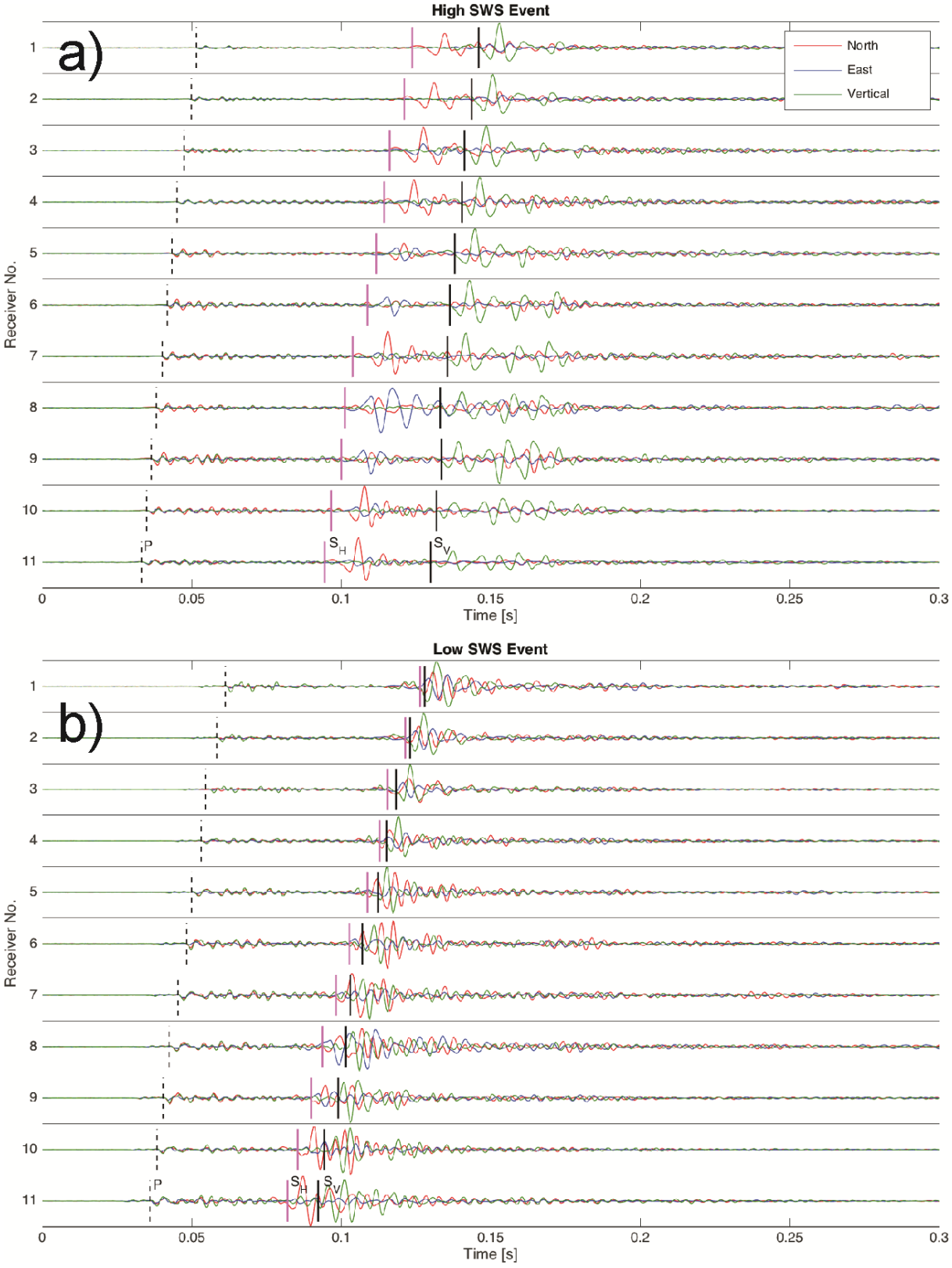

Fig. 45. Waveforms from example microseismic events recorded by the 11 3C geophones. (a) An event with strong SWS, producing significant time delays (19–37 ms) between fast and slow *S*-waves. The event is located 450 m from the monitoring array. (b) An event with smaller amounts of SWS. The event is located 305 m from the monitoring array. Picks are labeled on bottom traces.

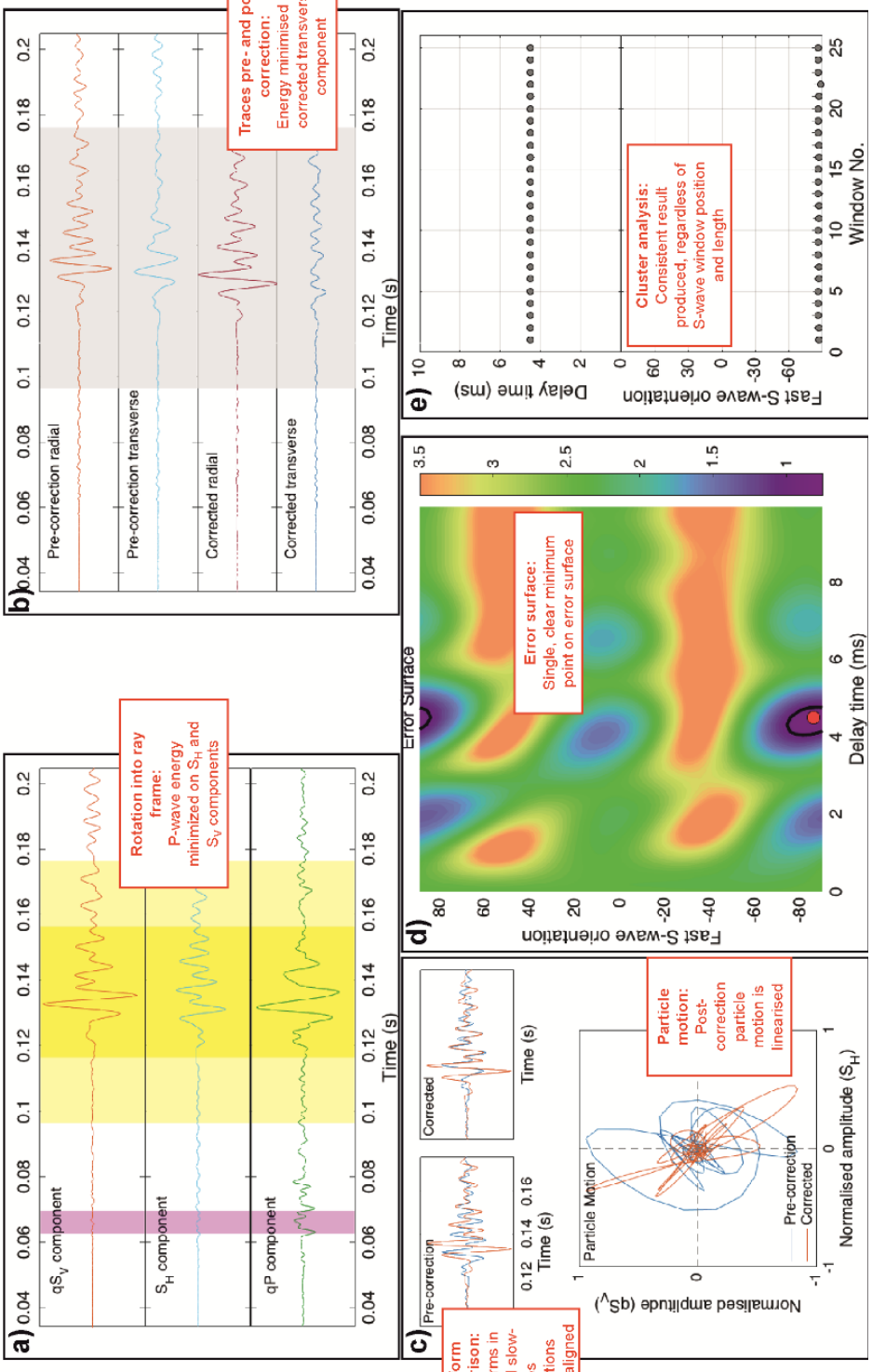

Fig. 46. Example SWS result, showing the QC criteria used to assess the measurements. In (a) I plot the recorded waveforms in the ray-frame coordinates: An effective rotation will ensure that *P*-wave energy is minimized on the *SH* and *SV* components. In (b) I plot the radial and transverse components prior to and after the SWS correction has been applied: the SWS correction should minimize energy on the transverse component. In (c) I plot the S-wave arrivals in the SWS fast- and slow-orientation coordinates, and the pre- and post-correction particle motion (a superposition of components plotted in (b) restricted to the longest analysis window length): after correction, two matching waveforms should be found, resulting in a linearization of the particle motion. In (d) I plot the error surface of the correction method as a function of delay time and fast direction, normalized such that the 95% confidence interval (highlighted in bold) is valued one: a single, clear minimum point should be produced. In (e) I compare SWS results produced by altering the analysis windows within the light- and dark-yellow bands of (a). A good result should be consistent regardless of the choice of the analysis window.

resulting in linearization of the particle motion in a fastand slow-axes coordinate system (Fig. 46c). The SWS correction is determined by applying all possible fast *S*-wave orientations and time shifts and then retrieving the minimum error solution from a resulting error surface (Fig. 46d). The analysis is performed for various-length *S*-wave windows to provide a stable solution regardless of the window position and length (Fig. 46e). A more detailed description of this workflow is described in Fig. 46 caption. To ensure good data quality, the acceptance criteria defined by Teanby et al. (2004) were used to ensure that only robust SWS measurements were taken forward for further analysis, including:

1) good event signal-to-noise ratio;
2) linear P-wave motion allowing a well-constrained rotation from geographical (NE- Z) to ray-frame (P-SH-SV) coordinate system;
3) effective minimization of energy on the transverse component after the SWS correction has been applied, resulting in linear post-correction particle motion, and matching post-correction waveforms in a fast- and slow-S-wave coordinate system;
4) a single, tightly constrained minimum in the error surface;
5) consistent SWS results regardless of the choice of the analysis window start time and length.

A high-quality result must fulfill all of these conditions. These criteria were first assessed automatically by discarding results which evidently neglected any of these conditions. Then the remaining SWS measurements were assessed manually via the inspection of plots such as the one shown in Fig. 46.

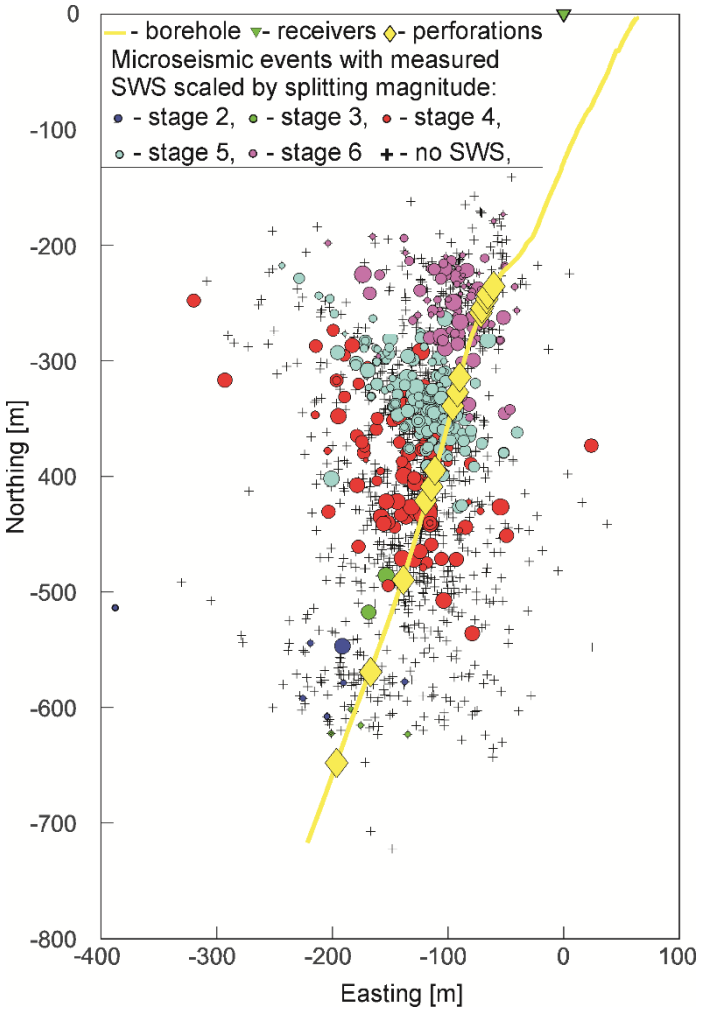

Fig. 47. A map view of stage-colored microseismic events locations with at least one good-quality SWS measurement, scaled by the splitting magnitude. Other microseismic events are marked as black plus signs at the background.

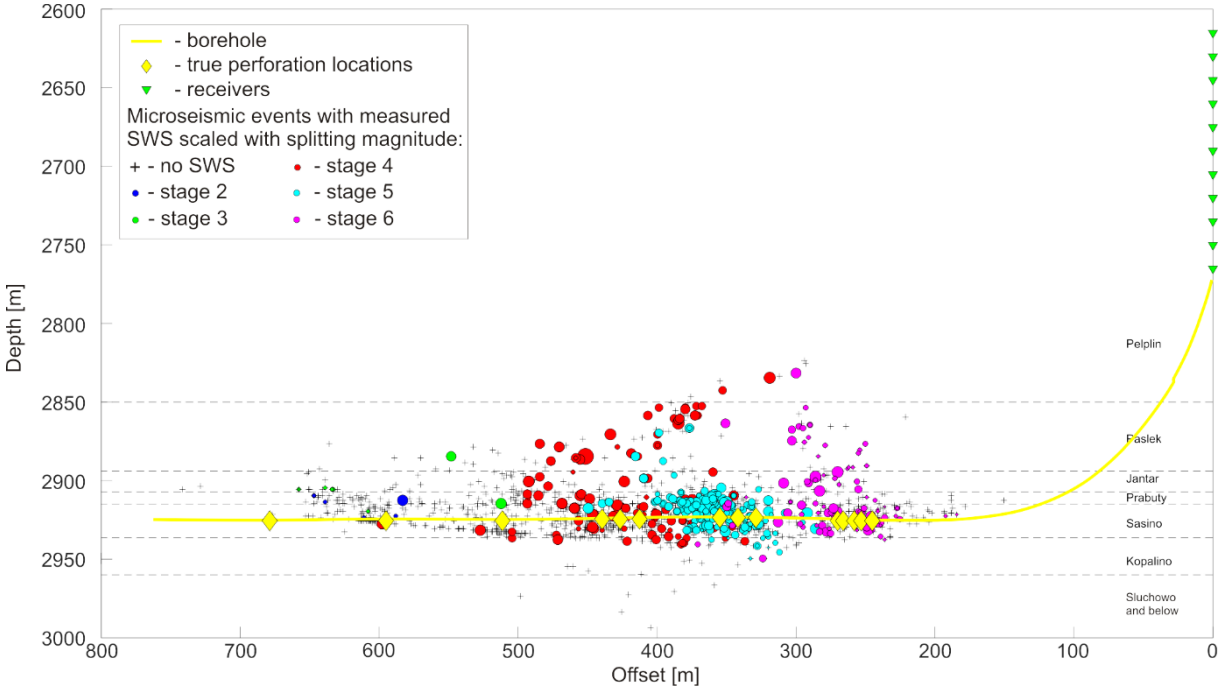

Fig. 48. Locations of stage-colored microseismic events with at least one good-quality SWS measurement, scaled by the splitting magnitude. Other microseismic events are marked as black plus signs at the background. Cross section along the borehole trajectory. Primary and secondary target intervals with enhanced TOC concentration are Sasino and Jantar, respectively.

Out of more than 14 000 SWS measurements (all registered events on each receiver), 561 were accepted as high-quality results under our strict acceptance criteria. The spatial distribution of microseismic events with a high-quality measurement on at least one trace is plotted in Fig. 47 in map view and in Fig. 48 in a side view. Significant noise level restricted the number of good measurements, especially for distant stages: only 4% of accepted measurements belong to stages 1–3 (the most distant from the observation well). The accepted measurements had approximately 35° wide azimuthal coverage and 35°–70° incidence angle coverage (Fig. 49a,b). Most fast *S*-wave polarization angles are at 90° relative to the *SV* orientation; i.e., they are near-horizontal, as expected from a VTI system. However, significant numbers of events do not have horizontal fast *S*-wave polarizations, and indeed the delay times for these events are often larger than the delay times for those with horizontal polarizations (Fig. 49c). These observations imply that the system is not solely VTI. Instead, such a signature can be recognized as VTI fabric influenced by vertical fractures (Usher et al. 2015).

5.2 Inversion of SWS measurements for rock-physics parameters

A single measurement of dt and φ along a single ray-path is not sufficient to constrain the overall anisotropic symmetry system. Instead, a population of SWS measurements along a range of ray-paths must be inverted to reveal the overall anisotropy. Typically, a rock-physics model, assuming a particular anisotropic symmetry system, must be created, which is then compared with the observations, with the best-fitting rock-physics model parameterization being taken as the result (e.g. Verdon et al. 2009). In this case, I inverted measured fast polarization angles and time delays for a background VTI fabric (Thomsen 2002) overprinted with a single set of vertically aligned, unfilled, penny-shaped fractures (Hudson 1981), resulting in effective orthorhombic symmetry. The inversion is resolved for four free parameters of the effective orthorhombic medium between receivers and microseismic sources:

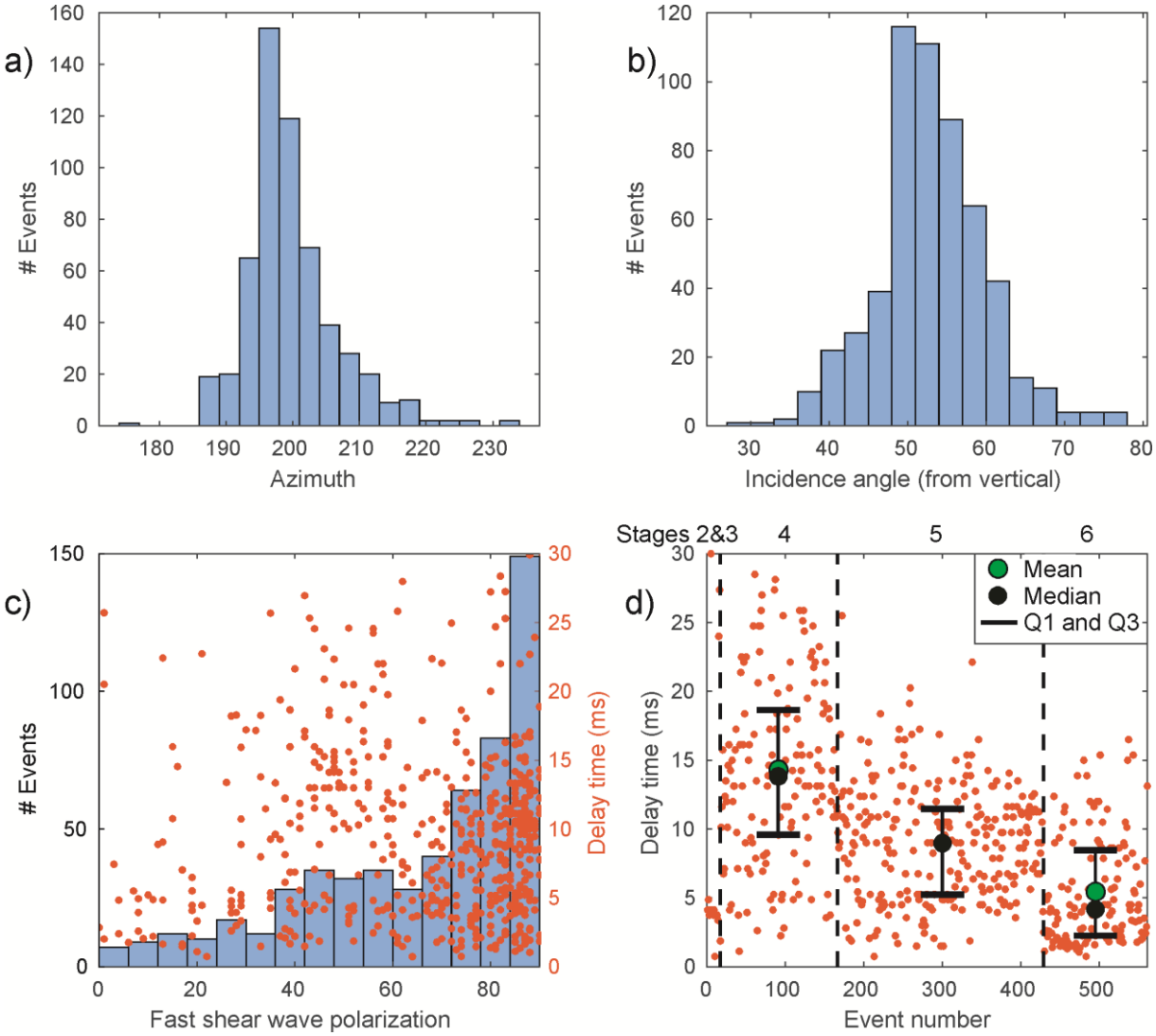

Fig. 49. The SWS results for the good-quality measurements. (a) A histogram of *P*-wave back azimuths, (b) a histogram of ray-path incidence angles, and (c) a histogram of the absolute value of the fast direction angles (relative to the *SV* orientation). Corresponding delay times are plotted on the secondary axis with orange dots, and (d) *dt* ordered by event origin time (orange dots) and its statistics per stage. Consecutive stages are separated by the dashed line. Note the median and mean for Stage 5 overlap. The population of measurements from stages 2 and 3 is insufficient to provide reliable statistics.

- the fracture density ξ and strike α of the vertical fracture set;
- Thomsen's parameters describing the VTI rock fabric;
- with only *S*-wave data, δ and ε cannot be constrained independently; instead, a ratio between δ and ε is resolved.

The inversion is performed following the method developed by Verdon et al. (2009) and Verdon and Wüstefeld (2013), described in Chapter 2. When iterating over a parameter space (ξ, α, δ, and γ), the elastic stiffness tensor providing velocities and polarizations of *S*-waves for any direction is computed by solving a Christoffel equation, independent from Thomsen (1986) weak anisotropy assumption. The background *P*- and *S*-wave velocities, V_P0 , V_S0 , and density are held constant through the model space. Velocities are based on the VTI velocity model developed in Chapter 4, whereas the mean density was taken from the well-log interval of interest.

5.2.1 Inversion results

The inversion of SWS measurements for an orthorhombic rock-physics model without any prior VTI fabric constraints resulted in unstable fracture parameters (strike α and crack density ξ). Those parameters were not constrained because the relatively weaker azimuthal anisotropy did not contribute significantly to the overall model due to limited azimuthal and incidence angle data coverage (Verdon et al. 2009) and stronger VTI fabric that dominates the inversion over the influence of cracks, due to relatively weak azimuthal anisotropy (Gajek et al. 2017).

However, the VTI fabric has already been observed by other geophysical methods, including:

- 3D VTI pre-stack depth migration velocity model (Kowalski et al. 2014) from a coincident 3D seismic survey, for which γ was derived using empirical relation to ε (Wang 2001);
- Backus-averaged well-logs – a benchmark model for the VTI velocity model inversion from microseismic data. Sonic, density, and natural gamma logs were used to obtain the vertical velocities V_P0 and V_S0, and to derive Thomsen's parameters (Thomsen 1986). Those parameters were downscaled to 200 Hz using a Backus-averaging scheme (Backus 1962);
- the VTI velocity model inverted for microseismic event location in Chapter 4.

The inverted VTI parameters for the three models are listed in Table 10. There is some disagreement between the prior VTI measurements. I, therefore, explored the effect on the fracture parameters (α and ξ) inverted from SWS measurements when the VTI fabric is fixed, doing this using each of the VTI fabrics determined from each of the geophysical methods (reflection seismic, well-log, microseismic).

I found that inversions for fracture strikes and densities are well constrained and consistent within the range of possible VTI parameters defined by the seismic, well log, and microseismic observations. Obtained fracture strikes were ranging between 102° and 108°, and fracture densities between 0.09 and 0.14, respectively (Fig. 50).

Table 10

Comparison of the input VTI parameters as derived from three geophysical methods and the resulting best-fit values for fracture strike and fracture density

	Input model	Surface seismic	Backus-averaged well log	Microseismic
Input	Epsilon ε	0.17	0.14	0.15
	Gamma γ	0.15	0.14	0.27
	Delta δ	0.11	0.02	0.02
Results	Fracture strike α	102°	108°	102°
	Fracture density ξ	0.09	0.14	0.10

5.2.2 Discussion

I assumed a VTI medium influenced by vertical cracks after judging from *S*-wave delay times and corresponding incidence angle (Fig. 49). However, for particular solely VTI settings, the *SV*-wave can propagate faster than *SH*-wave towards particular directions (Thomsen 1986). Nevertheless, I excluded this possibility basing on a synthetic model of *SH*- and *SV*-wave velocities in a VTI medium (Fig. 51). Two scenarios for the strongest (γ = 0.27) and the weakest (γ = 0.14) anisotropy among finally obtained models (Table 10) were tested, with common pa-

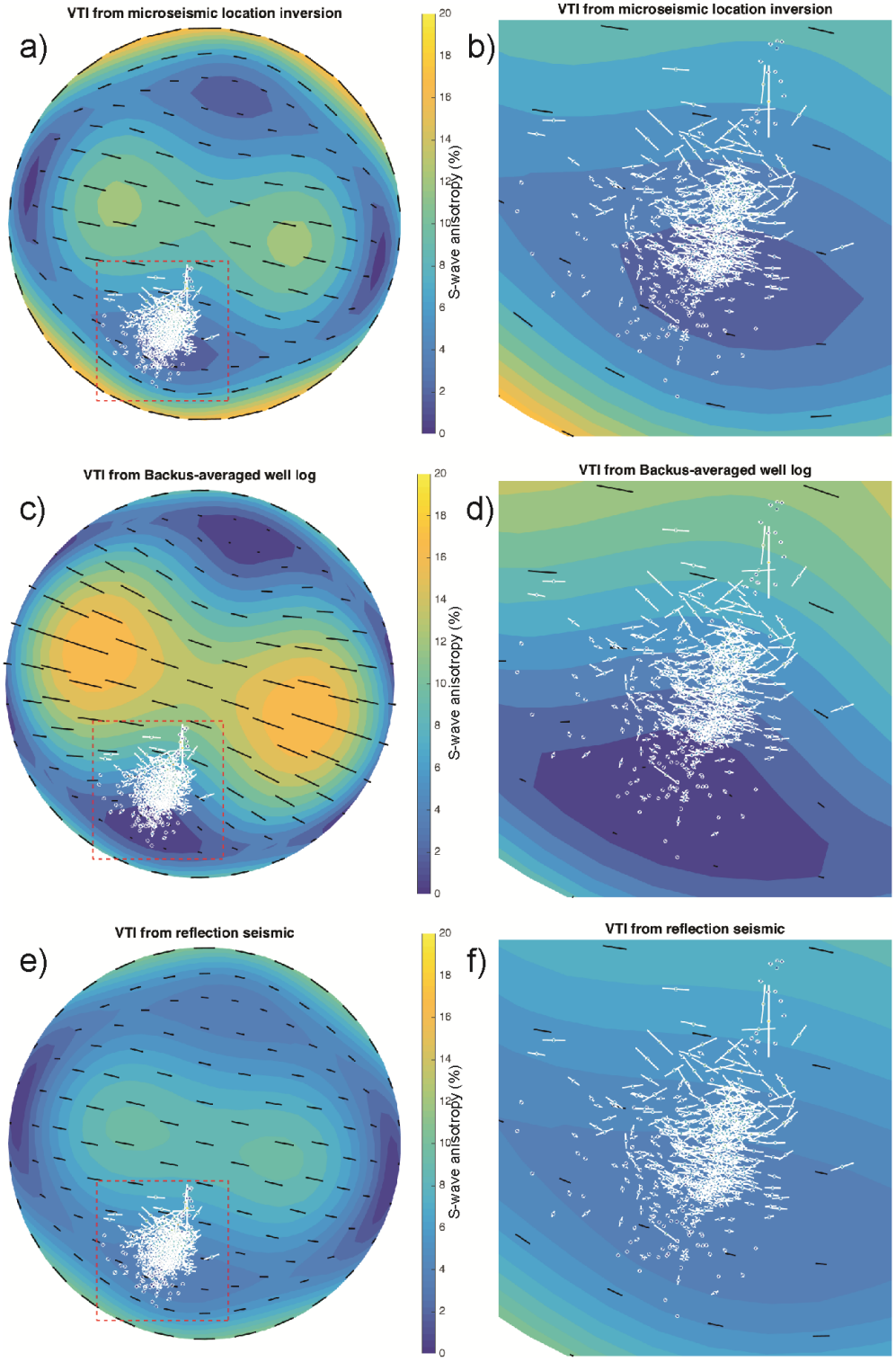

Fig. 50. Upper hemisphere projections of measured SWS data (white ticks) and the best fitting rock physics models (black ticks and background contours). Tick position indicates the azimuth and inclination of the ray-path, tick orientation indicates the fast shear-wave polarization, and colors and tick mark lengths indicate the magnitude of anisotropy. In (a) I show the result using the background VTI parameters derived from reflection seismic data, while (b) shows the same data zoomed in to the red box marked in (a), allowing the data to be inspected in more detail. In (c) and (d) I show the same for the case with background VTI parameters derived from the Backus-averaged well log, and in (e) and (f) I show the same for the case with background VTI parameters derived from the microseismic location velocity model.

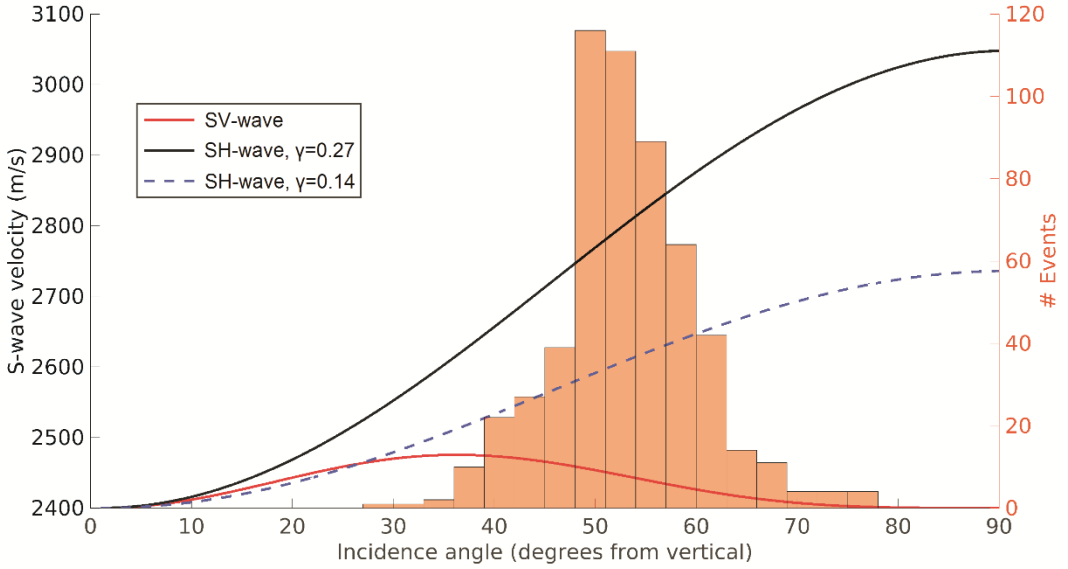

Fig. 51. Velocity (independent of γ) marked in the red solid line; *SH*-wave velocity for the higher anisotropy scenario (γ = 0.27) marked in the solid black line; *SH*-wave velocity for the lower anisotropy scenario (γ = 0.14) marked in the dashed blue line. In the background, a histogram of ray-path incidence angles of observation well at the toe end of the registered microseismic events is presented (right ordinate) indicating the range of incidence angles sampled by SWS measurements.

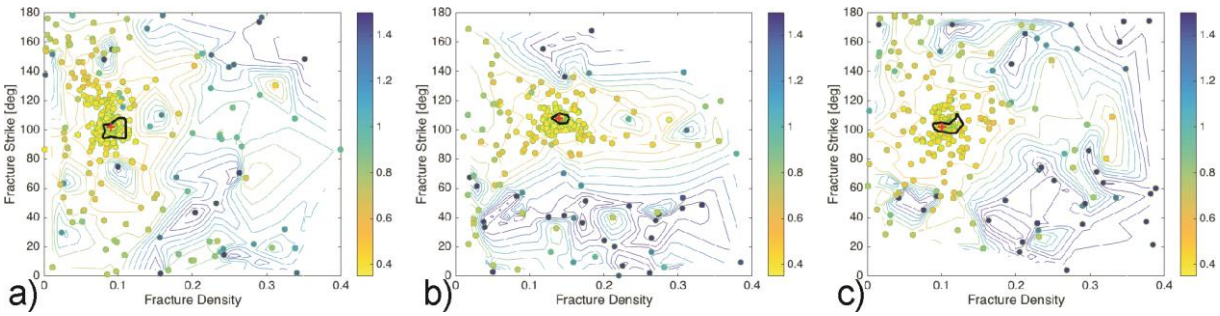

Fig. 52. Normalized misfit between the observed SWS and model values as a function of fracture density and strike, with background VTI parameters determined by (a) reflection seismic data, (b) Backus-averaged well log, and (c) the microseismic event location velocity model. The best-fit model in each case is marked by the red +, the green-edged dots mark the model parameters sampled by the neighborhood algorithm while searching for the best-fit model, and the contours represent smoothed misfit surfaces fitted to these sample points, with the solid black line delineating the 95% confidence interval.

rameters: V_S0 = 2400 m/s, ε = 0.15, δ = 0.02. For this particular VTI media, the *SV*-wave can be slightly faster than *SH*-wave in case of the lower anisotropy scenario. However, in the range of incidence angles sampled by SWS measurements, the *SH*-wave velocity prevails, hence, the assumption of VTI fabric with vertical cracks remains valid.

The observation well is close to the heel of the injection well, while the fracturing stages proceeded from the toe to the heel, as is common practice during hydraulic fracturing operations. Such geometry promotes the influence of the final stages of the stimulation by limiting the number of events from initial stages due to the S/N decay with the distance (Fig. 48). What's more, it limits the available azimuthal coverage of splitting measurements where the maximum azimuthal span is provided mostly by events within the closest, i.e., final stages (Fig. 47). Consequently, the unconstrained inversion of rock-physics parameters did not produce a stable result. The inversion became well-resolved after fixing the model's VTI parameters. The

geophysical data sources used to constrain the inversion vary significantly in scale from seismic frequencies, through microseismic frequencies, and up to sonic logs (downscaled to 200 Hz by Backus averaging). Nevertheless, the obtained fractures strike and fracture density were constrained well for all three models (Fig. 52).

The fracture strike of 102°–108° obtained using SWS data is close to the ca. 125° strike of the J2 fracture set obtained from XRMI log interpretation presented in Fig. 53 (Bobek and Jarosiński 2018). The J2 set has biggest contribution to the interval influencing SWS measurements and dominates in the Sasino formation (see Fig. 44b). It also contributes to the azimuthal anisotropy as detected by 3D wide-azimuth *P*-wave seismic data (Cyz and Malinowski 2018), where similar fracture strikes were inferred (Fig. 54). Estimated fracture strike can be influenced by a secondary fracture set J' striking approximately 80°; however, trying to invert for two fracture sets did not result in any stable strike of second fracture set.

The imaged direction differs by 45°–50° from the in-situ regional maximum horizontal stress orientation, which has an azimuth of ca. 155° (Jarosiński 2005). This indicates that the SWS measurements are imaging pre-existing natural fractures rather than new fractures created during stimulation, which would be expected to strike parallel to the maximum horizontal stress. However, this is to be expected when the geometry of observation and injection wells is considered: the ray paths from each of the stages are predominantly through the un-stimulated rock ahead (i.e. "heel-wards") of the stimulation stages, and therefore can only image the pre-existing natural fractures.

Baird et al. (2017) showed how the anisotropic system could change as hydraulic fracturing proceeds and ray-paths switch from propagation through unstimulated rock to rocks that have been stimulated, resulting in a change in the dominant fracture strike from that of the pre-existing fractures to that of the present-day maximum horizontal stress direction (and the presumed orientation of the hydraulic fractures). Baird et al. (2017) also noted an increase in the fracture compliance ratio (Z_N/Z_T) representing the change from partially filled and poorly-connected old fractures to the "clean", well-connected new hydraulic fractures (Schoenberg and Sayers 1995). To replicate such measurements, ray-paths through the already-stimulated volumes are required, which in turn would require an observation well at the toe end of the injection well for this particular well configuration.

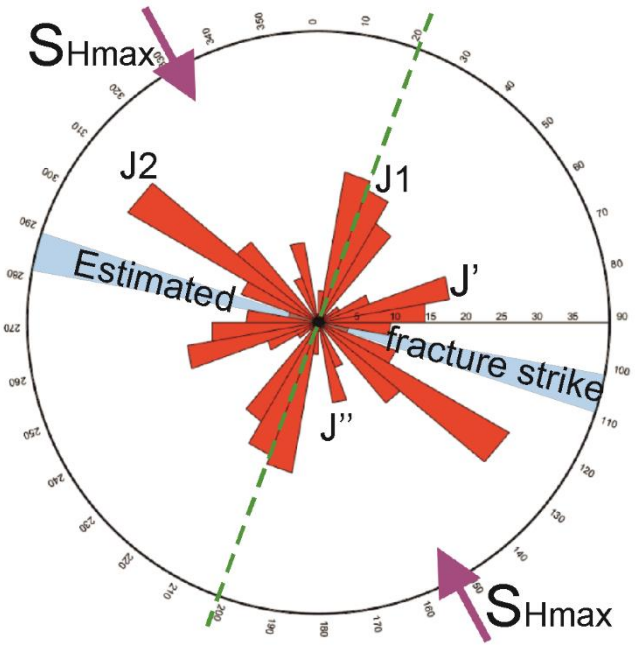

Fig. 53. Orientation of the subvertical fracture sets (joints) in the monitoring borehole obtained from XRMI log interpretation (the interval contributing to SWS measurements), the present-day maximum horizontal stress direction (SH_{max}), and the estimated fracture strike. The dashed green line points to the direction of the stimulated borehole horizontal segment.

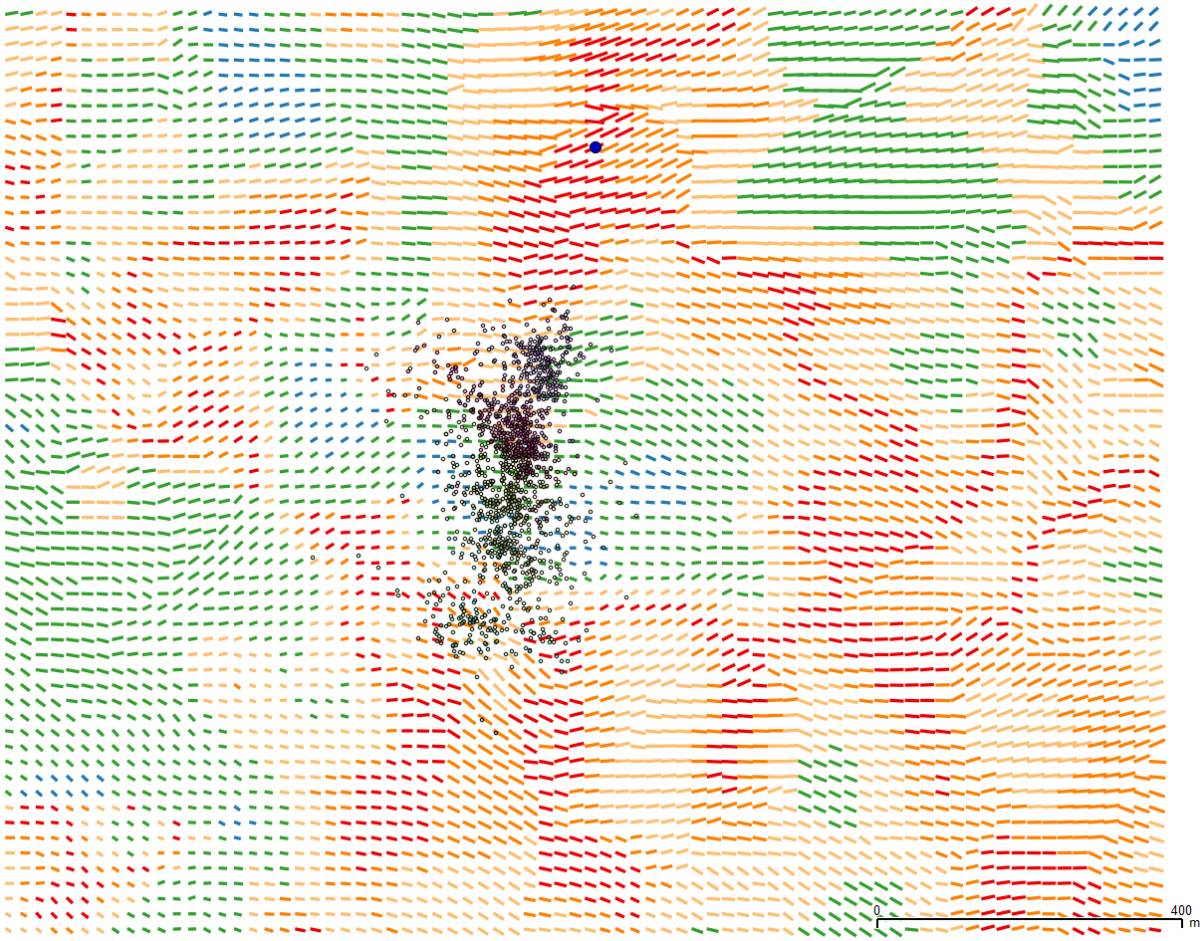

Fig. 54. Map of the seismic azimuthal anisotropy orientation and magnitude averaged over Jantar, Prabuty, and Sasino formations obtained from the amplitude versus azimuth (AVAZ) analysis. Lines indicating fracture strike are color-coded by the magnitude of azimuthal anisotropy obtained from the azimuth-dependent analysis of reflection coefficients observed in reflection seismic data (Cyz and Malinowski 2018). A value of 0 indicates that no anisotropy was observed.

5.3 Conclusions from this chapter

In this chapter, I used SWS observations and results from the previous chapter to invert orthorhombic stiffness tensor and estimate the parameters of fractures within the stimulated rock volume.

During the pilot hydraulic stimulation, significant SWS has been identified at the records of many microseismic events, indicating a presence of the anisotropy on the ray-path between receivers and the stimulated reservoir zone. After locating the events using the VTI velocity model, I took measurements of dt and φ on available records and performed a qualitative analysis of the measurements. Next, I have inverted the measurements for orthorhombic stiffness tensor and extracted fracture parameters. Inversion results show that the orthorhombic anisotropy of the stimulated shale is dominated by the VTI fabric overprinted by weaker azimuthal anisotropy. Therefore, the SWS phenomenon occurring in the microseismic records may be utilized to measure the azimuthal anisotropy and estimate fracture density and their orientation within the reservoir.

The imprint of the VTI fabric makes the inversion for fracture parameters more challenging than it otherwise would be. However, by incorporating constraints on VTI parameters from other geophysical measurements, such as reflection seismic and borehole logs, I was able to

invert the observed SWS measurements for a well-constrained estimate of fracture strike of 102°–108° with fracture density of 0.09–0.14.

The resulting fracture strike corresponds to the orientation of pre-existing fracture set J2 obtained from the XRMI log and from the analysis of the surface seismic data. The J2 set, as indicated in the previous chapter, dominates the fracture propagation and influences the fracture openings more than the maximum horizontal stress direction.

6. SUMMARY AND CONCLUSIONS

In this thesis, I presented a set of techniques for subsurface characterization which enhance downhole microseismic monitoring performance in the context of hydraulic fracturing for a single vertical observation borehole geometry. The most important is the methodology of the VTI anisotropic velocity model traveltime-based inversion, which uses all *P*-, *SH*-, and *SV*-waves present in anisotropic media, which most often is a case in the shale gas-related applications. Moreover, I provided a benchmark of proposed inversion methodology towards field applicability during ongoing hydraulic fracturing operations.

Secondly, I presented a technique of a probabilistic event location algorithm allowing for a reliable assessment of a stimulation performance. This approach results in a 3D probability density function distribution used for the events' location, due to accounting independently for uncertainties in both offset-depth and azimuth planes. Also, I included the description of fundamental and state of the art methodologies from fields of applied seismology and downhole microseismic monitoring.

I demonstrated applications of developed techniques to the field data from the hydraulic fracturing monitoring campaign in Lower Paleozoic shale resource play in northern Poland, preceded by a complete workflow for microseismic data processing. The VTI anisotropic velocity model inversion provided means for seismic velocities and anisotropy estimation, and hence, accurate mapping of microseismic events induced during a treatment. The obtained accurate locations, supplemented by individual 3D uncertainty distributions, allowed to delineate the extent of the cloud of microseismic events. Therefore, it allowed obtaining information on the Microseismic Volume (geological formations being fractured) and the effectiveness of hydraulic treatment.

Next, thanks to a reliable mapping of induced microseismicity, the SWS analysis could be successfully utilized to detect pre-existing fractures set most-probably controlling the development of induced fractures in the stimulated reservoir. The adopted methodology for fracture characterization based on SWS observations allowed to measure the azimuthal anisotropy and estimate fracture density together with their orientation within the reservoir (between the recording antenna and stimulated zone). Inverting the orthorhombic stiffness tensor by supplementing the VTI model with SWS observations of HTI anisotropy provided a complete description of the reservoir zone of interest, despite the challenging observation environment. Thanks to combining microseismic observations with the information provided by other methods, weaker HTI anisotropy dominated by VTI fabric was overcome to provide well-resolved information about the fracture system, regardless of narrow-azimuth observation geometry.

According to my judgment, both synthetic and real data examples included in this thesis validated both hypotheses which initiated this research.

Demonstrated synthetic studies proved that accounting for anisotropy during a process of velocity model building enhances the accuracy of microseismic event locations. Moreover, comparisons of microseismic event location error in anisotropic and isotropic velocity models showed the superiority of anisotropic approach (even with limited data) over various isotropic approaches.

Also, the case study presented in Chapter 5 successfully utilized the SWS phenomenon present in the microseismic records to estimate fracture density and their orientation within the analyzed shale gas reservoir. The obtained fracture orientation corresponded to the orientation interpreted from borehole XRMI data and surface seismic survey.

Even though SWS may be very useful for subsurface characterization in terms of fractures and anisotropy imaging, a suitable monitoring geometry is required to extract desired features of the subsurface. For example, when the same geometry of observation and injection wells as in the presented case study is considered, SWS measurements are imaging pre-existing natural fractures since seismic waves travel predominantly through the un-stimulated rock ahead (i.e. "heel-wards"). On the other hand, in order to observe how the anisotropic system can change as hydraulic fracturing proceeds (e.g., new fracture opening, change in the dominant fracture strike, fracture connectivity, saturation) ray-paths through the already-stimulated volumes are necessary. It requires an observation well at the toe-end of the injection well in case of this particular well configuration.

Described techniques together build up a comprehensive set of tools that can be applied in the industry practice for improving the quality of a final microseismic monitoring interpretation. Moreover, the included benchmark of a new technique of traveltime-based VTI anisotropic velocity model inversion showed, that it is feasible to become a nearreal- time on-site implementation during ongoing microseismic monitoring of hydraulic fracturing.

References

Aki, K., and P. Richards (1980), *Quantitive Seismology: Theory and Methods*, Vol. 1, W.H. Freeman & Co., San Francisco, 557 pp.

Al-Harrasi, O.H., A. Al-Anboori, A. Wüstefeld, and J.M Kendall (2011), Seismic anisotropy in a hydrocarbon field estimated from microseismic data, *Geophys. Prospect.* **59**, 2, 227–243, DOI: 10.1111/j.1365-2478.2010.00915.x.

Allen, R.V. (1978), Automatic earthquake recognition and timing from single traces, *Bull. Seismol. Soc. Am.* **68**, 5, 1521–1532.

Alsina, D., and R. Snieder (1995), Small-scale sublithospheric continental mantle deformation: constraints from SKS splitting observations, *Geophys. J. Int.* **123**, 2, 431–448, DOI: 10.1111/j.1365-246X.1995.tb06864.x.

Ando, M., Y. Ishikawa, and H. Wada (1980), S-wave anisotropy in the upper mantle under a volcanic area in Japan, *Nature* **286**, 43–46, DOI: 10.1038/286043a0.

Backus, G.E. (1962), Long-wave elastic anisotropy produced by horizontal layering, *J. Geophys. Res.* **67**, 11, 4427–4440, DOI: 10.1029/JZ067i011p04427.

Baird, A.F., J.M. Kendall, J.P. Verdon, A. Wuestefeld, T.E. Noble, Y. Li, M. Dutko, and Q.J. Fisher (2013), Monitoring increases in fracture connectivity during hydraulic stimulations from temporal variations in shear wave splitting polarization, *Geophys. J. Int.* **195**, 2, 1120–1131, DOI: 10.1093/gji/ggt274.

Baird, A.F., J.M. Kendall, and J. Budge (2016), Shear wave splitting and fluid flow in highly anisotropic shale gas reservoirs. **In:** *Proc. 78th EAGE Conference and Exhibition 2016*, EAGE Publications BV, 1–5, DOI: 10.3997/2214-4609.201600999.

Baird, A.F., J.M. Kendall, Q.J. Fisher, and J. Budge (2017), The role of texture, cracks, and fractures in highly anisotropic shales, *J. Geophys. Res. Solid Earth* **122**, 12, 10341–10351, DOI: 10.1002/2017JB014710.

Banik, N.C. (1987), An effective anisotropy parameter in transversely isotropic media, *Geophysics* **52**, 12, 1654–1664, DOI: 10.1190/1.1442282.

Bardainne, T., and E. Gaucher (2010), Constrained tomography of realistic velocity models in microseismic monitoring using calibration shots, *Geophys. Prospect.* **58**, 5, 739–753, DOI: 10.1111/j.1365-2478.2010.00912.x.

Becquey, M., and M. Dubesset (1990), Three-component sonde orientation in a deviated well, *Geophysics* **55**, 10, 1386–1388, DOI: 10.1190/1.1442786.

Bentley, J.L. (1975), Multidimensional binary search trees used for associative searching, *Commun. ACM* **18**, 9, 509–517, DOI: 10.1145/361002.361007.

Bobek, K., and M. Jarosiński (2018), Parallel structural interpretation of drill cores and microresistivity scanner images from gas-bearing shale (Baltic Basin, Poland), *Interpretation* **6**, 3, SH25–SH38, DOI: 10.1190/INT-2017-0211.1.

Bobek, K., M. Jarosinski, and R. Pachytel (2017), Tectonic structures in shale that you do not include in your reservoir model. **In:** *Proc. 51st U.S. Rock Mechanics/Geomechanics Symposium, San Francisco, Ca, USA, June 2017*.

Bos, L., T. Danek, M.A. Slawinski, and T. Stanoev (2018), Statistical and numerical considerations of Backus-average product approximation, *J. Elast.* **132**, 1, 141–159, DOI: 10.1007/s10659-017-9659-9.

Bowman, J.R., and M. Ando (1987), Shear-wave splitting in the upper-mantle wedge above the Tonga subduction zone, *Geophys. J. Int.* **88**, 1, 25–41, DOI: 10.1111/j.1365-246X.1987.tb01367.x.

Caffagni, E., D.W. Eaton, J.P. Jones, and M. van der Baan (2016), Detection and analysis of microseismic events using a Matched Filtering Algorithm (MFA), *Geophys. J. Int.* **206**, 1, 644–658, DOI: 10.1093/gji/ggw168.

Carcione, J.M. (ed.) (2007), *Wave Fields in Real Media: Wave Propagation in Anisotropic, Anelastic, Porous and Electromagnetic Media*, Elsevier Seismic Exploration Series, Vol. 38. Elsevier, Amsterdam.

Černỳ, V. (1985), Thermodynamical approach to the traveling salesman problem: An efficient simulation algorithm, *J. Optimiz. Theory Appl*. **45**, 1, 41–51.

Červenỳ, V., and I. Pšenčík (1979), Ray amplitudes of seismic body waves in laterally inhomogeneous media, *Geophys. J. Int.* **57**, 1, 91–106, DOI: 10.1111/j.1365-246X.1979.tb03774.x.

Cesca, S., and F. Grigoli (2015), Full waveform seismological advances for microseismic monitoring. **In:** R. Dmowska (ed.), *Advances in Geophysics*, Vol. 56, Elsevier, Amsterdam, 169–228, DOI: 10.1016/bs.agph.2014.12.002.

Chander, R. (1975), On tracing seismic rays with specified end-points, *J. Geophys*. – *Zeitsch. Geophys*. **41**, 2, 173–177.

Chen, Y. (2020), Automatic microseismic event picking via unsupervised machine learning, *Geophys. J. Int.* **222**, 3, 1750–1764, DOI: 10.1093/gji/ggaa186.

Chevrot, S. (2000), Multichannel analysis of shear wave splitting, *J. Geophys. Res. Solid Earth* **105**, B9, 21579–21590, DOI: 10.1029/2000JB900199.

Christoffersson, A., E.S. Husebye, and S.F. Ingate (1988), Wavefield decomposition using ML-probabilities in modelling single-site 3-component records, *Geophys. J. Int.* **93**, 2, 197–213, DOI: 10.1111/j.1365-246X.1988.tb01996.x.

Crampin, S. (1984), An introduction to wave propagation in anisotropic media, *Geophys. J. Int.* **76**, 1, 17–28, DOI: 10.1111/j.1365-246X.1984.tb05018.x.

Crampin, S., and S.V. Zatsepin (1995), Production seismology: The use of shear waves to monitor and mode production in a poro-reactive and interactive reservoir. **In:** *SEG Technical Program Expanded Abstracts 1995*, Society of Exploration Geophysicists, 199–202, DOI: 10.1190/1.1887499.

Crampin, S., R. Evans, B. Üçer, M. Doyle, J.P. Davis, G.V. Yegorkina, and A. Miller (1980), Observations of dilatancy-induced polarization anomalies and earthquake prediction, *Nature* **286**, 874–877, DOI: 10.1038/286874a0.

Crampin, S., R.A. Stephen, and R. McGonigle (1982), The polarization of *P*-waves in anisotropic media, *Geophys. J. Int.* **68**, 2, 477–485, DOI: 10.1111/j.1365-246X.1982.tb04910.x.

Crampin, S., S. Chastin, and Y. Gao (2003), Shear-wave splitting in a critical crust: III. Preliminary report of multi-variable measurements in active tectonics, *J. Appl. Geophys.* **54**, 3–4, 265–277, DOI: 10.1016/j.jappgeo.2003.01.001.

Cyz, M., and M. Malinowski (2018), Seismic azimuthal anisotropy study of the Lower Paleozoic shale play in northern Poland, *Interpretation* **6**, 3, SH1–SH12, DOI: 10.1190/INT-2017-0200.1.

Danek, T., A. Leśniak, and A. Pięta (2010), *Numerical Modeling of Seismic Wave Propagation in Selected Anisotropic Media*, Wydawnictwo Instytutu Gospodarki Surowcami Mineralnymi i Energią PAN.

DiSiena, J.P., J.E. Gaiser, D. Corrigan, and M.N. Toksöz (1984), Horizontal components and shear wave analysis of three-component VSP data. **In:** M.N. Toksoz and R.R. Stewart (eds.), *Vertical Seismic Profiling, Part B: Advanced Concepts*, Geophysical Press.

Eberhart, R., and J. Kennedy (1995), A new optimizer using particle swarm theory. **In:** *MHS'95. Proceedings of the Sixth International Symposium on Micro Machine and Human Science*, IEEE, 39–43.

Ebrom, D.A., R.H. Tatham, K.K. Sekharan, J.A. McDonald, and G.H.F. Gardner (1990), Hyperbolic traveltime analysis of first arrivals in an azimuthally anisotropic medium: A physical modeling study, *Geophysics* **55**, 2, 185–191, DOI: 10.1190/1.1442825.

Eisner, L., D. Abbott, W.B. Barker, J. Lakings, and M.P. Thornton (2008), Noise suppression for detection and location of microseismic events using a matched filter. **In:** *SEG Technical Program Expanded Abstracts 2008*, Society of Exploration Geophysicists, 1431–1435, DOI: 10.1190/1.3059184.

Eisner, L., P.M. Duncan, W.M. Heigl, and W.R. Keller (2009), Uncertainties in passive seismic monitoring, *The Leading Edge* **28**, 6, 648–655, DOI: 10.1190/1.3148403.

Eisner, L., M. Thornton, and J. Griffin (2011), Challenges for microseismic monitoring. **In:** *SEG Technical Program Expanded Abstracts 2011*, Society of Exploration Geophysicists, 1519–1523, DOI: 10.1190/1.3627491.

Ellis, R.G., and D.W. Oldenburg (1994), Applied geophysical inversion, *Geophys. J. Int.* **116**, 1, 5–11, DOI: 10.1111/j.1365-246X.1994.tb02122.x.

Farra, V., and R. Madariaga (1987), Seismic waveform modeling in heterogeneous media by ray perturbation theory, *J. Geophys. Res. Solid Earth* **92**, B3, 2697–2712, DOI: 10.1029/JB092iB03p02697.

Fink, M. (1999), Time-reversed acoustics, *Sci. Am.* **281**, 5, 91–97, https://www.jstor.org/stable/26058488.

Flinn, E.A. (1965), Signal analysis using rectilinearity and direction of particle motion, *Proc. IEEE* **53**, 12, 1874–1876, DOI: 10.1109/PROC.1965.4462.

Gajek,W., J. Trojanowski, and and M. Malinowski (2016), Advantages of probabilistic approach to microseismic events location – a case study from Northern Poland. **In:** *Proc. 78th EAGE Conference and Exhibition 2016*, EAGE Publications BV, 1–3, DOI: 10.3997/2214-4609.201600909.

Gajek,W., J.P. Verdon, M. Malinowski, and J. Trojanowski (2017), Imaging seismic anisotropy in a shale gas reservoir by combining microseismic and 3D surface reflection seismic data. **In:** *Proc. 79th EAGE Conference and Exhibition 2017 – Workshops*, EAGE Publications BV, DOI: 10.3997/2214-4609.201701689.

Gajek,W., J. Trojanowski, and M. Malinowski (2018a), Downhole microseismic monitoring at a pilot hydraulic fracturing site in Poland. **In:** *Proc. Seventh EAGE Workshop on Passive Seismic 2018*, EAGE Publications BV, 1–6, DOI: 10.3997/2214-4609.201800059.

Gajek, W., J. Trojanowski, M. Malinowski, M. Jarosiński, and M. Riedel (2018b), Results of the downhole microseismic monitoring at a pilot hydraulic fracturing site in Poland — Part 1: Event location and stimulation performance, *Interpretation* **6**, SH39–SH48, DOI: 10.1190/INT-2017-0205.1.

Gajek, W., M. Malinowski, and J.P. Verdon (2018c), Results of downhole microseismic monitoring at a pilot hydraulic fracturing site in Poland — Part 2: *S*-wave splitting analysis, *Interpretation* **6**, 3, SH49–SH58, DOI: 10.1190/INT-2017-0207.1.

Gao, S., P.M. Davis, H. Liu, P.D. Slack, Y.A. Zorin, V.V. Mordvinova, V.M. Kozhevnikov, and R.P. Meyer (1994), Seismic anisotropy and mantle flow beneath the Baikal rift zone, *Nature* **371**, 149–151, DOI: 10.1038/371149a0.

Gao, S., P.M. Davis, H. Liu, P.D. Slack, A.W. Rigor, Y.A. Zorin, V.V. Mordvinova, V.M. Kozhevnikov, and N.A. Logatchev (1997), SKS splitting beneath continental rift zones, *J. Geophys. Res. Solid Earth* **102**, B10, 22781–22797, DOI: 10.1029/97JB01858.

Geiger, L. (1912), Probability method for the determination of earthquake epicenters from the arrival time only, *Bull. St. Louis Univ*. **8**, 1, 56–71.

Gholami, R., A. Moradzadeh, V. Rasouli, and J. Hanachi (2016), Shear wave splitting analysis to estimate fracture orientation and frequency dependent anisotropy, *Acta Geophys*. **64**, 1, 76–100, DOI: 10.1515/acgeo-2015-0060.

Gibowicz, S.J., and A. Kijko (2013), *An Introduction to Mining Seismology*, Elsevier, 399 pp.

Gillberg, T., Ø. Hjelle, and A.M. Bruaset (2012), Accuracy and efficiency of stencils for the eikonal equation in earth modelling, *Comput. Geosci*. **16**, 933–952, DOI: 10.1007/s10596-012-9296-0.

Glantz, S.A., and B.K. Slinker (1990), *Primer of Applied Regression and Analysis of Variance*, McGraw-Hill, New York.

Gledhill, K., and D. Gubbins (1996), SKS splitting and the seismic anisotropy of the mantle beneath the Hikurangi subduction zone, New Zealand, *Phys. Earth Planet. Int.* **95**, 3–4, 227–236, DOI: 10.1016/0031-9201(95)03118-9.

Goldberg, D.E. (1989), *Genetic Algorithms in Search, Optimization, and Machine Learning*, Addison-Wesley Publ. Co.

Goldberg, D.E., and J.H. Holland (1988), Genetic algorithms and machine learning, *Machine Learning* **3**, 95–99, DOI: 10.1023/A:1022602019183.

Grechka, V. (2007), Multiple cracks in VTI rocks: Effective properties and fracture characterization, *Geophysics* **72**, 5, D81–D91, DOI: 10.1190/1.2751500.

Grechka, V. (2010), Data-acquisition design for microseismic monitoring, *The Leading Edge* **29**, 3, 278–282, DOI: 10.1190/1.3353723.

Grechka, V., and A.A. Duchkov (2011), Narrow-angle representations of the phase and group velocities and their applications in anisotropic velocity-model building for microseismic monitoring, *Geophysics* **76**, 6, WC127–WC142, DOI: 10.1190/geo2010-00408.1.

Grechka, V., and W.M. Heigl (2017), *Microseismic Monitoring*, Society of Exploration Geophysicists, Tulsa, 468 pp.

Grechka, V., and S. Yaskevich (2013), Inversion of microseismic data for triclinic velocity models, *Geophys. Prospect.* **61**, 6, 1159–1170, DOI: 10.1111/1365-2478.12042.

Grechka, V., and S. Yaskevich (2014), Azimuthal anisotropy in microseismic monitoring: A Bakken case study, *Geophysics* **79**, 1, KS1–KS12, DOI: 10.1190/geo2013-0211.1.

Grechka, V., P. Singh, and I. Das (2011), Estimation of effective anisotropy simultaneously with locations of microseismic events, *Geophysics* **76**, 6, WC143–WC155, DOI: 10.1190/geo2010-0409.1.

Grechka, V., A. De La Pena, E. Schisselé-Rebel, E. Auger, and P.F. Roux (2015), Relative location of microseismicity, *Geophysics* **80**, 6, WC1–WC9, DOI: 10.1190/geo2014-0617.1.

Guo, N., and S. Fagin (2002), Becoming effective velocity-model builders and depth imagers, Part 2—The basics of velocity-model building, examples and discussions, *The Leading Edge* **21**, 12, 1210–1216, DOI: 10.1190/1.1536136.

Gupta, I.N. (1973), Dilatancy and premonitory variations of *P*, *S* travel times, *Bull. Seismol. Soc. Am.* **63**, 3, 1157–1161.

Hagen, D.C. (1982), The application of principal components analysis to seismic data sets, *Geoexploration* **20**, 1–2, 93–111, DOI: 10.1016/0016-7142(82)90009-6.

Hall, S.A., J.M. Kendall, J. Maddock, and Q. Fisher (2008), Crack density tensor inversion for analysis of changes in rock frame architecture, *Geophys. J. Int.* **173**, 2, 577–592, DOI: 10.1111/j.1365-246X.2008.03748.x.

Harris, J.B. (1996), Shear-wave splitting in Quaternary sediments: Neotectonic implications in the central New Madrid seismic zone, *Geophysics* **61**, 6, 1871–1882, DOI: 10.1190/1.1444102.

Havskov, J., and G. Alguacil (2004), *Instrumentation in Earthquake Seismology*, Springer, Dordrecht.

Hongsresawat, S., M.P. Panning, R.M. Russo, D.A. Foster, V. Monteiller, and S. Chevrot (2015), USArray shear wave splitting shows seismic anisotropy from both lithosphere and asthenosphere, *Geology* **43**, 8, 667–670, DOI: 10.1130/G36610.1.

Hooke, R. (1678), *Lectures De Potentia Restitutiva, or of Spring Explaining the Power of Springing Bodies*, London, Printed for J. Martyn Printer to the Royal Society, Bell.

Horne, S. (2003), Fracture characterization from walkaround VSPs, *Geophys. Prospect.* **51**, 6, 493–499, DOI: 10.1046/j.1365-2478.2003.00391.x.

Houliston, D.J., G. Waugh, and J. Laughlin (1984), Automatic real-time event detection for seismic networks, *Computers & Geosciences* **10**, 4, 431–436, DOI: 10.1016/0098-3004(84)90043-8.

Huang, G., J. Ba, Q. Du, and J.M. Carcione (2019), Simultaneous inversion for velocity model and microseismic sources in layered anisotropic media, *J. Petrol. Sci. Eng.* **173**, 1453–1463, DOI: 10.1016/j.petrol.2018.10.071.

Huang,W., R. Wang, H. Li, and Y. Chen (2017), Unveiling the signals from extremely noisy microseismic data for high-resolution hydraulic fracturing monitoring, *Sci. Rep.* **7**, 11996, DOI: 10.1038/s41598-017-09711-2.

Hudson, J.A. (1981), Wave speeds and attenuation of elastic waves in material containing cracks, *Geophys. J. Int.* **64**, 1, 133–150, DOI: 10.1111/j.1365-246X.1981.tb02662.x.

Hudson, J.A., E. Liu, and S. Crampin (1996), The mechanical properties of materials with interconnected cracks and pores, *Geophys. J. Int.* **124**, 1, 105–112, DOI: 10.1111/j.1365-246X.1996.tb06355.x.

Jansky, J., V. Plicka, and L. Eisner (2010), Feasibility of joint 1D velocity model and event location inversion by the Neighbourhood algorithm, *Geophys. Prospect.* **58**, 2, 229–234, DOI: 10.1111/j.1365-2478.2009.00820.x.

Jarosiński, M. (2005), Ongoing tectonic reactivation of the Outer Carpathians and its impact on the foreland: Results of borehole breakout measurements in Poland, *Tectonophysics* **410**, 1–4, 189–216, DOI: 10.1016/j.tecto.2004.12.040.

Jarosiński, M. (2006), Recent tectonic stress field investigations in Poland: a state of the art, *Geol. Quart.* **50**, 3, 303–321.

Johnston, J.E., and N.I. Christensen (1995), Seismic anisotropy of shales, *J. Geophys. Res. Solid Earth* **100**, B4, 5991–6003, DOI: 10.1029/95JB00031.

Jones, G.A., J.M. Kendall, I. Bastow, D.G. Raymer, and A.Wuestefeld (2014), Characterization of fractures and faults: a multi-component passive microseismic study from the Ekofisk reservoir, *Geophys. Prospect.* **62**, 4, 779–796, DOI: 10.1111/1365-2478.12139.

Julian, B.R., and D. Gubbins (1977), Three-dimensional seismic ray tracing, *J. Geophys.* **43**, 1, 95–113, https://journal.geophysicsjournal.com/JofG/article/view/133.

Jurkevics, A. (1988), Polarization analysis of three-component array data, *Bull. Seismol. Soc. Am.* **78**, 5, 1725–1743.

Kendall, J.M., and P.G. Silver (1996), Constraints from seismic anisotropy on the nature of the lowermost mantle, *Nature* **381**, 409–412, DOI: 10.1038/381409a0.

Kendall, J.M., Q.J. Fisher, S.C. Crump, J. Maddock, A. Carter, S.A. Hall, J. Wookey, S.L. Valcke, M. Casey, G. Lloyd, and W.B. Ismail (2007), Seismic anisotropy as an indicator of reservoir quality in siliciclastic rocks, *Geol. Soc. London, Spec. Publ.* **292**, 123–136, DOI: 10.1144/SP292.7.

Kirkpatrick, S., C.D. Gelatt Jr., and M.P. Vecchi (1983), Optimization by simulated annealing, *Science* **220**, 4598, 671–680, DOI: 10.1126/science.220.4598.671.

Klemperer, S.L. (1987), Seismic noise-reduction techniques for use with vertical stacking; Aan empirical comparison, *Geophysics* **52**, 3, 322–334, DOI: 10.1190/1.1442306.

Kosarev, G.L., L.I. Makeyeva, and L.P. Vinnik (1984), Anisotropy of the mantle inferred from observations of *P* to *S* converted waves, *Geophys. J. Int.* **76**, 1, 209–220, DOI: 10.1111/j.1365-246X.1984.tb05037.x.

Kowalski, H., P. Godlewski, W. Kobusinski, J. Makarewicz, M. Podolak, A. Nowicka, Z. Mikolajewski, D. Chase, R. Dafni, A. Canning, and Z. Koren (2014), Imaging and characterization of a shale reservoir onshore Poland, using full-azimuth seismic depth imaging, *First Break* **32**, 101–109.

Krzemiński, L., and P. Poprawa (2006), Geochemistry of the Ordovician and Silurian clastic sediments of the Koszalin-Chojnice zone and the western Baltic Basin (N Poland), *Pr. Państw. Inst. Geol.* **186**, 123–148 (in Polish).

Lay, T., and T.C. Wallace (1995), *Modern Global Seismology*, International Geophysics Series, Vol. 58, Academic Press (an imprint of Elsevier), San Diego.

Li, J., H. Zhang, W.L. Rodi, and M.N. Toksoz (2013), Joint microseismic location and anisotropic tomography using differential arrival times and differential backazimuths, *Geophys. J. Int.* **195**, 3, 1917–1931, DOI: 10.1093/gji/ggt358.

Liner, C., and T. Fei (2007), The Backus number, *The Leading Edge* **26**, 4, 420–426, DOI: 10.1190/1.2723204.

Liu, E., and A. Martinez (2014), *Seismic Fracture Characterization*, Elsevier.

Lomax, A., A. Michelini, and A. Curtis (2009), Earthquake location, direct, global-search methods. **In:** *Complexity in Encyclopedia of Complexity and Systems Science*, Part 5, Springer, 2449–2473.

Lonardelli, I., H.R. Wenk, and Y. Ren (2007), Preferred orientation and elastic anisotropy in shales, *Geophysics* **72**, 2, D33–D40, DOI: 10.1190/1.2435966.

Lynn, H.B., and L. Thomsen (1986), Shear wave exploration along the principal axis. **In:** *Proc. 56th Annual SEG International Meeting, Expanded Abstracts*, 473–476.

Lynn, H.B., W.E. Beckham, K.M. Simon, C.R. Bates, M. Layman, and M. Jones (1999), *P*-wave and *S*-wave azimuthal anisotropy at a naturally fractured gas reservoir, Bluebell-Altamont Field, Utah, *Geophysics* **64**, 4, 1312–1328, DOI: 10.1190/1.1444636.

MacBeth, C. (2002), *Multi-Component VSP Analysis for Applied Seismic Anisotropy*, Handbook on Geophysical Exploration. Seismic Exploration, Vol. 26, Pergamon (an imprint of Elsevier), Amsterdam.

Magotra, N., N. Ahmed, and E. Chael (1987), Seismic event detection and source location using single-station (three-component) data, *Bull. Seismol. Soc. Am.* **77**, 3, 958–971.

Mallick, S., and L.N. Frazer (1988), Rapid computation of multioffset vertical seismic profile synthetic seismograms for layered media, *Geophysics* **53**, 4, 479–491, DOI: 10.1190/1.1442479.

Martin, M.A., and T.L. Davis (1987), Shear-wave birefringence: A new tool for evaluating fractured reservoirs, *The Leading Edge* **6**, 10, 22–28, DOI: 10.1190/1.1439333.

Maxwell, S. (2009), Microseismic location uncertainty, *CSEG Recorder* 34, 4, 41–46.

Maxwell, S. (2014), *Microseismic Imaging of Hydraulic Fracturing: Improved Engineering of Unconventional Shale Reservoirs*, Distinguished Instructor Series, No. 17, Society of Exploration Geophysicists, Tulsa, DOI: 10.1190/1.9781560803164.

Maxwell, S.C., L. Bennett, M. Jones, and J. Walsh (2010), Anisotropic velocity modeling for microseismic processing: Part 1—impact of velocity model uncertainty. **In:** *SEG Technical Program Expanded Abstracts 2010*, 2130–2134, DOI: 10.1190/1.3513267.

Mayerhofer, M.J., E. Lolon, N.R. Warpinski, C.L. Cipolla, D. Walser, and C.M. Rightmire (2010), What is stimulated reservoir volume? *SPE Prod. & Oper*. **25**, 1, 89–98, DOI: 10.2118/119890-PA.

McMechan, G.A. (1982), Determination of source parameters by wavefield extrapolation, *Geophys. J. Int.* **71**, 3, 613–628 DOI: 10.1111/j.1365-246X.1982.tb02788.x.

Metropolis, N., and S. Ulam (1949), The Monte Carlo method, *J. Am. Statistic. Assoc*. **44**, 247, 335–341, DOI: 10.1080/01621459.1949.10483310.

Miyazawa, M., R. Snieder, and A. Venkataraman (2008), Application of seismic interferometry to extract *P*- and *S*-wave propagation and observation of shear-wave splitting from noise data at Cold Lake, Alberta, Canada, *Geophysics* **73**, 4, D35–D40, DOI: 10.1190/1.2937172.

Mizuno, T., S. Leaney, and G. Michaud (2010), Anisotropic velocity model inversion for imaging the microseismic cloud. **In:** *Proc. 72nd EAGE Conference and Exhibition incorporating SPE EUROPEC 2010*, cp-161-00172, DOI: 10.3997/2214-4609.201400764.

Modliski, Z., and T. Podhalaska (2010), Outline of the lithology and depositional features of the lower Paleozoic strata in the Polish part of the Baltic region, *Geol. Quart.* **54**, 2, 109–121.

Mueller, M.C. (1991), Prediction of lateral variability in fracture intensity using multicomponent shear-wave surface seismic as a precursor to horizontal drilling in the Austin Chalk, *Geophys. J. Int.* **107**, 3, 409–415, DOI: 10.1111/j.1365-246X.1991.tb01402.x.

Mueller, M.C., A.J. Boyd, and C. Esmersoy (1994), Case studies of the dipole shear anisotropy log. **In:** *SEG Technical Program Expanded Abstracts 1994*, Society of Exploration Geophysicists, 1143–1146, DOI: 10.1190/1.1822721.

Murat, M.E., and A.J. Rudman (1992), Automated first arrival picking: A neural network approach, *Geophys. Prospect.* **40**, 6, 587–604, DOI: 10.1111/j.1365-2478.1992.tb00543.x.

Narr, W., D.S. Schechter, and L.B. Thompson (2006), *Naturally Fractured Reservoir Characterization*, Society of Petroleum Engineers, Richardson.

Nichols, D., F. Muir, and M. Schoenberg (1989), Elastic properties of rocks with multiple sets of fractures. **In:** *SEG Technical Program Expanded Abstracts 1989*, Society of Exploration Geophysicists, 471–474, DOI: 10.1190/1.1889682.

Nicolas, A., and N.I. Christensen (1987), Formation of anisotropy in upper mantle peridotites – a review. **In:** K. Fuchs and C.Froidevaux (eds.), *Composition, Structure and Dynamics of the Lithosphere-Asthenosphere System*, Geodynamics Series, Vol. 16, American Geophysical Union, 111–123, DOI: 10.1029/GD016p0111.

Niu, F., and A.M. Perez (2004), Seismic anisotropy in the lower mantle: A comparison of waveform splitting of SKS and SKKS, *Geophys. Res. Lett.* **31**, 24, L24612, DOI: 10.1029/2004GL021196.

Nur, A., and G. Simmons (1969), Stress-induced velocity anisotropy in rock: An experimental study, *J. Geophys. Res.* **74**, 27, 6667–6674, DOI: 10.1029/JB074i027p06667.

Pasternacki, A. (2016), Ocena efektywności procesu szczelinowania hydraulicznego w eksploatacji gazu ziemnego z łupków ilastych na podstawie badań mikrosejsmicznych, Ph.D. Thesis, AGH University of Science and Technology, Kraków (in Polish).

Patterson, D., and X.M. Tang (2001), Shear wave anisotropy measurement using cross-dipole acoustic logging: An overview, *Petrophysics* **42**, 02, SPWLA-2001-v42n2a4.

Podhalańska, T., M.I. Waksmundzka, A. Becker, J. Roszkowska-Remin, I. Dyrka, A. Feldman-Olszewska, A. Głuszyński, I. Grotek, M. Janas, P. Karcz, G. Nowak, J. Pacześna, M. Roman, M. Sikorska-Jaworowska, M. Kuberska, A. Kozłowska, and K. Sobień (2016), Strefy perspektywiczne występowania niekonwencjonalnych złóż węglowodorów w kambryjskich,

ordowickich, sylurskich i karbońskich kompleksach skalnych Polski – integracja wyników badań, *Prz. Geol.* **64**, 12, 1008–1021 (in Polish).

Poprawa, P. (2010), Shale gas potential of the Lower Palaeozoic complex in the Baltic and Lublin-Podlasie basins (Poland), *Prz. Geol.* **58**, 3, 226–249.

Pšenčík, I. (1998), Package ANRAY, version 4.10, *Seismic Waves in Complex* **1998**, 403–404.

Pšenčík, I., and J.L. Martins (2001), Properties of weak contrast PP reflection/transmission coefficients for weakly anisotropic elastic media, *Studia Geophys. Geod.* **45**, 176–199, DOI: 10.1023/A:1021868328668.

Pujol, J. (2003), *Elastic Wave Propagation and Generation in Seismology*, Cambridge University Press, Cambridge.

Rao, C.R. (1964), The use and interpretation of principal component analysis in applied research, *Sankhyā: The Indian J. Statist. Ser. A* **26**, 4, 329–358.

Rao, C.R. (1973), *Linear Statistical Inference and its Applications*, 2nd ed., John Wiley & Sons, Inc., New York.

Rawlinson, N., and M. Sambridge (2004), Wave front evolution in strongly heterogeneous layered media using the fast marching method, *Geophys. J. Int.* **156**, 3, 631–647, DOI: 10.1111/j.1365-246X.2004.02153.x.

Rawlinson, N., S. Pozgay, and S. Fishwick (2010), Seismic tomography: A window into deep Earth, *Phys. Earth Planet. Int.* **178**, 3–4, 101–135, DOI: 10.1016/j.pepi.2009.10.002.

Rial, J.A., M. Elkibbi, and M. Yang (2005), Shear-wave splitting as a tool for the characterization of geothermal fractured reservoirs: lessons learned, *Geothermics* **34**, 3, 365–385, DOI: 10.1016/j.geothermics.2005.03.001.

Riedel, M. (2015), Efficient computation of seismic traveltimes in anisotropic media and the application in pre-stack depth migration, Ph.D. Thesis, TU Bergakademie Freiberg.

Robert, C., and G. Casella (2013), *Monte Carlo Statistical Methods*, Springer Science & Business Media, New York.

Roberts, R.G., A. Christoffersson, and F. Cassidy (1989), Real-time event detection, phase identification and source location estimation using single station three-component seismic data, *Geophys. J.* **97**, 471–480.

Rodi, W., and M.N. Toksoz (2000), Grid-search techniques for seismic event location, Technical Rep., Massachusetts Institute of Technology, Earth Resources Laboratory, Cambridge.

Rudzki, M.P. (1911), Parametrische Darstellung der elastischen Welle in anisotropen Medien, *Bull. Acad. Sci. Cracov*, 503–536.

Sabbione, J.I., M.D. Sacchi, and D.R. Velis (2015), Radon transform-based microseismic event detection and signal-to-noise ratio enhancement, *J. Appl. Geophys.* **113**, 51–63, DOI: 10.1016/j.jappgeo.2014.12.008.

Salimbeni, S., S. Prevolnik, S. Pondrelli, I. Molinari, J. Stipcevic, E. Kissling, V. Šipka, and M. Herak (2017), SKS splitting results in central Italy and Dinaric region inside the AlpArray-CASE project. **In:** *AGU Fall Meeting 2017 Abstracts*, #DI43B-0363.

Sambridge, M. (1999a), Geophysical inversion with a neighbourhood algorithm—I. Searching a parameter space, *Geophys. J. Int.* **138**, 2, 479–494, DOI: 10.1046/j.1365-246X.1999.00876.x.

Sambridge, M. (1999b), Geophysical inversion with a neighbourhood algorithm—II. Appraising the ensemble, *Geophys. J. Int.* **138**, 3, 727–746, DOI: 10.1046/j.1365-246x.1999.00900.x.

Savage, M.K. (1999), Seismic anisotropy and mantle deformation: What have we learned from shear wave splitting? *Rev. Geophys.* **37**, 1, 65–106, DOI: 10.1029/98RG02075.

Schneider Jr., W.A., K.A. Ranzinger, A.H. Balch, and C. Kruse (1992), A dynamic programming approach to first arrival traveltime computation in media with arbitrarily distributed velocities, *Geophysics* **57**, 1, 39–50, DOI: 10.1190/1.1443187.

Schoenberg, M., and C.M. Sayers (1995), Seismic anisotropy of fractured rock, *Geophysics* **60**, 1, 204–211, DOI: 10.1190/1.1443748.

Sen, M.K., and P.L. Stoffa (2013), *Global Optimization Methods in Geophysical Inversion*, Cambridge University Press, Cambridge.

Sena, A.G. (1991), Seismic traveltime equations for azimuthally anisotropic and isotropic media: Estimation of interval elastic properties, *Geophysics* **56**, 12, 2090–2101, DOI: 10.1190/1.1443021.

Senkaya, M., and H. Karsli (2014), A semi-automatic approach to identify first arrival time: the cross-correlation technique (CCT), *Earth Sci. Res. J.* **18**, 2, 107–113, DOI: 10.15446/esrj.v18n2.35887.

Sethian, J.A. (1996), A fast marching level set method for monotonically advancing fronts, *PNAS* **93**, 4, 1591–1595, DOI: 10.1073/pnas.93.4.1591.

Sharma, B.K., A. Kumar, and V.M. Murthy (2010), Evaluation of seismic events detection algorithms, *J. Geol. Soc. India* **75**, 533–538.

Shensa, M.J. (1977), The deflection detector – its theory and evaluation on short-period seismic data, Technical Rep., Texas Instruments Inc. Dallas Equipment Group.

Silver, P.G., and W.W. Chan (1991), Shear wave splitting and subcontinental mantle deformation, *J. Geophys. Res. Solid Earth* **96**, B10, 16429–16454, DOI: 10.1029/91JB00899.

Stork, A.L., J.P. Verdon, and J.M. Kendall (2015), The microseismic response at the In Salah Carbon Capture and Storage (CCS) site, *Int. J. Greenhouse Gas Control* **32**, 159–171, DOI: 10.1016/j.ijggc.2014.11.014.

Tan, Y., C. Chai, and T. Engelder (2014), Use of *S*-wave attenuation from perforation shots to map the growth of the stimulated reservoir volume in the Marcellus gas shale, *The Leading Edge* **33**, 10, 1090–1096, DOI: 10.1190/tle33101090.1.

Tang, C., J.A. Rial, and J.M. Lees (2005), Shear-wave splitting: A diagnostic tool to monitor fluid pressure in geothermal fields, *Geophys. Res. Lett.* **32**, 21, L21317, DOI: 10.1029/2005GL023551.

Tarantola, A. (1984), Inversion of seismic reflection data in the acoustic approximation, *Geophysics* **49**, 8, 1259–1266, DOI: 10.1190/1.1441754.

Tarantola, A. (2005), *Inverse Problem Theory and Methods for Model Parameter Estimation*, Other Titles in Applied Mathematics, Vol. 89, Society for Industrial and Applied Mathematics, 354 pp.

Teanby, N.A., J.M. Kendall, and M. van der Baan (2004), Automation of shear-wave splitting measurements using cluster analysis, *Bull. Seismol. Soc. Am.* **94**, 2, 453–463, DOI: 10.1785/0120030123.

Thomsen, L. (1986), Weak elastic anisotropy, *Geophysics* **51**, 10, 1954–1966, DOI: 10.1190/1.1442051.

Thomsen, L. (2002), *Understanding Seismic Anisotropy in Exploration and Exploitation*, SEG/EAGE Distinguished Instructor Series, No. 5.

Thurber, C.H., and E. Kissling (2000), Advances in travel-time calculations for three-dimensional structures. **In:** C.H. Thurber and N. Rabinowitz (eds.), *Advances in Seismic Event Location*, Springer, Dordrecht, 71–99.

Tillotson, P., J. Sothcott, A.I. Best, M. Chapman, and X.Y. Li (2012), Experimental verification of the fracture density and shear-wave splitting relationship using synthetic silica cemented sandstones with a controlled fracture geometry, *Geophys. Prospect.* **60**, 3, 516–525, DOI: 10.1111/j.1365-2478.2011.01021.x.

Tosi, P., S. Barba, V. De Rubeis, and F. Di Luccio (1999), Seismic signal detection by fractal dimension analysis, *Bull. Seismol. Soc. Am.* **89**, 4, 970–977.

Trnkoczy, A. (1999), Understanding and parameter setting of STA/LTA trigger algorithm. **In:** P. Bormann (ed.), *New Manual of Seismological Observatory Practice 2 (NMSOP-2)*, Deutsches GeoForschungsZentrum GFZ.

Trojanowski, J. (2019), Advanced migration and filtration techniques for microseismic data, Ph.D. Thesis, Institute of Geophysics, Polish Academy of Sciences.

Trojanowski, J., A. Górszczyk, and L. Eisner (2016), A multichannel convolution filter for correlated noise: Microseismic data application. **In:** *SEG Technical Program Expanded Abstracts 2016*, Society of Exploration Geophysicists, 2637–2641, DOI: 10.1190/segam2016-13453668.1.

Tsvankin, I. (1997), Anisotropic parameters and *P*-wave velocity for orthorhombic media, *Geophysics* **62**, 4, 1292–1309, DOI: 10.1190/1.1444231.

Tsvankin, I., and V. Grechka (2011), *Seismology of Azimuthally Anisotropic Media and Seismic Fracture Characterization*, Geophysical References Series, No. 17, Society of Exploration Geophysicists, DOI: 10.1190/1.9781560802839.

Um, J., and C. Thurber (1987), A fast algorithm for two-point seismic ray tracing, *Bull. Seismol. Soc. Am.* **77**, 3, 972–986.

Usher, P.J., A.F. Baird, and J.M. Kendall (2015), Shear-wave splitting in highly anisotropic shale gas formations. **In:** *SEG Technical Program Expanded Abstracts 2015*, Society of Exploration Geophysicists, 2435–2439, DOI: 10.1190/segam2015-58649441.

Van Dok, R.R., J.E. Gaiser, and G. Byerley (2003), Near-surface shear-wave birefringence in the North Sea: Ekofisk 2D/4C test, *The Leading Edge* **22**, 12, 1236–1242, DOI: 10.1190/1.1641376.

Vauchez, A., A. Tommasi, and G. Barruol (1998), Rheological heterogeneity, mechanical anisotropy and deformation of the continental lithosphere, *Tectonophysics* **296**, 1–2, 61–86, DOI: 10.1016/S0040-1951(98)00137-1.

Vavryčuk, V. (1993), Crustal anisotropy from local observations of shear-wave splitting in West Bohemia, Czech Republic, *Bull. Seismol. Soc. Am.* **83**, 5, 1420–1441.

Vera Rodriguez, I., D. Bonar, and M. Sacchi (2012), Microseismic data denoising using a 3C group sparsity constrained time-frequency transform, *Geophysics* **77**, 2, V21–V29, DOI: 10.1190/geo2011-0260.1.

Verdon, J. (2011), Microseismic monitoring and geomechanical modeling of CO2 storage in subsurface reservoirs, *Geophysics* **76**, 5, Z102–Z103, DOI: 10.1190/2011-0926-GEODIS.6.

Verdon, J.P., and J.M. Kendall (2011), Detection of multiple fracture sets using observations of shear-wave splitting in microseismic data, *Geophys. Prospect.* **59**, 4, 593–608, DOI: 10.1111/j.1365-2478.2010.00943.x.

Verdon, J.P., and A. Wüstefeld (2013), Measurement of the normal/tangential fracture compliance ratio (Z_N/Z_T) during hydraulic fracture stimulation using *S*-wave splitting data, *Geophys. Prospect.* **61**, Suppl. 1, 461–475, DOI: 10.1111/j.1365-2478.2012.01132.x.

Verdon, J.P., D.A. Angus, J.M. Kendall, and S.A. Hall (2008), The effect of microstructure and nonlinear stress on anisotropic seismic velocities, *Geophysics* **73**, 4, D41–D51 DOI: 10.1190/1.2931680.

Verdon, J.P., J.M. Kendall, and A. Wüstefeld (2009), Imaging fractures and sedimentary fabrics using shear wave splitting measurements made on passive seismic data, *Geophys. J. Int.* **179**, 2, 1245–1254, DOI: 10.1111/j.1365-246X.2009.04347.x.

Verdon, J.P., J.M. Kendall, D.J. White, and D.A. Angus (2011), Linking microseismic event observations with geomechanical models to minimise the risks of storing CO_2 in geological formations, *Earth and Planet. Sci. Lett.* **305**, 1–2, 143–152, DOI: 10.1016/j.epsl.2011.02.048.

Vernik, L., and J. Milovac (2011), Rock physics of organic shales, *The Leading Edge* **30**, 3, 318–323, DOI: 10.1190/1.3567263.

Vidale, J.E. (1986), Complex polarization analysis of particle motion, *Bull. Seismol. Soc. Am.* **76**, 5, 1393–1405.

Vidale, J. (1988), Finite-difference calculation of travel times, *Bull. Seismol. Soc. Am.* **78**, 6, 2062–2076.

Vinnik, L.P., R. Kind, G.L. Kosarev, and L.I. Makeyeva (1989), Azimuthal anisotropy in the lithosphere from observations of long-period *S*-waves, *Geophys. J. Int.* **99**, 3, 549–559, DOI: 10.1111/j.1365-246X.1989.tb02039.x.

Virieux, J., and V. Farra (1991), Ray tracing in 3-D complex isotropic media: An analysis of the problem, *Geophysics* **56**, 12, 2057–2069, DOI: 10.1190/1.1443018.

Voigt, W. (1910), *Lehrbuch der Kristallphysik (mit Ausschluss der Kristalloptik)*, Bibliotheca Mathematica Teubneriana; Johnson, New York.

Walck, M.C., and E.P. Chael (1991), Optimal backazimuth estimation for three-component recordings of regional seismic events, *Bull. Seismol. Soc. Am.* **81**, 2, 643–666.

Wandycz, P., E. Święch, L. Eisner, A. Pasternacki, D. Anikiev, and T. Maćkowski (2018), Estimating microseismic detectability of the surface-monitoring network using downhole-monitoring array, *Interpretation* **6**, 3, SH107–SH115, DOI: 10.1190/INT-2017-0198.1.

Wang, Z. (2001), Seismic anisotropy in sedimentary rocks. **In:** *SEG Technical Program Expanded Abstracts 2001*, Society of Exploration Geophysicists, 1740–1743, DOI: 10.1190/1.1816460.

Warpinski, N.R., and P.T. Branagan (1989), Altered-stress fracturing, *J. Petrol. Technol.* **41**, 9, 990–997, DOI: 10.2118/17533-PA.

Warpinski, N.R., P.T. Branagan, R.E. Peterson, S.L. Wolhart, and J.E. Uhl (1998), Mapping hydraulic fracture growth and geometry using microseismic events detected by a wireline retrievable accelerometer array. **In:** *Proc. SPE Gas Technology Symposium, March 1998, Calgary, Canada*, Society of Petroleum Engineers, SPE-40014-MS, DOI: 10.2118/40014-MS.

Wesson, R.L. (1971), Travel-time inversion for laterally inhomogeneous crustal velocity models, *Bull. Seismol. Soc. Am.* **61**, 3, 729–746.

Willis, H.A., G.L. Rethford, and E. Bielanski (1986), Azimuthal anisotropy: Occurrence and effect on shear-wave data quality. **In:** *SEG Technical Program Expanded Abstracts 1986*, Society of Exploration Geophysicists, 479–481, DOI: 10.1190/1.1893035.

Winkler, K.W. (1986), Estimates of velocity dispersion between seismic and ultrasonic frequencies, *Geophysics* **51**, 1, 183–189, DOI: 10.1190/1.1442031.

Withers, M., R. Aster, C. Young, J. Beiriger, M. Harris, S. Moore, and J. Trujillo (1998), A comparison of select trigger algorithms for automated global seismic phase and event detection, *Bull. Seismol. Soc. Am.* **88**, 1, 95–106.

Withers, M., R. Aster, and C. Young (1999), An automated local and regional seismic event detection and location system using waveform correlation, *Bull. Seismol. Soc. Am.* **89**, 3, 657–669.

Wolfe, C.J., and P.G. Silver (1998), Seismic anisotropy of oceanic upper mantle: Shear wave splitting methodologies and observations, *J. Geophys. Res. Solid Earth* **103**, B1, 749–771, DOI: 10.1029/97JB02023.

Wüestefeld, A. (2007), Methods and applications of shear wave splitting: The East European Craton, Ph.D. Thesis, Université Montpellier 2 Sciences et Techniques du Languedoc.

Wuestefeld, A., O. Al-Harrasi, J.P. Verdon, J. Wookey, and J.M. Kendall (2010), A strategy for automated analysis of passive microseismic data to image seismic anisotropy and fracture characteristics, *Geophys. Prospect.* **58**, 5, 755–773, DOI: 10.1111/j.1365-2478.2010.00891.x.

Wuestefeld, A., J.M. Kendall, J.P. Verdon, and A. van As (2011), In situ monitoring of rock fracturing using shear wave splitting analysis: an example from a mining setting, *Geophys. J. Int.* **187**, 2, 848–860, DOI: 10.1111/j.1365-246X.2011.05171.x.

Wuestefeld, A., S.M. Greve, S.P. Näsholm, and V. Oye (2018), Benchmarking earthquake location algorithms: A synthetic comparison, *Geophysics* **83**, 4, KS35–KS47, DOI: 10.1190/geo2017-0317.1.

Xu, S., and M. King (1989), Shear-wave birefringence and directional permeability in fractured rock, *Scientific Drilling* **1**, 1, 27–33.

Yaskevich, S., G. Loginov, A. Duchkov, and A. Serdukov (2016), Pitfalls of microseismic data inversion in the case of strong anisotropy, *Appl. Geophys*. **13**, 2, 326–332, DOI: 10.1007/s11770-016-0558-9.

Yu, C., and S. Shapiro (2014), Seismic anisotropy of shale: Inversion of microseismic data. **In:** *SEG Technical Program Expanded Abstracts 2014*, Society of Exploration Geophysicists, 2324–2329, DOI: 10.1190/segam2014-1251.1.

Zangeneh, N., E. Eberhardt, and R.M. Bustin (2015), Investigation of the influence of stress shadows on horizontal hydraulic fractures from adjacent lateral wells, *J. Unconven. Oil Gas Resour*. **9**, 54–64, DOI: 10.1016/j.juogr.2014.11.001.

Zaręba, M., and T. Danek (2019), Correction to: VSP polarization angles determination: Wysin-1 processing case study, *Acta Geophys.* **67**, 2, 737–737, DOI: 10.1007/s11600-019-00277-3.

Zelt, C.A. (1999), Modelling strategies and model assessment for wide-angle seismic traveltime data, *Geophys. J. Int.* **139**, 1, 183–204, DOI: 10.1046/j.1365-246X.1999.00934.x.

Zelt, C.A., and P.J. Barton (1998), Three-dimensional seismic refraction tomography: A comparison of two methods applied to data from the Faeroe Basin, *J. Geophys. Res. Solid Earth* **103**, B4, 7187–7210, DOI: 10.1029/97JB03536.

Zhao, H. (2005), A fast sweeping method for Eikonal equations, *Math. Comput.* **74**, 603–627, DOI: 10.1090/S0025-5718-04-01678-3.

Received 18 December 2020
Received in revised form 1 March 2021
Accepted 5 March 2021

"Publications of the Institute of Geophysics, Polish Academy of Sciences: Geophysical Data Bases, Processing and Instrumentation" appears in the following series:

A – Physics of the Earth's Interior

B – Seismology

C – Geomagnetism

D – Physics of the Atmosphere

E – Hydrology (formerly Water Resources)

P – Polar Research

M – Miscellanea

Every volume has two numbers: the first one is the consecutive number of the journal and the second one (in brackets) is the current number in the series.